Title
Towards the resolution of the solar neutrino problem

Author
Friedland, Alexander

Publication Date
2000-08-29

LBNL-46714

ERNEST ORLANDO LAWRENCE
BERKELEY NATIONAL LABORATORY

Towards the Resolution of the Solar Neutrino Problem

Alexander Friedland

Physics Division

August 2000

Ph.D. Thesis

DISCLAIMER

LBNL-46714

Towards the Resolution of the Solar Neutrino Problem

Alexander Friedland
Ph.D. Thesis

Department of Physics
University of California, Berkeley

and

Physics Division
Ernest Orlando Lawrence Berkeley National Laboratory
University of California
Berkeley, California 94720

August 2000

This work was supported by the Director, Office of Science, Office of High Energy and Nuclear Physics, Division of High Energy Physics, of the U.S. Department of Energy under Contract No. DE-AC03-76SF00098.

Towards the Resolution of the Solar Neutrino Problem

by

Alexander Friedland

Moscow Institute of Physics and Technology, 1990-1993
M.S., University of California at Berkeley, 1996

A dissertation submitted in partial satisfaction of the
requirements for the degree of
Doctor of Philosophy

in

Physics

in the

GRADUATE DIVISION
of the
UNIVERSITY of CALIFORNIA at BERKELEY

Committee in charge:

Professor Hitoshi Murayama, Chair
Professor Lawrence Hall
Professor Nicolai Reshetikhin

Spring 2000
LBNL-46714

Towards the Resolution of the Solar Neutrino Problem

by

Alexander Friedland

Abstract

Towards the Resolution of the Solar Neutrino Problem

by

Alexander Friedland

Doctor of Philosophy in Physics

University of California at Berkeley

Professor Hitoshi Murayama, Chair

A number of experiments have accumulated over the years a large amount of solar neutrino data. The data indicate that the observed solar neutrino flux is significantly smaller than expected and, furthermore, that the electron neutrino survival probability is energy dependent. This "solar neutrino problem" is best solved by assuming that the electron neutrino oscillates into another neutrino species.

Even though one can classify the solar neutrino deficit as strong evidence for neutrino oscillations, it is not yet considered a definitive proof. Traditional objections are that the evidence for solar neutrino oscillations relies on a combination of hard, different experiments, and that the Standard Solar Model (SSM) might not be accurate enough to precisely predict the fluxes of different solar neutrino components. Even though it seems unlikely that modifications to the SSM alone can explain the

current solar neutrino data, one still cannot completely discount the possibility that a combination of unknown systematic errors in some of the experiments and certain modifications to the SSM could conspire to yield the observed data.

To conclusively demonstrate that there is indeed new physics in solar neutrinos, new experiments are aiming at detecting "smoking gun" signatures of neutrino oscillations, such as an anomalous seasonal variation in the observed neutrino flux or a day-night variation due to the regeneration of electron neutrinos in the Earth. In this dissertation we study the sensitivity reach of two upcoming neutrino experiments, Borexino and KamLAND, to both of these effects.

Results of neutrino oscillation experiments for the case of two-flavor oscillations have always been presented on the $(\sin^2 2\theta, \Delta m^2)$ parameter space. We point out, however, that this parameterization misses the half of the parameter space $\frac{\pi}{4} < \theta \leq \frac{\pi}{2}$, which is physically inequivalent to the region $0 \leq \theta \leq \frac{\pi}{4}$ in the presence of matter effects. The MSW solutions to the solar neutrino problem can extend to the $\theta > \pi/4$ side. Furthermore, even the "vacuum oscillation" solutions are affected by solar matter effects and hence are different in the two sides.

Professor Hitoshi Murayama
Dissertation Committee Chair

To my parents

Contents

List of Figures

List of Tables

Acknowledgements

I would like to thank Prof. Hitoshi Murayama and Prof. Eugene Commins for giving me the opportunity to pursue my graduate research at Berkeley and also for providing invaluable support and inspiration.

I am thankful to all the students in the Theory Group for providing a stimulating atmosphere, in particular to David Smith and Neal Weiner, for keeping up a certain level of noise in our office absolutely essential for scientific work. I am grateful to André de Gouvêa, who coauthored most of the papers with me while I was at Berkeley, for many stimulating discussions.

I would like to thank John Bahcall his encouragements on the project of Section 5.1, and also for including in the BP2000 solar model the data for the outer regions of the Sun. I would also like to thank James Pantaleone, Plamen Krastev, M.C. Gonzalez-Garcia, and Yosef Nir for their valuable input.

I owe my gratitude to my parents for their support ever since I was a child and to Helen for being the best sister out there. I am greatly indebted to my aunt Natasha, who has done so much for me and my family, and to my late uncle Fima, who was a wonderful person. I am also grateful to my grandmother, who showed me by her own example the power of human determination and critical thinking.

Finally, I owe my gratitude to my wonderful wife Natasha, for her understanding and support, especially in times when I really needed them.

Chapter 1

Introduction

In the last decade the field of neutrino physics has witnessed several remarkable developments. The atmospheric neutrino data collected by the Super-Kamiokande experiment provide a very strong evidence that neutrinos are massive and the flavor oscillations take place. Significant advances have been also made in the solar neutrino physics. The data from the radiochemical and water Cherenkov detectors indicates that neutrino oscillations may also be responsible for the solar neutrino deficit. These neutrino oscillation results provide the best (only?) evidence at the moment for new physics beyond the Standard Model.

In the beginning of this dissertation we present an overview of the solar neutrino physics. We then describe the original results on the sensitivity of the two upcoming ^{7}Be experiments Borexino and KamLAND to "smoking gun" signatures of neutrino oscillations and an exploration of the full physical parameter space $0 < \theta < \pi/2$. The

overview is presented in Chapter 2. It contains a description of basic neutrino properties and interactions and necessary background about the solar neutrino problem. We also argue for the need to look for "smoking gun" signatures at present and future experiments as a way to unequivocally prove the neutrino oscillation hypothesis.

In Chapter 3 we study the sensitivity reach of the Borexino and KamLAND experiments to the seasonal variations of the solar neutrino flux. We consider the cases of both the "normal" $1/L^2$ variations and the anomalous variations expected in the vacuum oscillation case. In Chapter 4 we determine the sensitivity of these experiments to the neutrino regeneration phenomenon in the Earth. We also point out that is it important to study the regeneration effect for $0 < \theta < \pi/2$. Part of this range ($\theta > \pi/4$) has been traditionally neglected in the literature.

In Chapter 5 we study the solutions to the solar neutrino problem in this full parameter space. We investigate the cases of both the "vacuum oscillation" solutions and the MSW solution. Remarkably, it turns out that for Δm^2 in the "vacuum oscillation" region the solar matter effect can in fact be nonnegligible, especially for the low–energy *pp* neutrinos. This makes the two sides, $\theta < \pi/4$ and $\theta > \pi/4$, not completely equivalent. We further explore the MSW region and find that the allowed regions there are not necessarily confined to $\theta < \pi/4$ side.

The last chapter contains our summary and conclusions. The appendices clarify several technical points that were used in the analysis in different chapters.

Chapter 2

Overview of Neutrino Physics

2.1 Neutrinos in the Standard Model

This section contains an elementary review of well-established neutrino properties and interactions. Such interactions include the so-called charged and neutral current weak interactions. Both interactions are described by the unified electroweak theory which, along with the QCD, forms the basis of the Standard Model of particle physics.

2.1.1 Elementary review of neutrino properties

There are two basic features that distinguish the neutrinos from all other known elementary particles:

- they are left-handed, meaning that a neutrino spin is always antiparallel to its momentum (parallel for antineutrino); and

- they have very small interaction cross-sections with matter.

The former fact, established in a beautiful experiment by Goldhaber *et al.* in 1958 [5], played a crucial role in our understanding of the nature of the weak interactions and in the construction of the unified electroweak theory. The latter is a consequence of the fact that neutrinos do not possess either electric charge or color, and hence couple to other particles only through the weak interactions.

As the name suggests, the weak interaction cross-sections and decay rates are many orders of magnitude smaller then those of comparable processes mediated by the electromagnetic or strong forces. As an example, the lifetime of the Σ^- hyperon (dds), which decays almost exclusively via the following weak interaction channel: $\Sigma^- \to n + \pi^-$, is 1.48×10^{-10} seconds. By comparison, the electromagnetic decay of Σ^0 , the neutral partner of Σ^- with the quark composition $s(ud+du)/\sqrt{2}$, $\Sigma^0 \to \Lambda+\gamma$, occurs on a much shorter time scale, $\tau = 7 \times 10^{-20}$ seconds. As a consequence of such disparity in strength, although all quarks and leptons participate in weak interactions, their effects are often swamped by strong or electromagnetic couplings. What makes it possible to observed weak interaction effects in low energy experiments is fact that they do not respect certain conservation laws obeyed by strong and electromagnetic interactions, such as conservation of parity, strangeness, *etc.* In the example given above the decay of Σ^- violated strangeness. Another example is provided by atomic parity violation experiments, which measure rates of certain atomic transitions disallowed by parity conservation, but allowed once weak interactions are included.

The fact that the neutrino couples only weakly to matter and the corresponding cross-sections are tiny has a direct implication on the design of neutrino experiments. As will be described later, all neutrino detection experiments require very large targets, and state-of-the-art shielding and background rejection. The history of neutrino discovery itself provides a great illustration to this point. Postulated by Pauli in 1929 to explain the continuous spectrum of β decay of the proton, the neutrino was not detected until 1956, when Reines and Cowan [6] first observed the reaction $\bar{\nu}_e + p \rightarrow n + e^+$ in their classic experiment, using 1 MeV reactor antineutrinos and a target of cadmium chloride ($CdCl_2$) and water. To illustrate the inherent difficulty of all neutrino detection experiments, it is worth mentioning that the mean free path of such 1 MeV antineutrinos in water is of the order of 10^{20} cm or 100 light years.

2.1.2 Coupling of leptons in the electroweak theory

The theory which provided the correct description of the weak interactions and at the same time united them with the electromagnetic interaction was developed by Glashow [7], Salam [8], and Weinberg [9]. The theory represents a logical and beautiful construction, which was confirmed in a countless number of experiments. Together with the theory of strong interactions, the QCD, it constitutes the Standard Model of particle physics. In this section we review the electroweak theory and present the results that will be used to describe neutrino coupling to matter.

The fundamental concept used to describe the electromagnetic interaction is the

coupling of the electromagnetic current to a photon. The interaction between a photon and a charged particle is given by $H_{int} = A_\mu J^\mu$. The current J^μ is simply $q(p+p')^\mu$ for a scalar particle and $q\bar{f}\gamma^\mu i$ for fermions. Here i and f are the operators of the initial and final particles, and p and p' refer to the initial and final momenta. The electromagnetic current can also be decomposed in terms of left- and right-handed components. Introducing $\psi_L \equiv P_L\psi \equiv \frac{(1-\gamma^5)}{2}\psi$ and using $\{\gamma^5, \gamma^\mu\} = 0$, we can trivially show that

$$J^\mu_{EM} = q(\bar{f}_L\gamma^\mu i_L + \bar{f}_R\gamma^\mu i_R). \qquad (2.1)$$

The terminology "left-handed" ("right-handed") comes from the fact that, in the limit $v \to c$, u_L (u_R) describes a particle with its spin pointing in the direction opposite to (along) its momentum. According to Eq. (2.1), the electromagnetic current receives equal contributions from left- and right-handed components. Such a current is referred to as the *vector* current.

The theory of the weak interaction is based on an analogous construction. One introduces *weak currents* and couples them to the $W^\pm$ and Z bosons. The reason why the same approach works in both cases is not accidental. Both weak and electromagnetic couplings are *gauge* interactions and, moreover, are two parts of the *same* gauge theory, the electroweak $SU(2) \times U(1)$ model, as will be described shortly.

From experiment, it is known that weak interactions can convert the electron and the electron neutrino into each other. If an electron emits a W^- boson and becomes a neutrino, the corresponding weak current is $J^\mu_{W^-} = \bar{\nu}_L\gamma^\mu e_L$. Notice that only the

left-handed component of the electron enters J_{W^-}, since it couples to the neutrino and the neutrino is left-handed. Thus, the weak current is not a vector current, unlike the electromagnetic current given in Eq. (2.1). The coupling to the W is instead known as a $V-A$ interaction, because J_W can be written as $\bar{\nu}\gamma^\mu(1-\gamma^5)e = \bar{\nu}\gamma^\mu e - \bar{\nu}\gamma^\mu\gamma^5 e =$ Vector $-$ Axial vector.

Since the states ν_e and e can turn into each other as a result of weak interaction, it is important to explore whether these transitions can be described by a gauge theory. The first natural candidate to check is the group of $SU(2)$ rotations. Let us group e_L and ν_e in a doublet:

$$L = \begin{pmatrix} \nu_e \\ e_L \end{pmatrix}. \tag{2.2}$$

The generators of $SU(2)$ in the fundamental representation are

$$\boldsymbol{T}^{(1)} = \frac{1}{2}\begin{pmatrix} 0 & 1 \\ 1 & 0 \end{pmatrix}, \quad \boldsymbol{T}^{(2)} = \frac{1}{2}\begin{pmatrix} 0 & -i \\ i & 0 \end{pmatrix}, \quad \boldsymbol{T}^{(3)} = \frac{1}{2}\begin{pmatrix} 1 & 0 \\ 0 & -1 \end{pmatrix}. \tag{2.3}$$

In terms of these matrices the current J_{W^+} can be written as

$$J_{W^+} = \bar{L}\gamma^\mu \begin{pmatrix} 0 & 0 \\ 1 & 0 \end{pmatrix} L = \bar{L}\gamma^\mu \boldsymbol{T}^{(-)} L, \tag{2.4}$$

where we introduced the matrix $\boldsymbol{T}^{(+)} = \boldsymbol{T}^{(1)} - i\boldsymbol{T}^{(2)}$. Similarly, the current that couples to W^- can be written as $\bar{L}\gamma^\mu \boldsymbol{T}^{(+)} L$.

Thus the term in the Lagrangian responsible for the coupling of the lepton doublet

(2.2) to the $W^{\pm}$ bosons is given by

$$\mathcal{L}_{W^{\pm}} = \tilde{g}(W^{+}_{\mu} J^{(+)\mu} + W^{-}_{\mu} J^{(-)\mu}). \tag{2.5}$$

This can be rewritten in terms of $T^{(1,2)}$, if we introduce W^1 and W^2 such that $W^+ = (W^1 + iW^2)/\sqrt{2}$, $W^- = (W^1 - iW^2)/\sqrt{2}$:

$$\mathcal{L}_{W^{1,2}} = g(W^1_{\mu} \bar{L}\gamma^{\mu} \boldsymbol{T}^{(1)} L + W^2_{\mu} \bar{L}\gamma^{\mu} \boldsymbol{T}^{(2)} L). \tag{2.6}$$

The coupling constants g and $\tilde{g}$ are related by $g = \sqrt{2}\tilde{g}$.

We thus showed that the charged current interactions can indeed be obtained from the first two generators of $SU(2)$. In order to have a full $SU(2)$ gauge interaction we add a term containing the third generator:

$$\mathcal{L}_{SU(2)} = g(W^1_{\mu} \bar{L}\gamma^{\mu} \boldsymbol{T}^{(1)} L + W^2_{\mu} \bar{L}\gamma^{\mu} \boldsymbol{T}^{(2)} L + W^3_{\mu} \bar{L}\gamma^{\mu} \boldsymbol{T}^{(3)} L), \tag{2.7}$$

where a new gauge boson, W^3, was introduced.

The addition of the third term in Eq. (2.7) leads to very important consequences. Notice that this term gives two new diagonal currents, $\bar{e}_L \gamma^{\mu} e_L$ and $\bar{\nu}_L \gamma^{\mu} \nu_L$. Can these currents be in fact the electromagnetic currents? The answer is obviously "no", for two reasons: i) it only involves the left-handed components and ii) it would give a non-zero charge to the neutrino. On the other hand, how can we explain the charges (0, -1) of the doublet L? Introducing a separate $U(1)_{EM}$ gauge group and assigning different charges to the elements of the doublet would be unacceptable, if we want to keep the weak $SU(2)$.

The resolution is suggested by the pattern of the charges $(0, -1)$, which can be represented as $Q = T^{(3)} + Y$, with $Y = -1/2$ and $T^{(3)}$ is the eigenvalue of the isospin operator. *Part* of the electric charge can indeed be due to the interaction with the W^3 component, while the remainder can be explained if we introduce an additional $U(1)$ group (called the *hypercharge* $U(1)_Y$) and assign a hypercharge $Y = -1/2$ to the doublet L as a whole. The diagonal part of the interaction is now

$$\Delta\mathcal{L}_{\text{neutr}} = gW^3_\mu \bar{L}\gamma^\mu \boldsymbol{T}^{(3)} L + g' Y_L B_\mu \bar{L}\gamma^\mu L + g' Y_R B_\mu \bar{e_R}\gamma^\mu e_R. \tag{2.8}$$

On closer inspection of this idea, several issues arise:

- In nature, there is only one photon, while in our case we have two fields, W^3 and B.
- The gauge group $U(1)_Y$ will have its own coupling constant g', which we need to relate to g and e, the electric charge.
- The electric charge of the right-handed electron will come purely from the $U(1)_Y$ interaction. This will require different hypercharge assignments for e_L and e_R, *i. e.* $Y_L \neq Y_R$ in Eq. (2.8).

The first point can be resolved if only one of the linear combinations of W^3 and B remains massless, while the other one acquires a mass. Let

$$\begin{aligned} B_\mu &= \cos\theta_W A_\mu - \sin\theta_W Z_\mu, \\ W^3_\mu &= \sin\theta_W A_\mu + \cos\theta_W Z_\mu, \end{aligned} \tag{2.9}$$

where A will be the photon, Z will acquire a mass, and θ_M is known as the weak mixing angle.

We can now address the second point. Plugging in Eq. (2.9) into Eq. (2.8) and looking at the coefficient in front of A_μ, we get

$$gT^{(3)} \sin\theta_M + g' Y_L \cos\theta_M = Qe. \tag{2.10}$$

Plugging in our proposed relationship $Q = Y + T^{(3)}$, we obtain

$$(g \sin\theta_M - g' \cos\theta_M) T^{(3)} + g' Q \cos\theta_M = Qe, \tag{2.11}$$

which is satisfied if

$$\begin{aligned} g \sin\theta_M - g' \cos\theta_M &= 0, \\ g' \cos\theta_M &= e. \end{aligned} \tag{2.12}$$

Thus,

$$g \sin\theta_M = g' \cos\theta_M = e. \tag{2.13}$$

Finally, for the right-handed component of the electron e_L the hypercharge is $Y_{e_R} = -1$. Thus, the right- and left-handed components of the electron are treated as different particles in this framework.

We can also compute the coupling strength of the Z boson to the leptons. Similarly to the way Eq. (2.10) was obtained, we can combine Eq. (2.9) and Eq. (2.8) and collect

the coefficients in front of $Z_\mu \bar{\psi}\gamma^\mu\psi$. We obtain

$$gT^{(3)}\cos\theta_M - g'Y_L\sin\theta_M = gT^{(3)}\cos\theta_M - g\frac{\sin\theta_M}{\cos\theta_M}(Q - T^{(3)})\sin\theta_M =$$
$$\frac{g}{\cos\theta_M}(T^{(3)} - Q\sin^2\theta_M) \tag{2.14}$$

To summarize, the neutrinos couple to both $W^\pm$ and Z bosons through what is known as correspondingly charged and neutral current interactions:

$$\begin{aligned}
\Delta\mathcal{L}_{\text{int}} &= \Delta\mathcal{L}_{CC} + \Delta\mathcal{L}_{NC}, \\
\Delta\mathcal{L}_{CC} &= \frac{g}{\sqrt{2}}(W^+_\mu J^{(+)\mu} + W^-_\mu J^{(-)\mu}), \\
\Delta\mathcal{L}_{NC} &= \frac{g}{\cos\theta_M}(T^{(3)} - Q\sin^2\theta_M)Z_\mu J^{(0)\mu},
\end{aligned} \tag{2.15}$$

where

$$\begin{aligned}
T^{(3)}_{\text{neutrino}} &= \frac{1}{2}, \\
Q_{\text{neutrino}} &= 0, \\
J^{(+)\mu} &= \bar{e}_L\gamma^\mu\nu, \\
J^{(-)\mu} &= (J^{(+)\nu})^\dagger, \\
J^{(0)\mu} &= \bar{e}_L\gamma^\mu e_L + \bar{e}_R\gamma^\mu e_R + \bar{\nu}\gamma^\mu\nu.
\end{aligned} \tag{2.16}$$

2.1.3 Masses through the Higgs mechanism

Next we will address two outstanding issues:

- We need to introduce the Higgs mechanism and to prove that the Z boson in Eq. (2.9) indeed acquires a mass, while the photon A remains massless.

- We have not discussed the quark sector.

In order to explain how the Z boson acquires a mass, we first need to address the fermion masses. A naive approach would be to add $m\bar{e}_L e_R$ to the Lagrangian. This, however, is not allowed by the $SU(2)$ gauge invariance. For a term in the Lagrangian to be gauge invariant, it must contain the doublet L as a whole, without splitting its components. To obtain a gauge invariant combination, we can add another $SU(2)$ doublet to the theory, H. Unlike L, the components of H are *bosons*. This allows us to write

$$\Delta\mathcal{L}_{\text{mass}} = -\lambda \bar{L} H e_R, \tag{2.17}$$

where λ is a constant of interaction, called the Yukawa coupling. To match the hypercharges, we must assign $Y = +1/2$ to H. The doublet H is called a Higgs doublet. It contains a positively charged boson and a neutral boson,

$$H = \begin{pmatrix} h^+ \\ h^0 \end{pmatrix}. \tag{2.18}$$

So far, this is an interaction term between three fields, not a mass term. To obtain a mass term from Eq. (2.18), we postulate that the neutral component of the Higgs doublet acquires a non-zero *vacuum expectation value* (VEV),

$$\langle H \rangle = \begin{pmatrix} 0 \\ v \end{pmatrix}. \tag{2.19}$$

Notice that we did not write a nonzero VEV for the charged component h^+, as that would violate electric charge conservation. Substituting Eq. (2.19) into Eq. (2.17), we obtain the desired mass term for the electron, $-\lambda v \bar{e}_L e_R$.

We are now ready to consider the mass for the gauge bosons. Knowing the gauge quantum numbers of the Higgs doublet, we will analyze its coupling to the gauge bosons $W^{1,2,3}$ and B. This interaction is described by the following terms in the Lagrangian:

$$\mathcal{L} \subset (D_\mu H)(D^\mu H) = \left|(\partial_\mu - igW_\mu^{(a)}T^{(a)} - ig'Y_H B_\mu)H\right|^2 \tag{2.20}$$

We now set H to its VEV, Eq. (2.19), and look for terms that correspond to mass terms for the gauge bosons.

$$\left|\begin{pmatrix} g(W_\mu^{(1)} - iW_\mu^{(2)})v/2 \\ (-gW_\mu^{(3)} + g'B_\mu)v/2 \end{pmatrix}\right|^2 = \frac{g^2v^2}{2}W_\mu^+ W^{-\mu} + \frac{(g^2+g'^2)v^2}{4}Z_\mu Z^\mu, \tag{2.21}$$

where we used the fact that $(-gW_\mu^{(3)} + g'B_\mu) = \sqrt{g^2+g'^2}Z_\mu$, according to Eq. (2.9). This demonstrates that $W^\pm$ and Z indeed become massive as a result of coupling to the Higgs field, while the photon remains massless. Moreover, it makes a prediction of the ratio of the W and Z masses

$$m_W/m_Z = \cos\theta_W = \sqrt{g^2 - e^2}/g, \tag{2.22}$$

in agreement with experiment.

2.1.4 The Quark Sector

The discussion so far has been concentrated on the leptons. We will now briefly present the results for the quark sector.

Just like the leptons, the left-handed quarks can also be grouped in a doublet:

$$Q_L = \begin{pmatrix} u \\ d' \end{pmatrix}. \tag{2.23}$$

Notice that the lower component is denoted d' and not simply d. The meaning of this notation will be discussed shortly. To reproduce the electric charges of $(+2/3, -1/3)$ with $Q = Y + T^{(3)}$ we will assign to Q_L the hypercharge of $+1/6$. The doublet Q will thus couple to $W^{\pm}$, Z, and the photon.

Next, we consider the right-handed quarks. Unlike the situation in the lepton sector, there are two right-handed particles in a single generation, U_R and D_R. The hypercharge assignments which yield the correct electric charges are $Y_U = 2/3$, $Y_D = -1/3$. Thus, U_R and D_R will couple to Z and the photon.

At last, we discuss the generation of masses for the quarks. The mass for the down-type quarks can be generated in the same way as for the leptons, with the term

$$-\lambda_D \bar{Q}_L H D_R \tag{2.24}$$

in the Lagrangian. On the other hand, the mass for the up-type quarks has no analog in the lepton sector. The gauge invariant combination involving Q_L and H can be constructed if we make use of the second possible way to make $SU(2)$ invariants,

$\epsilon_{\alpha\beta}A^\alpha B^\beta$. This combination is invariant because $SU(2)$ transformation matrices have a unit determinant. (The invariants we previously used for the leptons and the down-type quarks were of the form $A^\dagger_\alpha B^\alpha$.) It is easy to see that the term

$$-\lambda_D \epsilon_{\alpha\beta} \bar{Q}^\alpha_L H^{\dagger\beta} U_R \tag{2.25}$$

is gauge invariant and will give masses to the up-type quarks.

In Eqs. (2.24) and (2.25) we omitted the generation indices. In fact in turns out the mass eigenstates and the weak eigenstates are not aligned with each other. By that we simply mean that when, for example, the up quark emits a W^+ and turns into some state in the down sector, there is no reason for that state to be a mass eigenstate. In general, it can be a linear superposition of the mass eigenstates d, s, and b. In the case of only two generations the misalignment effect between the weak and the mass bases is given in terms of the Cabibbo angle θ_C:

$$\begin{aligned} d' &= \cos\theta_C d + \sin\theta_C s, \\ s' &= -\sin\theta_C d + \cos\theta_C s. \end{aligned} \tag{2.26}$$

Here d and s are defined to be the mass eigenstates, while d' and s' are the states that enter the weak doublets (see Eq. (2.23)). The misalignment is responsible, for instance, for weak decays of the strange particles.

In the case of the three generations, the mass and weak bases are related by a 3×3 matrix, known as the Cabibbo-Kobayashi-Maskawa (CKM) matrix. This matrix contains four independent parameters, three angles and one phase. The phase

is thought to be responsible for the CP violation observed in nature.

There is no analog of the CKM matrix for the lepton sector, so long as the neutrinos are massless. If, however, neutrinos had masses and furthermore those masses were different, one would be required to introduce the mixing matrix for the leptons as well. This would lead to the neutrino oscillations, as will be discussed in the next section.

2.2 Neutrino Masses and Oscillations

As was shown in the previous section, in the Standard Model (SM) neutrinos are massless. Thus, a detection of nonzero neutrino masses would be an indication of new physics beyond the SM. In this sections we will explore the consequences of neutrino masses. We will show that if neutrino mass eigenvalues are different, one may observe neutrino oscillations. We will describe neutrino oscillations in vacuum and in matter.

2.2.1 Neutrino Oscillations in Vacuum

To introduce the concept of neutrino mixing and oscillations, let us first discuss one important difference between the neutrinos and other known elementary particles. Unlike the other particles in the Standard Model, the neutrinos are defined as weak eigenstates, not mass eigenstates.

Normally, when one speaks of a particle, one usually has in mind a state of a

certain mass. For example, an electron $|e\rangle$ and a muon $|\mu\rangle$ are each defined as the states of given masses. The same applies to quarks. As was discussed in 2.1.4, the weak currents contain superpositions of quark mass eigenstates, resulting in the need for the CKM matrix. In the case of massless neutrinos, however, one cannot speak about mass eigenstates. Thus, the neutrino states are defined as the weak eigenstates[1]. This means that, for example, ν_e is defined as the state which, upon emitting a W^+ boson, becomes an electron. In this sense ν_e is analogous to the state d' (Eq. 2.26) in the quark sector, rather than d.

If neutrinos were massive, then it seems quite plausible that the neutrino mass eigenstates and weak eigenstates would not be aligned, just like in the quark sector. In the case of only two generations the relationship between the two bases can be parameterized as

$$\begin{aligned} |\nu_e\rangle &= \cos\theta|\nu_1\rangle + \sin\theta|\nu_2\rangle, \\ |\nu_\mu\rangle &= -\sin\theta|\nu_1\rangle + \cos\theta|\nu_2\rangle, \end{aligned} \tag{2.27}$$

where $|\nu_1\rangle$ and $|\nu_2\rangle$ are the mass eigenstates and θ is the mixing angle. The misalignment between the two bases leads to neutrino flavor oscillations.

To see how the oscillations arise in the simplest case, let us consider the evolution of a neutrino state created at some point as ν_e and propagating in vacuum. If the neutrino energy is much greater than its mass, its energy is given by $E_i = \sqrt{p^2 + m_i^2} \simeq$

[1]See the PDG book [10].

$p + \frac{m_i^2}{2p} \simeq p + \frac{m_i^2}{2E}$. At time t the state becomes

$$|\nu(t)\rangle = (\cos\theta|\nu_1\rangle + e^{i\frac{\Delta m^2}{2E}t}\sin\theta|\nu_2\rangle)e^{i\phi},$$

where we factored out the common phase $e^{i\phi}$. The probability to detect this state as ν_e is

$$P = |\langle\nu_e|\nu(t)\rangle|^2 = 1 - \sin^2 2\theta \sin^2\left(\frac{\Delta m^2 t}{4E_\nu}\right). \tag{2.28}$$

This formula shows that the flavor composition of the neutrino states depends on time t, *i. e.* the neutrino *oscillates* with the amplitude given by $\sin^2 2\theta$. Separate lepton numbers are not conserved unless $\theta = 0$ or $\pi/2$. In practical units

$$P = 1 - \sin^2 2\theta \sin^2\left(1.27\frac{\Delta m^2}{E_\nu}L\right), \tag{2.29}$$

where the neutrino energy E_ν is in GeV, the distance traveled L is in kilometers, and the mass-squared splitting is in eV^2.

We can also write the Hamiltonian H of the system. In the mass basis ($|\nu_1\rangle$, $|\nu_2\rangle$) H is simply

$$H = \begin{pmatrix} \frac{m_1^2}{2E_\nu} & 0 \\ 0 & \frac{m_2^2}{2E_\nu} \end{pmatrix} = \text{const} + \begin{pmatrix} -\frac{\Delta m^2}{4E_\nu} & 0 \\ 0 & \frac{\Delta m^2}{4E_\nu} \end{pmatrix},$$

while in the weak basis ($|\nu_e\rangle$, $|\nu_\mu\rangle$) it takes the form

$$H = \text{const} + \frac{\Delta m^2}{4E_\nu}\begin{pmatrix} -\cos 2\theta & \sin 2\theta \\ \sin 2\theta & \cos 2\theta \end{pmatrix}. \tag{2.30}$$

2.2.2 Effect of Matter on Neutrino Oscillations

We now consider how the evolution of a neutrino state can be affected by its interactions with matter. We will show that such interactions in some cases can dramatically change the neutrino survival probability.

Neutrinos interact with matter through charged and neutral current weak interactions, Eqs. (2.15, 2.16). As an example, we will analyze the neutrino–electron scattering. This process will be important later when we discuss the neutrino evolution inside the Sun. The Feynman diagrams for the elastic $\nu_e e$ scattering are shown in Fig. 2.1. The amplitude corresponding to the charged current diagram is

$$i\mathcal{M}_{CC} = \frac{ig}{\sqrt{2}}(\bar{e}_{fL}\gamma_\mu \nu_i) \times \frac{-ig^{\mu\nu}}{p^2 - M_W^2} \times \frac{ig}{\sqrt{2}}(\bar{\nu}_f \gamma_\nu e_{iL}), \tag{2.31}$$

while for the neutral current diagram it is

$$\begin{aligned} i\mathcal{M}_{NC} &= \frac{ig}{\cos\theta_W}\frac{1}{2}(\bar{\nu}_f\gamma_\mu\nu_i) \\ &\quad \times \frac{-ig^{\mu\nu}}{p^2 - M_Z^2} \times \frac{ig}{\cos\theta_W}(T^{(3)} - Q\sin^2\theta_M) J_\nu^{(0)}(e,p,n)_{L,R}, \end{aligned} \tag{2.32}$$

where $J_\nu^{(0)}(e,p,n)_{L,R}$ refer to the neutral currents of left- and right-handed components of electrons, protons, and neutrons.

For low energy neutrinos, such as solar neutrinos, the vector boson propagators are dominated by the mass terms M_W^2 and M_Z^2. Then the amplitudes in Eqs. (2.31)

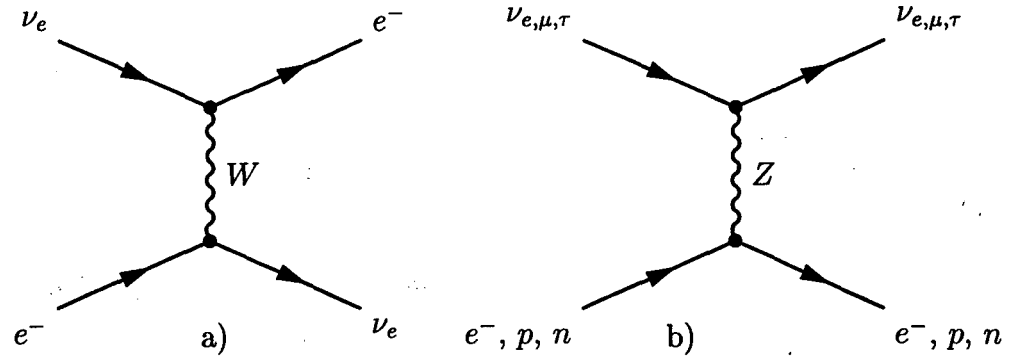

Figure 2.1: Feynman diagrams for neutrino elastic scattering processes via charged (a) and neutral (b) current interactions.

and (2.32) can be written as the four-fermion interactions:

$$\begin{aligned} i\mathcal{M}_{CC} &= \frac{-ig^2}{8M_W^2}(\bar{e}_f\gamma_\mu(1-\gamma^5)\nu_i)(\bar{\nu}_f\gamma^\mu(1-\gamma^5)e_i), \\ i\mathcal{M}_{NC} &= \frac{-ig^2}{M_Z^2\cos^2\theta_W}(\bar{\nu}_f\gamma_\mu\nu_i)(T^{(3)}-Q\sin^2\theta_M)J_\nu^{(0)}(e,p,n)_{L,R}. \end{aligned} \tag{2.33}$$

Comparing this to the traditional expression for the Fermi interactions,

$$\begin{aligned} i\mathcal{M}_{CC} &= \frac{-iG_F}{\sqrt{2}}(\bar{e}_f\gamma_\mu(1-\gamma^5)\nu_i)(\bar{\nu}_f\gamma^\mu(1-\gamma^5)e_i), \\ i\mathcal{M}_{NC} &= \frac{-iG_F}{\sqrt{2}}(\bar{\nu}_f\gamma_\mu\nu_i)(T^{(3)}-Q\sin^2\theta_M)J_\nu^{(0)}(e,p,n)_{L,R}, \end{aligned} \tag{2.34}$$

we see that $G_F = g^2/(4\sqrt{2}M_W^2)$. (The second equation in (2.34) is satisfied because of Eq. (2.22).)

We we will first analyze the most obvious consequence of neutrino interaction with matter, the scattering phenomenon. As was already discussed in Section 2.1.1, the interaction cross section is very small. As an example we will next consider the scattering cross section for neutrino scattering on electrons. It is possible to guess the answer based on simple dimensional analysis. Since the scattering amplitude is proportional to G_F, the cross section must contain G_F^2. To obtain the correct

dimension for the cross section, we can multiply this by the center of mass energy s. Thus, $\sigma \sim G_F^2 s = G_F^2 2 m_e E_{\nu_i}$. For neutrino energy of 1 MeV, this yields $\sigma \sim 10^{-44}$ cm^2, a tiny cross section indeed!

Given the amplitudes in Eqs. (2.34), we can obtain a more accurate answer. Upon averaging over the electron helicity states, we find

$$\overline{|\mathcal{M}|^2} = 128 G_F^2 (g_L^2 (p_{e_i} k_{\nu_i})^2 + g_R^2 (p_{e_i} k_{\nu_f})^2 - g_L g_R m^2 (k_{\nu_i} k_{\nu_f})), \tag{2.35}$$

where the notation

$$\begin{aligned} g_L &= \frac{1}{2} + \sin^2 \theta_W, \\ g_R &= \sin^2 \theta_W \end{aligned} \tag{2.36}$$

was introduced. The corresponding differential cross section for the $e\nu$ scattering is

$$\frac{d\sigma}{dT} = \frac{2 G_F^2 m_e}{\pi} \left[g_L^2 + g_R^2 \left(1 - \frac{T}{E_{\nu_i}} \right)^2 - g_L g_R \frac{m_e T}{E_{\nu_i}^2} \right], \tag{2.37}$$

where T denotes the energy of the outgoing electrons. Simple kinematics shows that it is related to the scattering angles $\theta_{\rm lab}$ in the lab frame and $\theta_{\rm CM}$ in the center of mass frame by

$$T = \frac{E_{\nu_e}^2 (1 - \cos \theta_{\rm lab})}{m_e + E_{\nu_e} (1 - \cos \theta_{\rm lab})}, \tag{2.38}$$

$$T = \frac{E_{\nu_e}^2}{m_e + 2 E_{\nu_e}} (1 - \cos \theta_{\rm CM}), \tag{2.39}$$

and hence T varies from $T_{\rm min} = 0$ to $T_{\rm max} = E_{\nu_e} / [1 + m_e / (2 E_{\nu_e})]$.

The first term in Eq. (2.37) comes from both charged and neutral current interactions of the left-handed component of the electron e_L, while the second term is due

to the neutral current interaction of its right-handed component e_R. The last term is the cross term between the two. It is proportional to the electron mass m_e and would vanish if $m_e \to 0$ (or, more to the point, $m_e \ll E_{\nu_i}$). This is behavior is expected, because in this limit e_L and e_R behave as two totally different particles.

Eq. (2.37) confirms that our estimate for the order of magnitude of the neutrino cross section was correct. The smallness of neutrino cross section with matter makes it possible for neutrinos produced in the core of the Sun to travel to the surface of the Sun undeflected. Only in the core of a supernova is the density high enough that the material there becomes opaque to (anti)neutrinos with energies of a few MeV.

There is, however, another effect of neutrino–matter coupling which was pointed out in [11]. Although neutrinos freely propagate in the medium, the interaction in question can lead to an effective *index of refraction* of the medium for neutrinos.

First, consider a single neutrino flavor propagating in the the solar or earth matter. According to a well-known result in optics, the index of refraction of a medium n is related to the forward scattering amplitude $f(0)$ of the scatterers that make up the medium by

$$n = 1 + \frac{2\pi N}{k^2} f(0), \tag{2.40}$$

where k is a wave number and N is the number density of the scatterers. The derivation of this formula can be found in A.1. Physically, it happens because the scattering phenomenon changes the group velocity of neutrinos in the medium. But the same effect can be achieved also by varying the mass of the neutrinos. Indeed,

the group velocity for massive neutrinos in vacuum is

$$v_{\rm gr} = \frac{dE}{dp} = \frac{p}{\sqrt{p^2+m^2}} \simeq 1 - \frac{m^2}{2p^2}. \tag{2.41}$$

By comparing Eqs. (2.40) and (2.41) we can see that the effect of index of refraction can be represented if m^2 is changed by

$$\delta m^2_{\rm mat} = 4\pi N f(0). \tag{2.42}$$

The value of $f(0)$ can be found either by starting from the Feynman diagrams, or, more quickly, by using the expression for the scattering cross section, Eq. (2.37). One is cautioned, however, against a naive application of the formula

$$|f(0)|^2 = \frac{d\sigma}{2\pi d\cos\theta}, \tag{2.43}$$

which leads to an incorrect result[2]. The reason for this subtlety is that the cross section in Eq. (2.37) is averaged over the spin states of the electron. To get the correct answer, in Eq. (2.42) we must use the average *amplitude*. The answer is:

$$\delta m^2_{\rm mat} = 2\sqrt{2}G_F N_e E_\nu - \sqrt{2}G_F N_n E_\nu. \tag{2.44}$$

Here N_e and N_n are the electron and neutron number densities in the medium. The first term is due to scattering by the charged current interaction, while the second one is the neutral current contribution. Notice that the neutral current contributions of electrons and protons cancel each other out if the medium is electrically neutral.

[2]This mistake was indeed made in the original paper [11]. As a result, the matter term in that paper is off by a factor of $\sqrt{2}$. (It furthermore has a wrong sign.)

For the muon and tau neutrinos elastic forward scattering can only occur through the neutral current interaction. Consequently, the value of $\delta m^2_{\rm mat}$ for them is given by

$$(\delta m^2_{\rm mat})_{\mu,\tau} = -\sqrt{2} G_F N_n E_\nu. \tag{2.45}$$

Using Eq. (2.44), we can estimate the order of magnitude of the index of refraction of a typical medium for neutrinos. Taking the electron number density to be $N_e = 10^{24}$ cm^{-3}, for the neutrino energy of 1 MeV we obtain $n - 1 = \sqrt{2} G_F N_e / E_\nu \sim 10^{-19}$. Hence, there is no hope to measure neutrino ray bending as a result of it passing through the Earth.

Thus, if there was only one neutrino generation, the modification of the index of refraction by the neutrino–matter interactions would have no observable consequences. The situation, however, can be very different in the presence of two or more generations, which can mix according to Eq. (2.27). In this case, the index of refraction can have a profound effect on both the mixing angle and the mass splitting between the levels. This can be seen if we write down the Hamiltonian for neutrinos in matter. To simplify the presentation, we will once again limit our consideration to only two generations, for definiteness ν_e and ν_μ, and also assume that the density of the medium is uniform. Taking into account the contribution of Eq. (2.42), with

$f(0)$ given by Eqs. (2.44) and (2.45), we obtain

$$H = p_\nu + \frac{m^2_{\rm sum}}{4p_\nu} - \sqrt{2}G_F N_n/2 + \begin{pmatrix} -\frac{\Delta m^2}{4p_\nu}\cos 2\theta + \sqrt{2}G_F N_e & \frac{\Delta m^2}{4p_\nu}\sin 2\theta \\ \frac{\Delta m^2}{4p_\nu}\sin 2\theta & \frac{\Delta m^2}{4p_\nu}\cos 2\theta \end{pmatrix}. \tag{2.46}$$

Here $m^2_{\rm sum} \equiv m_2^2 + m_1^2$. The eigenvalues of this Hamiltonian are

$$\lambda_\pm = p_\nu + \frac{m^2_{\rm sum}}{4p_\nu} + \frac{\sqrt{2}G_F(N_e - N_n)}{2} \pm \frac{1}{2}\left[\left(\frac{\Delta m^2}{2p_\nu}\right)^2 + \left(\sqrt{2}G_F N_e\right)^2 - \frac{\Delta m^2}{p_\nu}\sqrt{2}G_F N_e \cos 2\theta\right]^{1/2}. \tag{2.47}$$

For the study of neutrino oscillations, terms common to both states are irrelevant, and the first three terms can be dropped. One can also safely replace p_ν by E_ν in the remainder. The eigenstates of this Hamiltonian in terms of flavor eigenstates are

$$|\nu_-\rangle = \cos\theta_M |\nu_e\rangle - \sin\theta_M |\nu_\mu\rangle, \tag{2.48}$$

$$|\nu_+\rangle = \sin\theta_M |\nu_e\rangle + \cos\theta_M |\nu_\mu\rangle. \tag{2.49}$$

Here θ_M is the matter mixing angle, given by

$$\cos 2\theta_M = \frac{\Delta m^2 \cos 2\theta - 2E_\nu\sqrt{2}G_F N_e}{\sqrt{(\Delta m^2)^2 + (2E_\nu\sqrt{2}G_F N_e)^2 - 4\Delta m^2 E_\nu \sqrt{2}G_F N_e \cos 2\theta}}. \tag{2.50}$$

Thus, the presence of matter can change both the mixing angle and the mass-squared splitting between the eigenstates. For example, if the matter term $\sqrt{2}G_F N_e$ is much greater than the vacuum splitting $\Delta m^2/2E_\nu$, the amplitude of the flavor

oscillations in matter will be suppressed compared to the vacuum case. This indeed happens for solar neutrinos in the core of the Sun for a wide range of the parameters (first pointed out by Wolfenstein in [11]).

Additionally, in the case of varying matter density it is possible to obtain neutrino survival probability very different from those in vacuum. The two most striking mechanisms are the phenomenon of parametric resonance [12, 13, 14] and the so-called MSW effect [15, 16]. The former can be relevant for neutrino regeneration in the Earth, the phenomenon studied in Chapter 4. The latter plays a crucial role in one of the explanations for the solar neutrino deficit. We will discuss it in detail in Sect. 2.3.3, after providing some background on the Standard Solar Model and solar neutrino experiments.

2.3 The Solar Neutrino Problem

Sun gets its energy from nuclear reactions that take place in its core. The net result of these reaction is the conversion of hydrogen into helium nuclei. A few of these reactions produce neutrinos, which then travel through the Sun virtually unscattered. Several terrestrial experiments have been deployed to measure this solar neutrino flux, and more are under development. The existing experiments rely on different techniques to measure neutrino flux and are sensitive to different energy components. Nonetheless, all experiments report seeing a deficit in the observed neutrino flux, compared to the predictions of the Standard Solar Model. This discrepancy between

the theory and experiment is known as the solar neutrino problem. Understanding the solar neutrino problem would provide us with a unique opportunity to study the physics of solar interior. At the same time, if the resolution involves neutrino oscillations, it would be a major breakthrough in neutrino physics and particle physics in general.

Our presentation in this section is organized as follows. In 2.3.1 we review the foundations of the Standard Solar Model and its predictions on the solar neutrino fluxes. In 2.3.2 we describe the solar neutrino experiments. In 2.3.3 we present a synopsis of the standard analysis of solar neutrino data in terms of neutrino oscillations. Finally, in 2.3.4 we discuss some of the future experiments and argue for the need of "smoking gun" evidence to prove that the observed solar neutrino deficit is indeed due to neutrino oscillations.

2.3.1 The Standard Solar Model

The Sun is a typical middle-aged main sequence star. Its interior is in a long-lived quasistatic equilibrium, supported by the energy released as hydrogen is converted into helium. This conversion occurs in two chains of reactions, the *proton-proton (pp) chain* and the *carbon-nitrogen-oxygen (CNO) cycle*, shown in Figs. 2.2 and 2.3 correspondingly. A detailed analysis shows that for a star with the mass of the Sun the *pp* chain is dominant [3].

[3]For the CNO chain to be dominant, the core temperature in a star must be higher than about 16 million K. Such temperatures are achieved in stars with masses $\gtrsim 1.1 M_{\odot}$

To compute the parameters of the interior of the Sun, it is necessary to create a model of stellar evolution. Such a model starts with a chemically homogeneous spherical object of total mass $M_\odot$ and then applies the following four principles of stellar evolution [17]:

- The Sun is assumed to be in hydrostatic equilibrium throughout its evolution.
- Energy is generated by nuclear reactions in the Sun's core.
- These reactions are the sole cause of element abundance changes in the Sun.
- Energy is transported by photons or by convective motion.

After about 4.6 billion years of evolution (the age of the Sun) the model must reproduce the present day solar luminosity $L_\odot$ and radius $R_\odot$, as well as predict the present day parameters, such as densities, temperature distribution and element abundances in the interior, the spectrum of acoustic frequencies observed on the solar surface, and, very importantly, the neutrino fluxes.

Modern solar models built in this way are generally found to be in very good agreement with measurements. For example, the model by Bahcall and Pinsonneault, BP98 [4], predicts sound speeds which are in excellent agreement with the results obtained from helioseismology, as illustrated in Fig. 1 of reference [4][4]. To date, only the neutrino flux predictions of the model are found to be in direct contradiction with

[4]The largest discrepancy between the model and the data occurs at $R = 0.7R_\odot$, on the boundary between the radiative and convective zones. This discrepancy is too small to account for the observed deficit of solar neutrino flux by modifying the core temperature of the Sun.

the data, as will be described in Section 2.3.3.

Reaction	Abbr.	Max neutrino energy, MeV	Comments
$p + p \rightarrow {}^2H + e^+ + \nu_e$	*pp*	0.42	continuous
$p + p + e^- \rightarrow {}^2H + \nu_e$	*pep*	1.442	discrete
${}^3He + p \rightarrow {}^4He + \nu_e$	*hep*	18.77	discrete
${}^7Be + e^- \rightarrow {}^7Li + \nu_e$	^{7}Be(I)	0.863	90% of time, discrete
${}^7Be + e^- \rightarrow {}^7Li^* + \nu_e$	^{7}Be(II)	0.383	10% of time, discrete
${}^8B \rightarrow {}^8Be^* + e^+ + \nu_e$	^{8}B	15	continuous
${}^{13}N \rightarrow {}^{13}C + e^+ + \nu_e$	^{13}N	1.20	continuous
${}^{15}O \rightarrow {}^{15}N + e^+ + \nu_e$	^{15}O	1.73	continuous
${}^{15}F \rightarrow {}^{17}O + e^+ + \nu_e$	^{15}F	1.74	continuous

Table 2.1: Maximum energies of the neutrinos produced in the Sun's core.

Neutrinos are produced in both the *pp* and the *CNO* chains. As was already mentioned, for the Sun the *pp* chain is dominant. The reactions that make up the the *pp* chain are illustrated in Fig. 2.2. The vast majority of solar neutrinos come from the first reaction, the proton-proton fusion (see Table 2.2). These neutrinos, however, have relatively low energies, as shown in Table 2.1, and cannot be seen at all solar neutrino experiments. Thus, ^{7}Be(I) and ^{8}B neutrinos are also experimentally important, despite the fact that they occur only in 15% and 0.02% of all terminations of the chain correspondingly. The other two neutrino–producing reactions in the chain, the *pep* and *hep* neutrinos, are of lesser importance[5].

The *CNO* cycle is depicted in Fig. 2.3. Despite very different appearance from

[5]One of the explanations of the observed recoil electron spectrum at Super-Kamiokande involves the *hep* neutrinos. This, however, requires that their flux would be 20 times higher than predicted by BP98 [18].

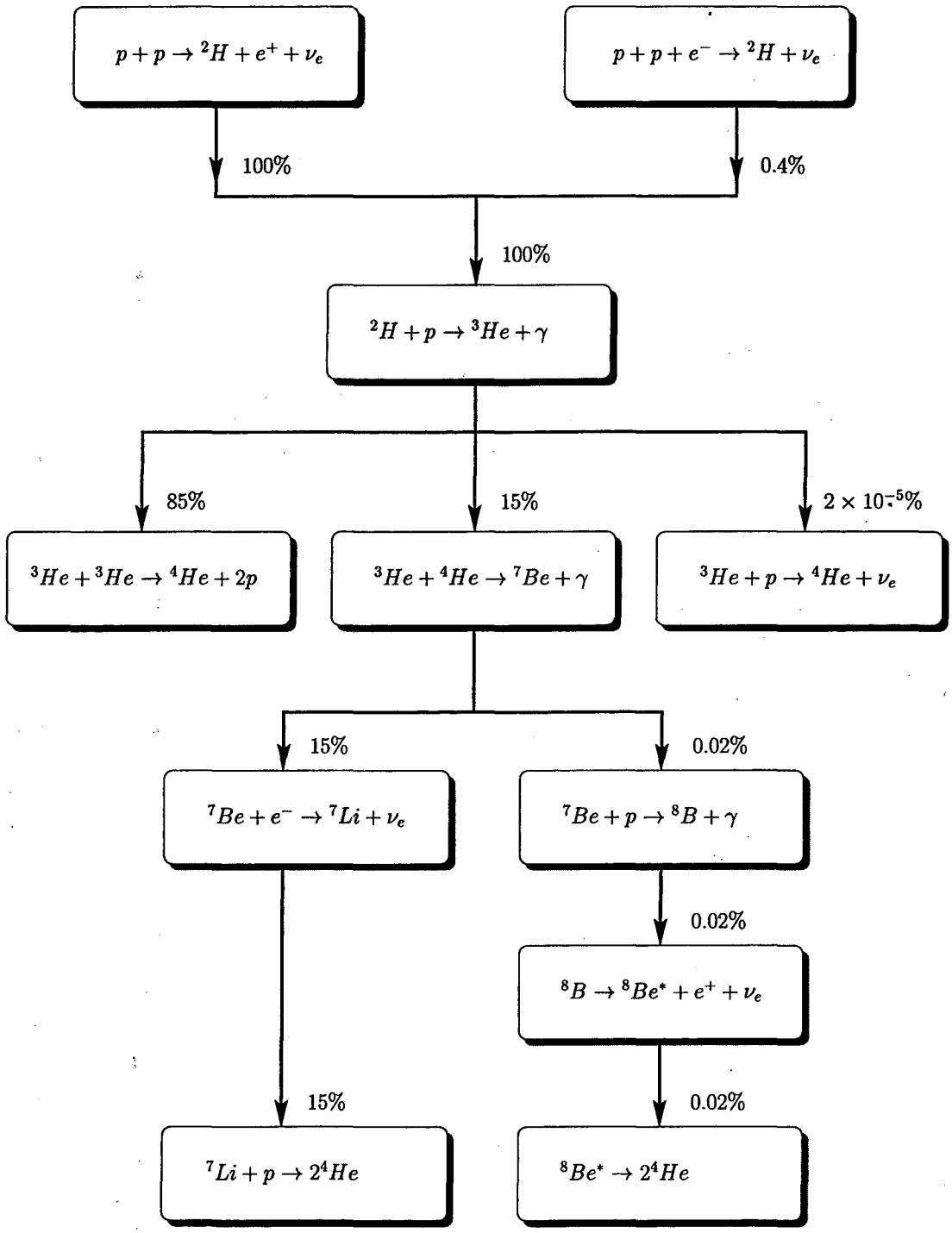

Figure 2.2: The *pp* chain in the Sun. The percentages shown represent the fraction of terminations of the chain in which each reaction occurs, averaged over the neutrino production region.

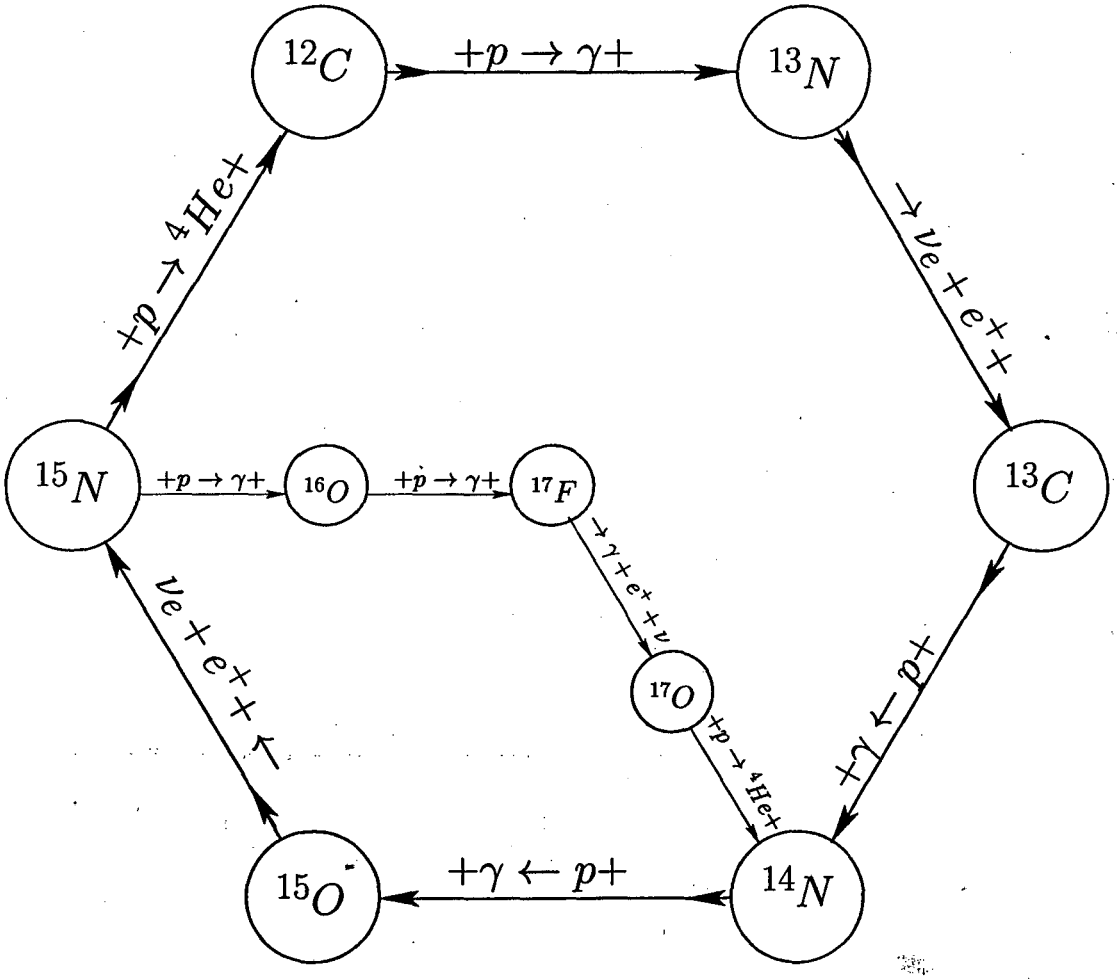

Figure 2.3: The *CNO* cycle in the Sun.

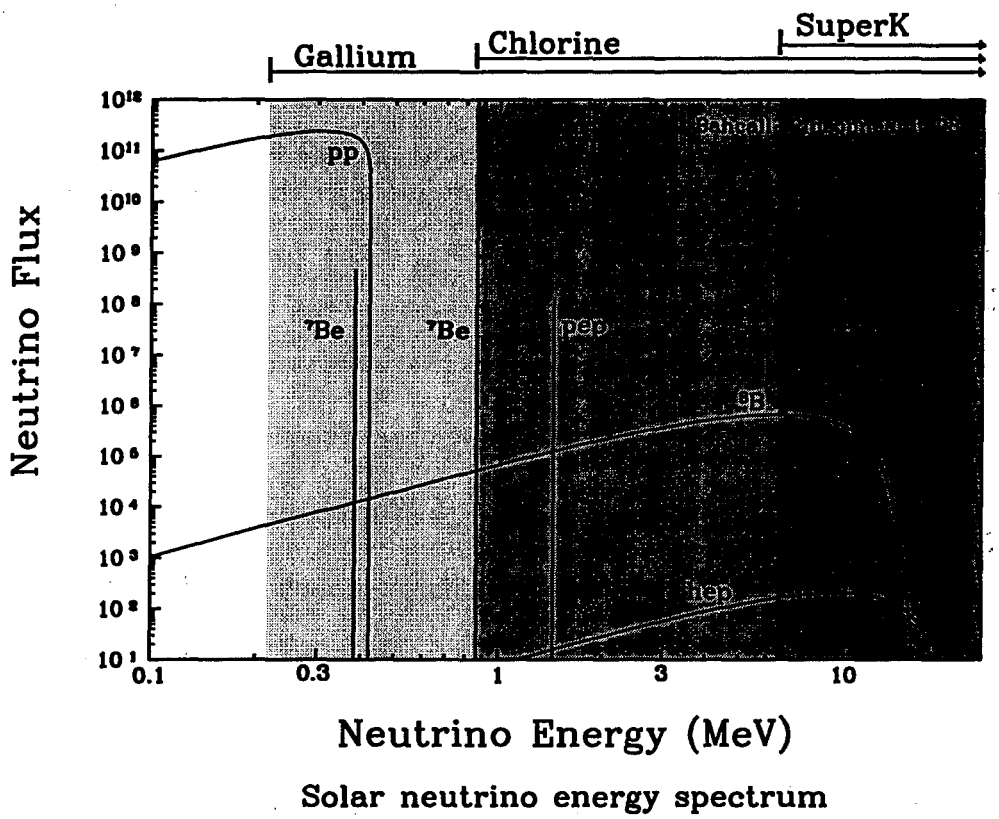

Solar neutrino energy spectrum

Figure 2.4: Solar neutrino spectrum according to BP98 solar model. Only the *pp* chain reactions are shown.

Source	Flux (10^{10} cm^{-2}s^{-1})	Cl (SNU)	Ga (SNU)
pp	5.94	0.0	69.6
pep	1.39×10^{-2}	0.2	2.8
hep	2.10×10^{-7}	0.0	0.0
^{7}Be	4.80×10^{-1}	1.15	34.4
^{8}B	5.15×10^{-4}	5.9	12.4
^{13}N	6.05×10^{-2}	0.1	3.7
^{15}O	5.32×10^{-2}	0.4	6.0
^{17}F	6.33×10^{-4}	0.0	0.1
Total		$7.7^{+1.2}_{-1.0}$	129^{+8}_{-6}

Table 2.2: Solar neutrino flux predictions (BP98), with 1σ uncertainties from all sources. Also shown are neutrino capture rates for chlorine and gallium experiments (see Sect. 2.3.2).

the *pp* chain, the net result of the *CNO* cycle is also to convert hydrogen into ^{4}He. The carbon, nitrogen, and oxygen that appear in the reaction do not get used up, and only serve as catalysts. Two of the reactions in the primary loop produce neutrinos, the β–decays of ^{13}N and ^{15}O. The secondary loop, shown within the primary cycle, connects the ^{15}N, ^{16}O, ^{17}F, and ^{17}O. The contribution of the neutrinos produced in this loop to the overall flux is negligible (see Table 2.2).

The energy spectra of the *pp* chain reactions are shown in Fig. 2.4. Notice, that the spectra of the *pp*, ^{8}B and *hep* neutrinos are quite broad, while the ^{7}Be and *pep* neutrinos, which are produced in a two-body final state, are virtually monochromatic. The shape of the spectrum of each reaction is dictated by kinematics and cannot be changed by modifying the solar model. Any such modifications only affect the overall normalization of each component. For example, these normalizations depend on the

central temperature in the following way: [17]:

$$\begin{aligned} \phi(pp) &\propto T^{-1.2}, \\ \phi(^7\mathrm{Be}) &\propto T^{8}, \\ \phi(^8\mathrm{B}) &\propto T^{18}. \end{aligned} \tag{2.51}$$

Thus, ^{8}B flux is the most sensitive to T, while pp is relatively insensitive.

On the other hand, the observed neutrino flux appears to exhibit not only an overall suppression, but a pattern of suppression of individual components which is energy-dependent. Neutrino oscillation explanation of the solar neutrino problem can in fact accommodate such a distortion of the observed neutrino flux. This will be discussed in Section 2.3.3. An experimental conformation of such distortions would be one of the "smoking gun" signatures of neutrino oscillations. This and other signatures will be discussed in Section 2.3.4.

2.3.2 The Solar Neutrino Experiments

To measure the solar neutrino flux several experiments have been built. These experiments include the Homestake experiment, the SAGE and GALLEX experiments, and the Kamiokande Super-Kamiokande experiments. All these experiments have large targets and are located deep underground to shield the targets from cosmic rays. This section contains a brief overview of the principles of operation of each of these experiments. In the next section we will discuss how the data accumulated by

these experiments compare with the predictions of the Standard Solar Model.

The Homestake experiment is the oldest of all solar neutrino detectors. Constructed in late 1960's, for two decades it was the only operating solar neutrino experiment. The detection principle is based on the reaction

$$\nu_e + {}^{37}\mathrm{Cl} \rightarrow e^- + {}^{37}\mathrm{Ar}, \tag{2.52}$$

with a threshold of 0.814 MeV. This value of the threshold renders the experiment insensitive to the abundant *pp* neutrinos. However, the ^{7}Be and ^{8}B neutrinos (as well as the *pep* and *CNO* neutrinos) are within its sensitivity range.

The target is a 100,000-gallon tank of perchloroethylene C_2Cl_4, a cleaning fluid, located 4850 ft underground in the Homestake Gold Mine in Lead, South Dakota. Periodically, usually once every one to three months[6], the argon in the tank is removed by purging the tank with helium. The argon atoms are absorbed by the charcoal trap maintained at the temperature of liquid nitrogen. The trap is subsequently heated and the extracted argon is purified and loaded in a small proportional counter. As a result of this procedure, on the order of 15 (!) ^{37}Ar atoms are extracted out of the total of more than 10^{30} atoms in the tank.

The extraction efficiency was tested by placing a small neutron source at the center of the tank and counting the number of ^{37}Ar atoms in the tank produced as a result, and also by introducing a measured number of ^{37}Ar atoms in the detector and then removing them. The extraction efficiency was shown to be at least 90%.

[6]The half-life of ^{37}Ar is 35 days, so after a few months the equilibrium number of argon-37 atoms is established.

That one can extract 15 atoms from a 100,000-gallon tank of a cleaning fluid with 90% efficiency is simply astounding!

As can be seen from Table 2.2, the SSM predicts that the majority of the ^{37}Ar atoms are expected to be created by the ^{8}B neutrinos, while the ^{7}Be neutrinos contribute about 15% of the total rate.

As was already mentioned, the Homestake experiment is insensitive to the low energy *pp* neutrinos. Gallium experiments were designed to eliminate this shortcoming. The solar neutrinos are captured in the reaction

$$\nu_e + {}^{71}\mathrm{Ga} \rightarrow e^- + {}^{71}\mathrm{Ge}, \tag{2.53}$$

which has a threshold of only 0.233 MeV. The radioactive ^{71}Ge has a half-life of 11.43 days and decays by electron capture. As shown in Table 2.2, in the absence of oscillations over a half of all neutrinos detected at these experiments are expected to come from the basic *pp* reaction.

The GALLEX detector is located in the Gran Sasso Underground Laboratory in Italy. The detector consists of a concentrated $GaCl_3$-HCl solution containing 30 tons of gallium. Neutrino interactions convert gallium nuclei into ^{71}Ge nuclei, which subsequently form the $GeCl_4$ molecules. Periodically, $GeCl_4$ is removed from the solution and, after a series of manipulations, germanium nuclei are transferred in the gas germane GeH_4. The resulting gas is then introduced into a small proportional counter, where the number of radioactive ^{71}Ge nuclei is measured.

The Soviet-American-Gallium-Experiment (SAGE) is located underneath a high

mountain in the Baksan river valley in the North Caucus region of Russia. It uses 60 tons of gallium and, unlike the GALLEX experiment, the target is in metal form. Gallium metal melts at about 30° C, permitting the extraction of the germanium. Although more cumbersome, after the first several extraction steps the chemical processing and counting techniques are quite similar to those used in GALLEX. To appreciate the scale of both experiments, it should be kept in mind that at the time the experimental techniques were being developed, the total world production of gallium was only 10 tons per year!

The two experimental techniques each have certain advantages and disadvantages, which are to some degree complementary. It is therefore encouraging that solar neutrino fluxes reported by both experiments are consistent within the error bars (the values are $79 \pm 10 \pm 6$ SNU for GALLEX and $79 \pm 10 \pm 6$ SNU for SAGE).

The Kamiokande experiment, which was launched on January 1987 and later superseded by its larger version, called Super-Kamiokande, is based on a completely different detection principle. Both experiments are basically very large tanks of water (Super-Kamiokande detector is 40 meters in diameter and 40 meters tall) located at a depth of 2700 meters water equivalent in the Kamioka Mozumi mine in Japan. The primary mode of interaction of neutrinos in the detector is the elastic scattering on electrons:

$$\nu_i + e_i^- \rightarrow \nu_f + e_f^- . \tag{2.54}$$

The recoil electrons produce Cherenkov light in the detector, which is measured by

photomultiplier tubes surrounding the fiducial volume of the detector. Thus, unlike the previously considered radiochemical experiments, the Kamiokande and Super-Kamiokande experiments are known as the water Cherenkov detectors.

Because the recoil electrons should be energetic enough to produce Cherenkov light, and most importantly, because the signal from the low energy electrons is swamped by the background from radon dissolved in the water, the water Cherenkov experiments are sensitive only to the high energy ^{8}B neutrinos. This drawback of the technique is, however, outweighed by several very important advantages. First, the orientation of the Cherenkov cone provides a directional information on the incoming neutrino. The Kamiokande was the first experiment to unequivocally demonstrate that neutrinos are indeed coming from the Sun. Second, the detection is carried out is real time, making it possible to look for seasonal and day–night variations in the event rate. Finally, if the detector is well calibrated, one can obtain not only the integrated flux, but also the energy spectrum of the ^{8}B solar neutrinos.

The Kamiokande experiment was originally built to look for proton decay. In 1984 it was decided to improve the detector to make possible the study of the relatively low-energy events induced by solar neutrinos. The upgrades were completed just in time to allow the observation of neutrinos from the supernova SN1987A, an incredibly lucky coincidence, considering the fact that a similar supernova event may occur with a frequency on the order of 100 years. The supernova neutrinos have energies comparable to those of the ^{8}B solar neutrinos.

In addition to solar neutrinos, Kamiokande and Super-Kamiokande have the capability to study the atmospheric neutrinos. These neutrinos are produced by the cosmic rays interacting in the upper atmosphere and include both electron and muon neutrinos and antineutrinos. The results from the study of atmospheric neutrinos indicate that muon neutrinos may be oscillating into some other neutrino type, thus providing the strongest evidence we have to date for new physics beyond the Standard Model.

At present Super-Kamiokande is the state-of-the-art solar neutrino experiment. Over the past several years it has accumulated a large amount of data. This data, combined with the results from the Homestake and gallium experiments provide a strong hint for solar neutrino oscillations. This analysis will be presented in the next subsection.

2.3.3 Comparison of Theory and Experiments: MSW and Vacuum Oscillation Solutions

All solar neutrino experiments described in the previous section report seeing a deficit of solar neutrinos. Gallium and water Cherenkov detectors measure a flux equal to a half of the expected value, while the Homestake experiment measures only about a third of what is predicted. The experimentally measured event rates and uncertainties, as well as the standard solar model predictions are summarized in Table 2.3.

Experiment	Experimental rate	Ref.	Theoretical rate	Units
Homestake	$2.56 \pm 0.16 \pm 0.16$	[19]	$7.7\ ^{+1.2}_{-1.0}$	SNU
SAGE	$67.2\ ^{+7.2\ +3.5}_{-7.0\ -3.0}$	[20]	$129\ ^{+8}_{-6}$	SNU
GALLEX	$77.5 \pm 6.2\ ^{+4.3}_{-4.7}$	[21]	$129\ ^{+8}_{-6}$	SNU
Kamiokande	$2.80 \pm 0.19 \pm 0.33$	[22]	$5.15\ ^{+1.0}_{-0.7}$	10^6 cm^{-2} s^{-1}
Super-Kamiokande	$2.45 \pm 0.04 \pm 0.07$	[23]	$5.15\ ^{+1.0}_{-0.7}$	10^6 cm^{-2} s^{-1}

Table 2.3: Solar neutrino fluxes observed by Homestake, SAGE, GALLEX, Kamiokande, and Super-Kamiokande (825 days, $E_e > 6.5$ MeV), as compared with the theoretical expectations of the BP98 standard solar model [4]. The errors are quoted at 1σ.

If one accepts the results of all five experiments, it is very difficult, if not impossible, to devise an explanation of the observed deficit by only modifying the solar model. This is because, as mentioned earlier, the shapes of neutrino spectra from individual reactions are fixed by kinematic and, in the absence of oscillations, the only freedom one has is to adjust the overall normalization of each reaction. After going through a simple exercise, one finds that to satisfy the Super-Kamiokande result the ^{8}B flux can be suppressed by a factor of 1/2. Then, the remaining half of the ^{8}B flux is enough to explain the rate seen by the Homestake experiment and there is no room for the ^{7}Be neutrinos. (In fact, the best fit value for the ^{7}Be flux in this case turns out to be negative.)

On the other hand, neutrino oscillations provide a simple and logically appealing explanation of all experimental data. The solutions traditionally have been classified into two category, MSW solutions or vacuum oscillation solutions. The former relies on the matter enhanced flavor conversion in the Sun, while the latter uses simple long–wavelength oscillations in vacuum to achieve the observed energy dependent

suppression of the solar neutrino flux.

We will first discuss the MSW mechanism. Using the position dependent modification of the Hamiltonian (2.46),

$$H(r) = p_\nu + \frac{m^2_{\rm sum}}{4p_\nu} - \sqrt{2}G_F N_n(r)/2 + \begin{pmatrix} -\frac{\Delta m^2}{4p_\nu}\cos 2\theta + \sqrt{2}G_F N_e(r) & \frac{\Delta m^2}{4p_\nu}\sin 2\theta \\ \frac{\Delta m^2}{4p_\nu}\sin 2\theta & \frac{\Delta m^2}{4p_\nu}\cos 2\theta \end{pmatrix}, \tag{2.55}$$

for neutrinos propagating inside the Sun, it is relatively simple to estimate the survival probability for electron neutrinos that are created in the Sun's core and are detected on the Earth, in the limit that $\Delta m^2/2E_\nu$ is much smaller than the Earth-Sun distance, such that oscillations in vacuum between ν_1 and ν_2 states are "averaged out"[7]. There are four possible "propagation paths" that the solar neutrino can follow:

$$\begin{aligned}
\nu_e &\rightarrow \nu^+(p = \sin^2\theta_\odot) \rightarrow \nu_2(p = 1 - P_c) \rightarrow \nu_e(p = \sin^2\theta) \\
&\text{or} \\
\nu_e &\rightarrow \nu^+(p = \sin^2\theta_\odot) \rightarrow \nu_1(p = P_c) \rightarrow \nu_e(p = \cos^2\theta) \\
&\text{or} \\
\nu_e &\rightarrow \nu^-(p = \cos^2\theta_\odot) \rightarrow \nu_1(p = 1 - P_c) \rightarrow \nu_e(p = \cos^2\theta) \\
&\text{or} \\
\nu_e &\rightarrow \nu^-(p = \cos^2\theta_\odot) \rightarrow \nu_2(p = P_c) \rightarrow \nu_e(p = \sin^2\theta),
\end{aligned} \tag{2.56}$$

where p is the probability that a given "step" takes place, ν^+ and ν^- are the heavy

[7]That this is indeed the case will be demonstrated later in Sect. 3.2.

and light mass eigenstates at the production point in the core, $\theta_\odot = \theta_M(0)$ and P_c is the level crossing probability, *i.e.* the probability that during the evolution from the Sun's core to vacuum the neutrino changes from one set of instantaneous Hamiltonian eigenstates to the other.

Therefore, the probabilities of finding the mass eigenstates ν_1 and ν_2 far from the Sun are given by

$$P_1 = \sin^2\theta_\odot P_c + \cos^2\theta_\odot(1 - P_c) \tag{2.57}$$

$$P_2 = 1 - P_1, \tag{2.58}$$

where $\theta_\odot$ is the mixing angle at the production point[8], and the electron neutrino survival probability (P_{ee}) at the surface of the Earth is

$$\begin{aligned} P_{ee} &= P_1\cos^2\theta + P_2\sin^2\theta \\ &= \sin^2\theta_\odot((1 - P_c)\sin^2\theta + P_c\cos^2\theta) \\ &+ \cos^2\theta_\odot((1 - P_c)\cos^2\theta + P_c\sin^2\theta). \end{aligned} \tag{2.59}$$

All equalities hold as long as the two mass eigenstates appear as an incoherent mixture (true for $\Delta m^2 \gtrsim 10^{-8}$ eV^2 for ^{7}Be neutrinos). Note also that in deriving Eq. (2.59) no assumption was made with respect to the value of $\cos 2\theta$, and therefore it should be valid for the entire range of $0 \leq \sin^2\theta \leq 1$. This fact will be important in Chapter 4.

[8]In our numerical analyses later, we integrate over the production region using the profile given in [24]. The interference between ν_+ and ν_- states in Eq. (2.56) vanishes upon averaging over the production region independent of Δm^2 or energy.

If the two mass eigenstates are not incoherent (true for $\Delta m^2 \lesssim 10^{-8}$ eV^2 for ^{7}Be neutrinos), Eq. (2.59) is modified to [25, 26]

$$P_{ee} = P_1 \cos^2\theta + P_2 \sin^2\theta - \sqrt{P_c(1-P_c)} \cos 2\theta_\odot \sin 2\theta \cos\left(2.54 \frac{\Delta m^2 L}{E_\nu} + \delta\right), \tag{2.60}$$

where L is the distance from the Sun to the surface of the Earth, in km, E_ν is in GeV, Δm^2 in eV^2, and δ is a matter induced phase, given in [25]. Physical consequences of the matter phase have been discussed in [27]. Eq. (2.60) is valid for a fixed neutrino energy. For ^{7}Be neutrinos, the integration over the width of the neutrino energy line leads to a suppression of the oscillatory terms already at $\Delta m^2 \simeq$ a few $\times 10^{-10}$ eV^2.

Assuming an exponential profile for the electron number density inside the Sun ($N_e(r) = N_e(0)\exp(-r/r_0)$), Schrödinger's equation can be solved analytically [28, 29], and it is shown that, in the range of the neutrino oscillation parameter space relevant for addressing the solar neutrino puzzle, Eq. (2.59) is indeed a very good approximation for P_{ee} and that P_c is given by [29, 30]

$$P_c = \frac{e^{-\gamma \sin^2\theta} - e^{-\gamma}}{1 - e^{-\gamma}}, \tag{2.61}$$

where

$$\gamma = 2\pi r_0 \frac{\Delta m^2}{2E_\nu} = 1.22 \left(\frac{\Delta m^2}{10^{-9}\text{ eV}^2}\right)\left(\frac{0.862\text{ MeV}}{E_\nu}\right), \tag{2.62}$$

for $r_0 = R_\odot/10.54 = 6.60 \times 10^4$ km [17].

Eqs. (2.62) and (2.61) show that in the limit $\sin^2\theta\Delta m^2 \gg (10^{-9}\text{ eV}^2)(E_\nu/1\text{ MeV})$ the value of the level crossing probability P_c goes to zero. The evolution in this case

is said to be *adiabatic*. Adiabatic evolution inside the Sun can lead under certain conditions to an almost total conversion of electron neutrinos into another flavor type, when the mixing angle in vacuum is very small. Indeed, suppose that $\Delta m^2 > 0$ and $\theta \ll 1$. Suppose that also $\sqrt{2}G_F N_e(0) > \Delta m^2/(2E_\nu)$ at the production point in the core. Then in the core the electron neutrino is produced almost completely in the *heavy* eigenstate. Assuming the evolution is adiabatic, the neutrino leaves the Sun also in the heavy state which, in vacuum, consists almost entirely of ν_μ. This is the essence of the MSW mechanism. The possibility of nearly total conversion was missed in [11] and was pointed out in [15] and [16].

The vacuum oscillation solution is based on a simpler idea. One assumes that the solar neutrino oscillation length is of the same order of magnitude as the Earth–Sun distance. This allows one to achieve the necessary selective suppression of certain neutrino energy components (see Eq. (2.29)). While it is not clear what the parameters in the neutrino mass matrix have to do with the value of one astronomical unit, one cannot discard such coincidence as a logical possibility.

Using these results, one can determine the regions in the two-neutrino parameter space, which are allowed by the data from all the experiments listed in Table 2.3. The results of such fits traditionally have been shown in the $(\sin^2 2\theta, \Delta m^2)$ space. Analysis shows that there are four disconnected regions in the parameter space that fit the data. One of them, the "just-so" solution, relies on vacuum neutrino oscillations with a very long wavelength (comparable to the Earth-Sun distance) [2], while the

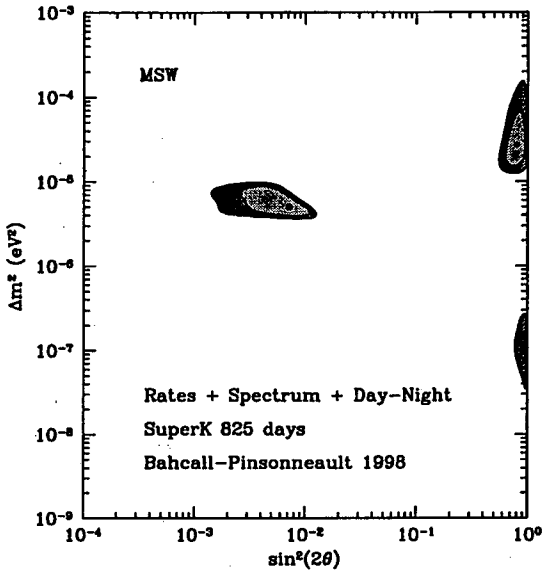

Figure 2.5: The global solutions for the allowed MSW oscillation regions, known, respectively, as the SMA, LMA, and LOW solutions (adopted from [1]).

other three (SMA, LMA, and LOW) [2, 3] rely on the MSW effect to produce the required energy dependence of the electron neutrino survival probability. The LOW solution also relies on the neutrino regeneration in the Earth during nighttime.

Figs. 2.5 and 2.6 show the recent fit results. Fig. 2.5 covers the MSW region, while Fig. 2.6 shows the allowed vacuum oscillation regions. Both figures have been adopted from [1]. We present the results of our own fits in Chapter 5.

2.3.4 Need for "Smoking Gun" Evidence for Oscillations

The results presented in the last section constitute a strong hint for neutrino flavor oscillations as a way to explain the observed neutrino fluxes. Nevertheless, this

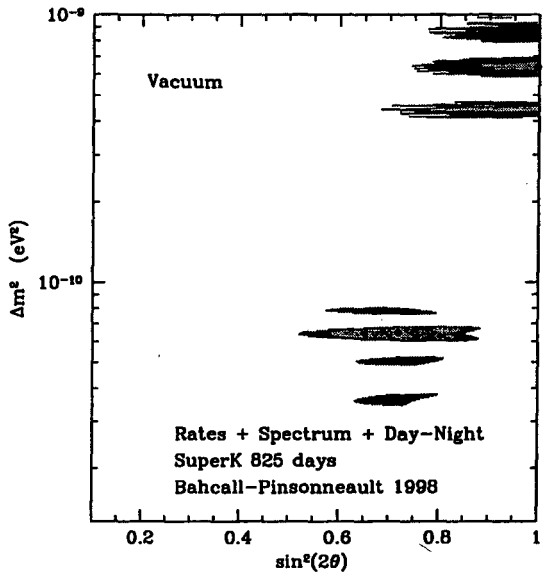

Figure 2.6: The global solution for the allowed vacuum oscillation regions (adopted from [1]).

evidence is as yet not considered definitive. As Sect. 2.3.2 shows, the solar neutrino experiments are notoriously difficult. Homestake data relies on being able to extract 15 atoms out of 100,000 tons of cleaning fluid with at least 90% efficiency, in the experiment located more than 1 km underground. Additionally, there is a possibility that the physics of the Sun is more complex than presently thought, and the neutrino flux calculations in the Standard Solar Model (SSM) may have underestimated the theoretical uncertainties. Even though it seems very unlikely that reasonable modifications to the SSM alone can explain the current solar neutrino data (see, for example, [31]), one still cannot completely discount the possibility that a combination of unknown systematic errors in some of the experiments and certain modifications

to the SSM could conspire to yield the observed data.

To conclusively demonstrate that the observed solar neutrino deficit is indeed due to neutrino flavor oscillations, it would be very desirable to detect at least one of the so-called "smoking gun" signatures of neutrino oscillations. Such signatures include a proof of the energy spectrum distortions, an anomalous seasonal variation in the observed neutrino flux, or a day-night variation due to the regeneration of electron neutrinos in the Earth. In the next chapter we study what can be accomplished at two upcoming neutrino experiments, Borexino and KamLAND, by analyzing the pattern of seasonal variations. In Chapter 4 we investigate the sensitivity of these experiments to the Earth regeneration phenomenon.

Out of all solar neutrino components, both experiments will be most sensitive to ^{7}Be neutrinos. As mentioned already, these neutrinos are almost monochromatic, with $E_\nu = 0.862$ MeV (90% of the time) or $E_\nu = 0.383$ MeV (10% of the time), depending on the final state of the ^{7}Li nucleus. Since the $E_\nu = 0.383$ MeV neutrinos cannot be cleanly seen at Borexino or KamLAND, in our analysis we will only consider the $E_\nu = 0.862$ MeV neutrinos, which will be referred to as the ^{7}Be neutrinos from now on.

The study of the ^{7}Be neutrino flux is particularly important, for a variety of reasons. First, in the SSM independent analysis of the solar neutrino data [31], where one arbitrarily rescales the flux of neutrinos from different sources, the flux of ^{7}Be neutrinos comes out extremely suppressed (in fact the best fit value for the ^{7}Be flux

is negative!), and the measurement of a reasonable flux would dramatically constrain such attempts. Second, since the prediction of one particular MSW solution (the small angle solution) for the survival probability of ^{7}Be neutrinos is very different from the other two solutions, one can separate it from the other two by measuring the ^{7}Be solar neutrino flux. Finally, as we show in the next chapter, one can either establish or exclude the "just-so" solution by analyzing the seasonal variation of the ^{7}Be solar neutrino flux at Borexino or KamLAND.

Chapter 3

Seasonal Variations at Borexino and KamLAND

In this chapter we present a quantitative study of what can be accomplished by measuring the seasonal variations of the ^{7}Be neutrino flux at Borexino and KamLAND. Seasonal variations of the solar neutrino flux are of course expected, because of the eccentricity of the Earth's orbit. The number of neutrinos of all flavors reaching the Earth is larger when the Earth is closer to the Sun than when it is farther away, and should vary as $1/L^2$. In the case of no neutrino oscillations or of the MSW solution to the solar neutrino problem, the number of ^{7}Be solar neutrino induced events is supposed to vary according to the $1/L^2$ law, following the variation of the total neutrino flux. This will be referred to as the "normal" seasonal variation.

If vacuum oscillations are the solution to the solar neutrino puzzle, large, anoma-

lous seasonal variations of the number of ^{7}Be solar neutrino induced events might be detected [32, 33]. As Eq. (2.29) shows, neutrino oscillation effects depend on the distance to the neutrino source, and different Earth-Sun distances may yield very different ν_e survival probabilities [26, 34]. The anomalous seasonal variation effect should be more pronounced in ^{7}Be neutrinos than in ^{8}B neutrinos (the latter was recently studied in [35]). This is because, as discussed in Section 2.3.1, ^{7}Be neutrinos are produced as part of a two-body final state and hence are virtually monoenergetic[1]. The details will become clear when we discuss the anomalous seasonal variation effect in Section 3.2.

In the case of no anomalous seasonal variations, if one has enough statistics and a small enough background, the time variation of the data can be used to measure the solar neutrino flux, given that the number of background events is constant in time.[2] We will analyze how well Borexino and KamLAND can perform this type of measurement. We are particularly interested in analyzing the relevance of this technique when the number of electron neutrinos reaching the detector is very suppressed with respect to the Standard Solar Model predictions, as might be the case if there are $\nu_e \rightarrow \nu_{\mu,\tau}$ oscillations for the small angle MSW solution.[3]

[1] In fact there are two distinct neutrino energies, 0.383 and 0.862 MeV, corresponding to different final states of the ^{7}Li nucleus. Borexino and KamLAND are only sensitive to the higher energy component.

[2] Actually, a time-dependent background is also acceptable, as long as it can be monitored and understood well enough.

[3] If ν_e oscillates into sterile neutrinos, the suppression is even more pronounced, due to the absence of neutral current $\nu_{\mu,\tau}$-e elastic scattering. We do not consider oscillations into sterile neutrinos in our analysis.

Our presentation in this chapter is organized as follows. In Sect. 3.1 we discuss how seasonal variations might be used to determine the solar neutrino flux at Borexino and KamLAND, in such a way that no separate measurement of the number of background events is required. In Sect. 3.2 we analyze the effect of the vacuum oscillation solutions to the solar neutrino puzzle on the annual variation of the number of detected events at Borexino and KamLAND. In particular we describe the region of the $(\sin^2 2\theta, \Delta m^2)$ parameter space where vacuum oscillations can be discovered by studying the seasonal variations of the data. In Sections. 3.3 and 3.4 we describe how the measurement of the seasonal variation of the ^{7}Be solar neutrino flux may be used to either measure the neutrino oscillation parameters, $\sin^2 2\theta$ and Δm^2, or exclude a large portion of the $(\sin^2 2\theta, \Delta m^2)$ parameter space. Section 3.5 contains a summary of our results and conclusions.

3.1 Measuring the ^{7}Be Solar Neutrino Flux

As was already pointed out, measuring the flux of ^{7}Be neutrinos is crucial towards understanding the solar neutrino puzzle. Borexino [36] plans to do this measurement by using 300 tons of organic liquid scintillator to detect recoil electrons from elastic ν-e scattering. Since the scintillator has no directional information, and the signal is characterized only by the scintillation light produced by the recoil electron, the background has to be kept under control. This places a very stringent constraint on the radio-purity of the scintillator and on the activity of the material in the detector.

Borexino anticipates 100 tons of fiducial volume for detecting solar neutrinos.

KamLAND [37], which was originally conceived as a reactor neutrino experiment with an unprecedented baseline (170 km on the average), may also be able to study ^{7}Be solar neutrinos, if rigorous yet attainable requirements on the radio-purity and activity are met. We assume throughout this dissertation that KamLAND will use 600 tons of fiducial volume for detecting solar neutrinos (the size of the fiducial volume will depend on the background rate, which is currently unknown). We concentrate our analysis on Borexino, which is an approved dedicated solar neutrino experiment, and discuss KamLAND, whose uses for solar neutrino studies are at present being proposed [38], as a possible higher statistics improvement.

It is important to define what is meant by "measuring the ^{7}Be solar neutrino flux." In reality, what the experiments are capable of measuring is the number of recoil electrons induced by solar neutrino interactions in a given recoil electron kinetic energy range (kinematic range). This information can only be converted into a solar neutrino flux measurement if one knows the flavor composition of the solar neutrinos. Explicitly, assuming that the solar neutrino flux is composed of ν_e (with fraction P) and $\nu_{\mu,\tau}$ (with fraction $Q = 1 - P$),

$$\#\text{recoil electrons/time} = \Phi \times (P\sigma_{\nu_e\text{-}e} + (1-P)\sigma_{\nu_{\mu,\tau}\text{-}e})N_e, \tag{3.1}$$

where Φ is the neutrino flux, N_e is the number of target electrons, and

$$\sigma_{\nu_x\text{-}e} \equiv \int_{T_{\min}}^{T_{\max}} dT \left(\frac{\mathrm{d}\sigma}{\mathrm{d}T}\right)_{\nu_x\text{-}e}, \tag{3.2}$$

with $\left(\frac{d\sigma}{dT}\right)_{\nu_x\text{-}e}$ being the differential cross section for ν_x-e scattering for a given kinetic energy T of the recoil electron. $T_{\rm min}$ and $T_{\rm max}$ define the kinematic range. In the case of neutrino oscillations, P is the the survival probability for electron neutrinos, while $1-P$ is the probability that ν_e will oscillate into $\nu_{\mu,\tau}$.

If the flavor composition of the flux is not known, all that can be quoted is the effective neutrino flux, $\Phi_{\rm eff}$, which is calculated from the number of measured recoil electrons assuming that there are only electron neutrinos coming from the Sun. Explicitly,

$$\Phi_{\rm eff} \equiv \frac{\#\text{recoil electrons/time}}{\sigma_{\nu_e\text{-}e} N_e} = \Phi \times \left(P + (1-P)\,\frac{\sigma_{\nu_{\mu,\tau}\text{-}e}}{\sigma_{\nu_e\text{-}e}} \right). \tag{3.3}$$

Clearly, if $P = 1$, $\Phi_{\rm eff} = \Phi$. It is important to remember that $\sigma_{\nu_{\mu,\tau}\text{-}e}/\sigma_{\nu_e\text{-}e} < 1$ and therefore $\Phi_{\rm eff} \leq \Phi$. The ratio of the neutrino elastic cross sections depends on the energy of the incoming neutrino and the kinematic range to which each particular experiment is sensitive. For $E_\nu = 0.862$ MeV and the Borexino (KamLAND) kinematic range 250–800 keV (280–800 keV), $\sigma_{\nu_{\mu,\tau}\text{-}e}/\sigma_{\nu_e\text{-}e} = 0.213(0.214)$. It is this effective electron neutrino flux, $\Phi_{\rm eff}$, that is referred to, throughout this dissertation (and in general), as the ^{7}Be solar neutrino flux.

In order to determine the number of recoil electrons induced by solar neutrino interactions, it is crucial to determine the number of background events. The number of background events can be estimated by various techniques, which we do not address in this dissertation. It is worthwhile to point out, however, that this is a very difficult process and it would be highly desirable to have an independent way to determine the

^{7}Be solar neutrino flux in order to make the final results more convincing. This may be possible if one looks at the seasonal variation of the number of detected events.

In the following, we study the seasonal variation of the event rate as a means to measure the ^{7}Be solar neutrino flux. The distance between the Earth and the Sun varies slightly over seasons because of the eccentricity of the Earth's orbit. The perihelion (when the Earth is closest to the Sun) occurs around January first. The eccentricity of the Earth's orbit is $\epsilon = 0.017$, and hence the distance varies as

$$L = L_0(1 - \epsilon \cos(2\pi t/\text{year})), \tag{3.4}$$

to the first order in ϵ. Here, t is the time measured in years from the perihelion, and $L_0 = 1.496 \times 10^8$ km is one astronomical unit. The neutrino flux varies as $1/L^2$ and hence shows a seasonal variation of about 7% from minimum to maximum. The change in the Earth-Sun distance between the aphelion and the perihelion is given by

$$\Delta L \equiv L_{\text{max}} - L_{\text{min}} = 2\epsilon L_0 = 5.1 \times 10^6 \text{ km}. \tag{3.5}$$

By fitting the event rate to the seasonal variation expected due to the eccentricity,

$$B + S\left(\frac{L_0}{L}\right)^2, \tag{3.6}$$

one can extract the background event rate B and the signal event rate S independently. As long as the detector is monitored well and its performance is sufficiently stable, this method will be only limited by statistics.

Borexino expects 53 events/day [4] according to the BP95 [39] Standard Solar Model

[4]For simplicity, we neglect the contribution of solar neutrino sources other than ^{7}Be electron

(SSM), together with 19 background events/day [36], after the statistical subtraction of the known background sources. This is done by pulse shape discrimination against the α-particle background and the measurement of Bi-Po pairs via α-β coincidence. This in turn allows the statistical subtraction of processes in the ^{238}U and ^{232}Th chains which are in equilibrium. It is also assumed that the experiment can achieve a radiopurity of 10^{-16}g/g for U/Th, 10^{-18}g/g for ^{40}K, ^{14}C/^{12}C $= 10^{-18}$, and no Rn diffusion. For KamLAND we use 466 events/kt/day for the signal and 217 events/kt/day [38] for the background under similar assumptions but with larger cosmogenic background (especially ^{11}C) and some Rn diffusion. Assuming 600 t of fiducial volume, we expect 280 signal events/day and 130 background events/day. Throughout the chapter, we will assume that the number of background events is either constant in time or its time dependence is sufficiently well understood by monitoring. We neglect systematic effects and assume that there are only statistical uncertainties.

Under these assumptions, Fig. 3.1 depicts a simulation of the seasonal variation of the "data" for both Borexino and KamLAND, after three years of running. The plots are for the case of the small angle MSW solution to the solar neutrino puzzle, where the ν_e's produced by ^{7}Be electron capture inside the Sun have almost completely oscillated into ν_μ or ν_τ, and the event rate is reduced to 21.3% (21.4%) of the SSM prediction at Borexino (KamLAND). In the fit to the data, both the background and the ^{7}Be flux are allowed to float.

capture throughout this chapter. In particular we neglect the contribution of neutrinos produced in the CNO cycle, which is about 10% of that from the ^{7}Be neutrinos.

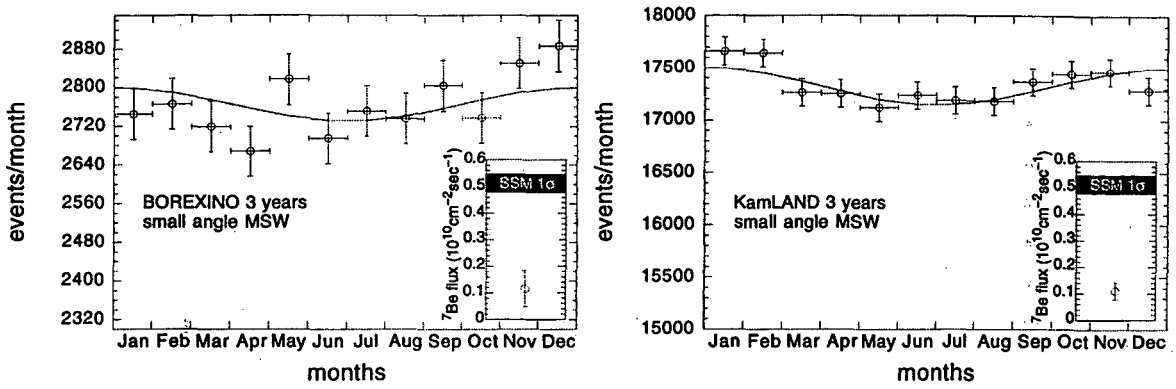

Figure 3.1: The simulated seasonal variation of the ^{7}Be flux for the case of the small angle MSW solution, for three years of Borexino (left) and KamLAND (right) running. The inset shows the measured flux of ^{7}Be neutrinos from the fit to the seasonal variation of the event rate (point with error bar) and the SSM prediction (shaded band).

This analysis can be repeated for different values of the ^{7}Be flux, or, equivalently, for different survival probabilities for ν_e. Fig. 3.2 depicts the expected 1 σ statistical accuracy of the ^{7}Be flux measurement, together with the central value normalized by the SSM prediction, as a function of the survival probability for ν_e. We emphasize that this measurement technique assumes no knowledge of the background.

The important information one should obtain from this analysis is if one can indeed measure a nonzero ^{7}Be solar neutrino flux. For example, in the case of the small angle MSW solution, the ν_e survival probability is very close to zero and, assuming the expected number of background events, Borexino's measured neutrino flux is less than 1.5 σ away from zero. The situation at KamLAND is much better, and in the case of the small angle MSW solution a healthy 3 sigma-away-from-zero measurement of the flux is obtained, if the background is as low as expected. The

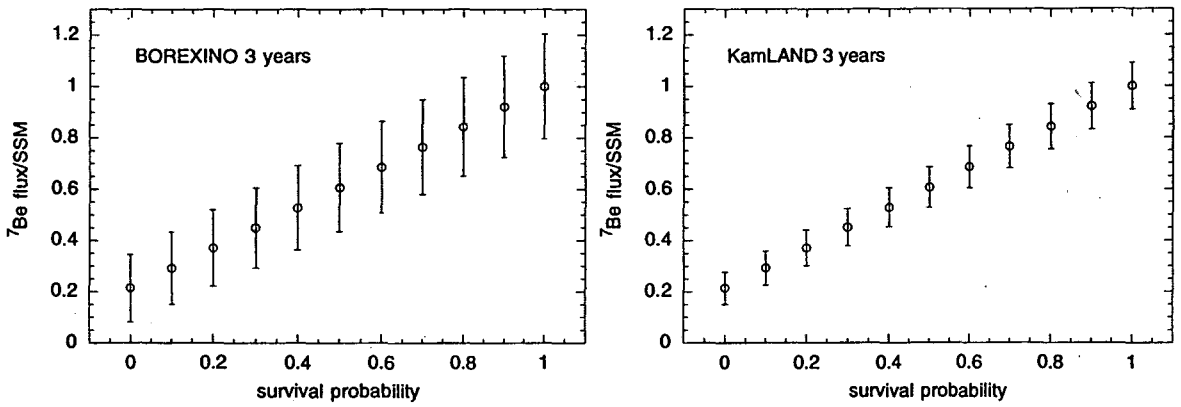

Figure 3.2: The expected 1 σ statistical accuracy of the ^{7}Be neutrino flux measurement, together with the central value normalized by the flux predicted by the SSM, as a function of the ν_e survival probability at Borexino (left) and KamLAND (right), after three years of data taking.

significance of the measured flux increases for larger survival probabilities, as in the case of the large angle and the low Δm^2 MSW solutions.

A similar analysis can be performed in order to determine how many background events each experiment can tolerate in order to claim a solar neutrino flux measurement which is 3 σ away from zero. Fig. 3.3 depicts the maximum number of background events per day allowed for 3 years of Borexino or KamLAND running. It is worthwhile to comment that, in the case of Borexino and the small angle MSW solution ($P \simeq 0$), a 3 sigma-away-from-zero measurement of the neutrino flux is not attainable in three years, even in the case of no background (note that for $P \lesssim 0.05$ the required maximum background to achieve a three σ measurement of the flux is negative, *i.e.*, impossible to achieve). Therefore, for Borexino, this simple, background independent analysis using the seasonal variation of the data is not particularly powerful in the case of the small angle MSW solution, due to statistical

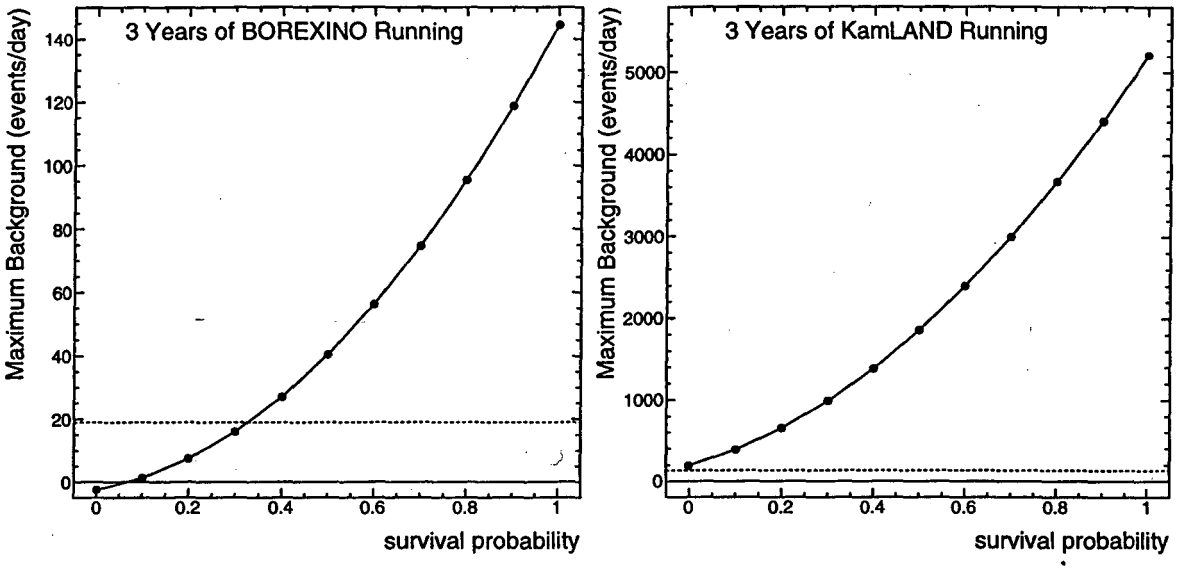

Figure 3.3: The maximum number of background events allowed per day at Borexino (left) or KamLAND (right), for 3 years of running, in order to measure a solar neutrino flux which is 3 σ away from zero. The dashed lines indicate the currently anticipated number of background events per day.

limitations.

3.2 Sensitivity to Vacuum Oscillations

In this section we study the discovery potential of the Borexino and KamLAND experiments in the region of Δm^2 corresponding to the vacuum oscillation solution to the solar neutrino problem. In this case, the pattern of seasonal variations can be very distinct from the normal pattern discussed in the previous section.

The basic idea is the following. The survival probability P for an electron neutrino

in the case of neutrino vacuum oscillations between two flavor states[5] is given by

$$P = 1 - \sin^2 2\theta \sin^2 \left(1.27\Delta m^2 \frac{L}{E}\right), \tag{3.7}$$

where the neutrino energy E is in GeV, the distance L in km, and the difference of masses-squared Δm^2 in eV^2. Model-independent analyses of all solar neutrino data show the need for an energy-dependent suppression of the ν_e flux. The "just-so" solution achieves this by choosing Δm^2 such that the corresponding neutrino oscillation length

$$L_{\text{osc}} \equiv \frac{\pi E}{1.27\Delta m^2} = 2.47 \times 10^8 \text{ km} \times \left(\frac{E}{10 \text{ MeV}}\right)\left(\frac{10^{-10} \text{ eV}^2}{\Delta m^2}\right) \tag{3.8}$$

is of the order of one Astronomical Unit (1 a.u. $= 1.496 \times 10^8$ km); hence the name "just-so". More specifically, the oscillation length is assumed comparable to 1 a.u. for ^{8}B neutrinos ($E_\nu \approx 10$ MeV); at the same time, the oscillation length of ^{7}Be neutrinos ($E_\nu = 0.862$ MeV) is an order of magnitude smaller and, for sufficiently large Δm^2, can be comparable to the seasonal variation of the Earth–Sun distance due to the eccentricity of the Earth's orbit, ΔL (see Eq. (3.5)). As a consequence, the flux of ^{7}Be neutrinos detected on the Earth may exhibit an anomalous seasonal variation, beyond the normal $1/L^2$ effect discussed in the previous section.

Such anomalous variation could serve as a unique signature of vacuum oscillations [32, 33]. Moreover, as we will show in this section, both Borexino and KamLAND will be able to cover a large portion of the "just-so" parameter space, even without relying

[5]One can assume the more complicated case of oscillations between three neutrino flavor states. In this chapter we limit our studies to the case of oscillations between two flavor states.

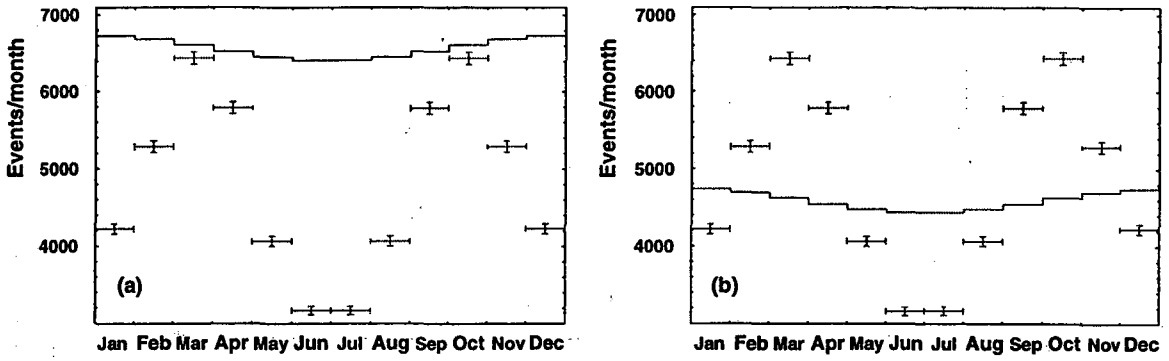

Figure 3.4: Illustration of the effect of vacuum oscillations on the shape of the seasonal variation of the solar neutrino data. The points with statistical error bars represent the number of events/month expected at Borexino after 3 years of running for $\Delta m^2 = 3 \times 10^{-10}$ eV^2, $\sin^2 2\theta = 1$. The histogram in (a) shows the number of events predicted by the SSM without neutrino oscillations, plus the number of anticipated background events. The histogram in (b) shows the same quantity after adjusting the solar neutrino flux and the background rate so as to minimize the value of χ^2, as explained in the text. The difference between the case with oscillations and the one without oscillations is still apparent.

on a particular solar model or estimate of the background rate, just by analyzing the *shape* of their data. In this sense the discovery of an anomalous seasonal variation at one of these experiments would be as robust a result as the Super-Kamiokande measurement of the up-down asymmetry for the atmospheric muon neutrinos.

To illustrate the main idea, we choose a particular point ($\Delta m^2 = 3 \times 10^{-10}$ eV^2, $\sin^2 2\theta = 1$) in the allowed region of the "just-so" parameter space [6] and compute the corresponding seasonal distribution of the neutrino events at Borexino after 3 years of running. We use the number of background events and the expected number of signal events (before the effect of neutrino oscillations) quoted in Sect. 3.1. The results are shown in Fig. 3.4 by the set of "data" points with error bars; each point

[6]Based on the analysis of the total rates in the Homestake, GALLEX, SAGE, and Super-Kamiokande experiments. See Fig. 5 in [2].

represents the number of events expected in a given month and the vertical error bars show the corresponding statistical uncertainties. The histogram in Fig. 3.4(a) shows "theoretical" event rates expected for non-oscillating neutrinos, provided the background rate is known accurately and the SSM prediction for the neutrino flux is trusted. One can see that under these assumptions vacuum neutrino oscillations with $\Delta m^2 = 3 \times 10^{-10}$ eV^2, $\sin^2 2\theta = 1$ would be trivial to discover.

More importantly, the experiment would be able to claim the discovery even without relying on an estimate of the background rate or the value of incoming neutrino flux predicted by the SSM. It is intuitively obvious from the figure that the vacuum oscillation "data" points cannot be fit by the "theoretical" curve even if the background and the solar neutrino flux are varied freely, unless one assumes neutrino oscillations. This can be quantified as follows. For a given background rate b and signal event rate s, we define the χ^2 value of the fit for an "average" experiment:

$$\chi^2(s,b) = N_{\text{d.o.f.}} + \sum_{i}^{N_{\text{bins}}} \frac{(d_i - b - s \cdot h_i)^2}{d_i}, \tag{3.9}$$

where N_{bins} is the number of bins, $N_{\text{d.o.f.}}$ is the number of degrees of freedom, d_i is the *average* expected number of neutrino events in the ith bin, and h_i is given by $h_i = \int_{i-1}^{i}(1 - \epsilon\cos(2\pi x/N_{\text{bins}}))^2 dx$. The constant term $N_{\text{d.o.f.}}$ in Eq. (3.9) is added to take into account the effect of statistical fluctuations in the data. In a single experiment, statistical fluctuations make the number of neutrino events in the ith bin slightly different from d_i, and χ^2 is computed by an expression similar to Eq. (3.9), with d_i replaced by the number of events measured in the ith bin and

without the constant term, $N_{\text{d.o.f.}}$. In our analysis, however, we are interested in the sensitivity of an "average" experiment. As proven in Appendix B.1, averaging over many experiments results in the definition of χ^2 given in Eq. (3.9), with the constant term $N_{\text{d.o.f.}}$. This agrees with the conventional wisdom that, if a function describes data correctly, the average expected value of χ^2 should be equal to the number of degrees of freedom. Given this definition, we can choose values of s and b that minimize the χ^2; the only restriction imposed is that both s and b be non-negative. For the case at hand the minimum occurs when b is zero and s is 0.95 times the SSM prediction (see Fig. 3.4(b)). As expected, even after this change the "data" points and the histogram are very different. (Numerically, $\chi^2 = 2935$ which for 10 degrees of freedom implies a confidence level of $1 - 9 \times 10^{-626}$!).[7]

We now extend this approach, and scan the entire ($\sin^2 2\theta$, Δm^2) plane (for an earlier work with a more simplified analysis which does not consider the presence of background, see [26]). In the analysis below, we follow the same steps as before: the "data" is simulated according to the expected number of background and signal events, plus the effect of neutrino oscillations, for each value of ($\sin^2 2\theta$, Δm^2), binned into a certain number of bins N_{bins}, and then compared to the "theoretical" predictions for the case of no oscillations. The χ^2 is computed according to Eq. (3.9) and minimized with respect to both the signal (s) and background (b). The confidence level (CL) corresponding to the minimal value of χ^2 and $N_{\text{d.o.f.}} = N_{\text{bins}} - 2$ degrees

[7] This number is, of course, unrealistic, and the true confidence level in this case will be dominated by systematic effects.

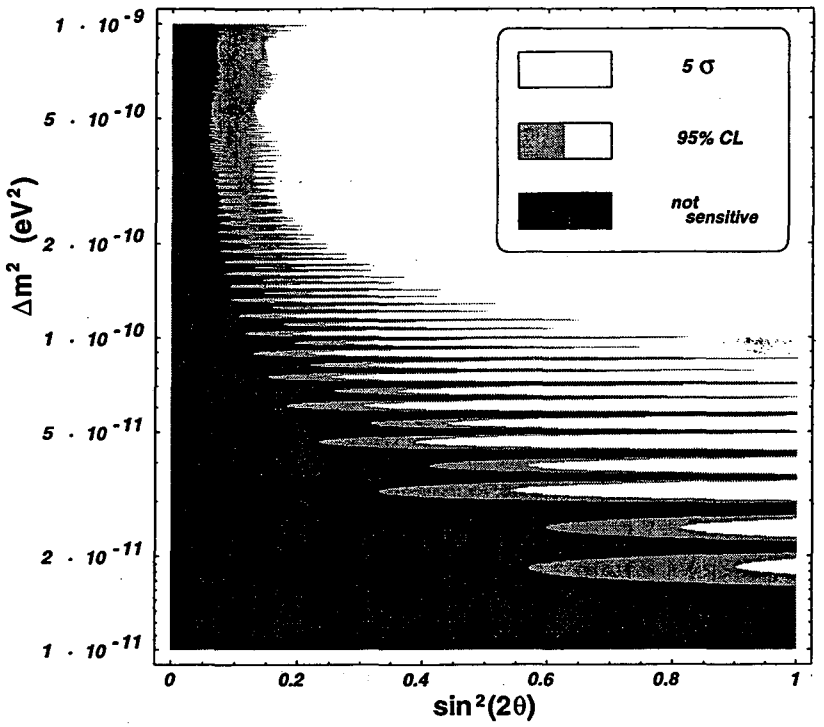

Figure 3.5: The sensitivity region of the Borexino experiment in 3 years, if the analysis does not assume any knowledge of the background rate or the incoming solar neutrino flux. In the unshaded region the "data" is at least 5 σ away from the best no-oscillations fit. In the lightly shaded region the discrepancy is greater than 95% CL but less than 5 σ CL.

of freedom is then determined, and the region in which the CL is less than a given number is isolated. This case, when both the number of background events and the incoming solar neutrino flux are considered unknown in the fit, is the most conservative one, and yields the smallest sensitivity region. Later we also study less conservative cases, where we assume in the "data" analysis that the incoming neutrino flux is the one predicted by the SSM and/or that the background rate is known.

We now apply this most conservative procedure to study the experimental reach of Borexino after 3 years of operation. In Figure 3.5 we show the results of the scan for

95% and 5 σ CL. As one can see from the figure, even at 5 σ CL a large portion of the parameter space above $\Delta m^2 \sim 10^{-10}$ eV^2 is covered (white region). In this region the neutrino oscillation length $L_{\rm osc}$ is smaller than the seasonal variation of the Earth–Sun distance ΔL. On the other hand, below $\Delta m^2 \sim 10^{-10}$ eV^2 one can see a series of spikes protruding through the sensitivity region. It is important to understand the origin of these spikes. Since we adjust the level of signal and background in the fit, we are not sensitive to the absolute event rate, only to its variation during the year. For $\Delta m^2 \lesssim 10^{-10}$ eV^2 the oscillation length is larger than ΔL and the amplitude of the variation of the event rate is roughly proportional to the first derivative of Eq. (3.7) with respect to L. In the regions where this derivative nearly vanishes, the amplitude of the variations is small and the signal is indistinguishable from the case of no oscillations. This explains why the loss of sensitivity occurs not only when the neutrinos undergo approximately an integer number of oscillations as they travel to the Earth ($\Delta m^2 = n \times 0.143 \times 10^{-10}$ eV^2), but also when the number of oscillations is close to a *half-integer* ($\Delta m^2 = (n + 1/2) \times 0.143 \times 10^{-10}$ eV^2). In the latter case the absolute neutrino flux is maximally suppressed, but the magnitude of the seasonal variation is small.[8]

Given this explanation, one would expect that the spikes corresponding to a half-integer number of oscillations should become shorter if in the analysis we choose to rely on the SSM prediction of the incoming neutrino flux and/or on the anticipated

[8]Notice that the regions preferred from the global fits have the absolute ^{7}Be neutrino flux suppressed. See Figs. 3.9 and 3.10.

background rate. It is straightforward to incorporate the knowledge of both quantities and their uncertainties in our procedure. For example, to impose the value of the incoming neutrino flux predicted by the SSM, we modify the expression of χ^2 in Eq. (3.9) by adding an extra term:

$$\chi^2(s,b) \longrightarrow \chi^2(s,b) + \frac{(s-s_0)^2}{\sigma_{s_0}^2}, \tag{3.10}$$

where s and b are the values of the signal and background with respect to which we later minimize χ^2, s_0 is the SSM prediction for the signal, and σ_{s_0} is the uncertainty in s_0. The rest of the analysis is carried out unchanged, except that the number of degrees of freedom is increased by one to $N_{\text{d.o.f.}} = N_{\text{bins}} - 1$. To use both the incoming flux predicted by the SSM and the anticipated background rate, two terms are added to Eq. (3.9) and the number of degrees of freedom is increased by two to $N_{\text{d.o.f.}} = N_{\text{bins}}$.

The results of the calculation are shown in Fig. 3.6. The uncertainty on the solar model prediction of the ^{7}Be neutrino flux is taken to be 9% [4], while the uncertainty on the background is 10% [38]. As expected, the odd–numbered spikes do become shorter. The one possibility not shown in the plot is the situation when one only assumes knowledge of the background rate. In this case the spikes become significantly thinner, although their length remains virtually unchanged.

In order to extend this analysis to values of $\Delta m^2 > 10^{-9}$ eV^2, several issues must be confronted. We will next address these issues one by one, and illustrate the discussion in Fig. 3.7.

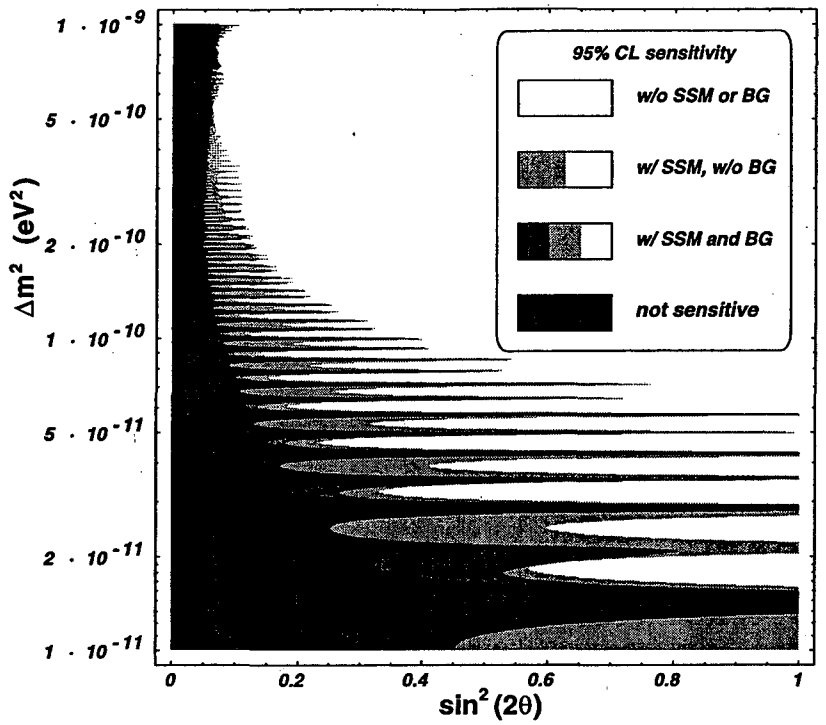

Figure 3.6: The sensitivity reach of the Borexino experiment after 3 years of running (at 95% confidence level). The three cases considered are: no knowledge of either the background rate or the incoming solar neutrino flux (the covered region is white); assumption that the incoming solar neutrino flux is the one predicted by the SSM, with 9% uncertainty (the covered region is white + light gray); assumption that the background rate is known with 10% uncertainty and the incoming neutrino flux agrees with the SSM, with 9% uncertainty (the covered region is white + light gray + medium gray).

The first and the most obvious point is that the number of bins needs to be changed. The reason is that the frequency of the seasonal variations increases with Δm^2, and above some value ($\Delta m^2 \simeq 8 \times 10^{-10}$ eV^2, for 12 bins) integration over the bin size washes out the effect. To avoid this, we change the number of bins from 12 to 365. After the change, the effect of binning kicks in at $\Delta m^2 \simeq 2.4 \times 10^{-8}$ eV^2, as curve 1 in Fig. 3.7 illustrates.

Next, there are two physical effects one must take into account: one is the in-

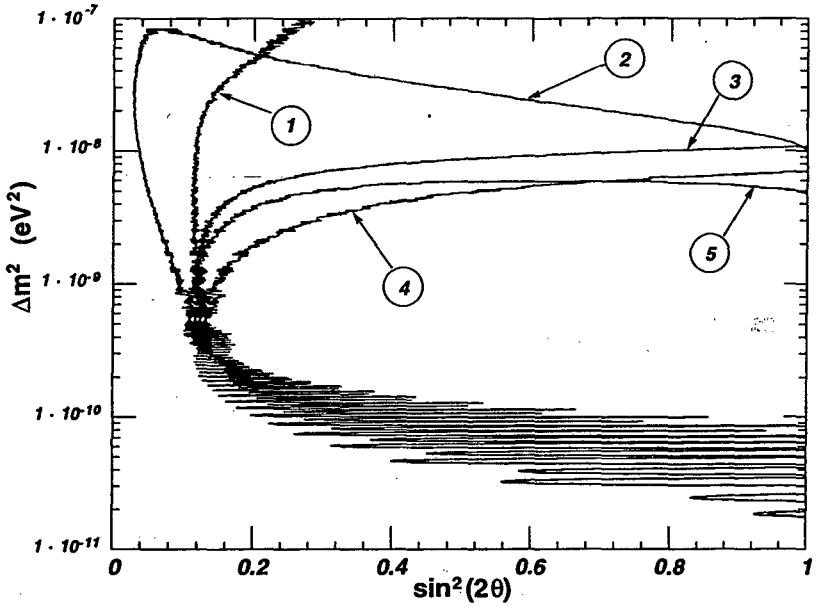

Figure 3.7: The relative roles of the binning effect, the linewidth effect, and the matter effect, as explained in the text.

teraction of the neutrinos with solar matter (the MSW effect), and the other is the finite width of the ^{7}Be solar neutrino line. One may worry about the wash-out of the seasonal variation effect due to the finite size of Sun's core. However, matter effects make the core size effect irrelevant because the mixing angle in the Sun's core is small and the oscillations effectively start at the level-crossing point (see Eq. (3.12)).[9]

When a ν_e is created by the electron capture process in the core of the Sun, its Hamiltonian is dominated by the matter effect $\sqrt{2}G_F n_e$ (n_e is the electron number density) if $\Delta m^2 \ll 10^{-5}$ eV^2 for ^{7}Be neutrinos. We restrict ourselves to $\Delta m^2 < 10^{-7}$ eV^2 in the following discussions, as the final sensitivity due to the anomalous seasonal variation is limited by $\lesssim 10^{-8}$ eV^2 as will be seen later in this section.

[9]We thank E. Lisi and L. Wolfenstein for pointing this out to us. For earlier papers on this particular point, see [11], [32], and in particular, [27].

Then the mass mixing effect can be completely ignored at the time of the neutrino production, and one can safely take the produced neutrino to be in a Hamiltonian eigenstate (the one which corresponds to the larger energy in the Sun's core). As it propagates through the Sun, the neutrino follows the instantaneous Hamiltonian eigenstate (in the adiabatic approximation), and exits in the heavier mass eigenstate, $\nu_2 = \nu_e \sin\theta + \nu_\mu \cos\theta$. It also has a finite amplitude A_c for hopping to the other Hamiltonian eigenstate. The neutrino state that exits the Sun can therefore be written as

$$\nu_{\text{exit}} = A_c \nu_1 + B_c \nu_2, \tag{3.11}$$

with the unitarity constraint $|A_c|^2 + |B_c|^2 = 1$. Out of the Sun, the two mass eigenstates develop different phases due to the mass difference, $e^{-i\Delta m^2 t/2E_\nu}$. Therefore the neutrino state that arrives at the Earth is given by

$$\nu_{\text{arrival}} = A_c \nu_1 + B_c \nu_2 e^{-i\Delta m^2 L/2E_\nu}, \tag{3.12}$$

up to an overall phase factor. The distance L is between the point of level crossing and the Earth. Finally, the survival probability of the electron neutrino is determined by the ν_e component of ν_{arrival}, and hence

$$\begin{aligned} P &= |A_c \cos\theta + B_c \sin\theta e^{-i\Delta m^2 L/2E_\nu}|^2 \\ &= |A_c|^2 \cos^2\theta + |B_c|^2 \sin^2\theta + 2\text{Re} A_c^* B_c e^{-i\Delta m^2 L/2E_\nu} \sin\theta\cos\theta. \end{aligned} \tag{3.13}$$

Since $|B_c|^2$ is the hopping probability between two Hamiltonian eigenstates in the Sun P_c, one can rewrite the formula using P_c and an additional phase factor $A_c^* B_c =$

$\sqrt{P_c(1-P_c)}e^{-i\delta}$,

$$P = P_c\cos^2\theta + (1-P_c)\sin^2\theta + 2\sqrt{P_c(1-P_c)}\sin\theta\cos\theta\cos\left(\frac{\Delta m^2 L}{2E_\nu} + \delta\right). \quad (3.14)$$

An approximate formula for P_c was given in [29, 30] using the exponential density profile of the Sun,

$$P_c = \frac{e^{-\gamma\sin^2\theta} - e^{-\gamma}}{1 - e^{-\gamma}} \quad (3.15)$$

with

$$\gamma = 2\pi r_0 \frac{\Delta m^2}{2E_\nu} = 1.22\left(\frac{\Delta m^2}{10^{-9}\mathrm{eV}^2}\right)\left(\frac{0.862\mathrm{MeV}}{E_\nu}\right), \quad (3.16)$$

where we consider the exponential-profile approximation for the electron number density in the Sun $n_e \propto \exp(-r/r_0)$, with $r_0 = R_\odot/10.54 = 6.60 \times 10^4$ km, given in [17]. Fig. 3.8 shows the contours of P_c on the $(\sin^2 2\theta, \Delta m^2)$ plane for the ^{7}Be neutrino energy $E_\nu = 0.862$ MeV.

The most important consequence of the matter effect is that the vacuum oscillation is suppressed when $P_c \to 0$ (adiabatic limit). The origin of the suppression is simple. When P_c is small, the neutrino state that exits the Sun is nearly a pure ν_2 state. Since it is a mass eigenstate, only its phase evolves in time and no oscillations take place. The ν_e survival probability then is simply given by the ν_e content of ν_2, which is nothing but $\sin^2\theta$, without anomalous seasonal variations. Therefore, the sensitivity to the anomalous seasonal variation is reduced in the region with small P_c. When Δm^2 is small, on the other hand, the situation is in the extreme non-adiabatic limit,

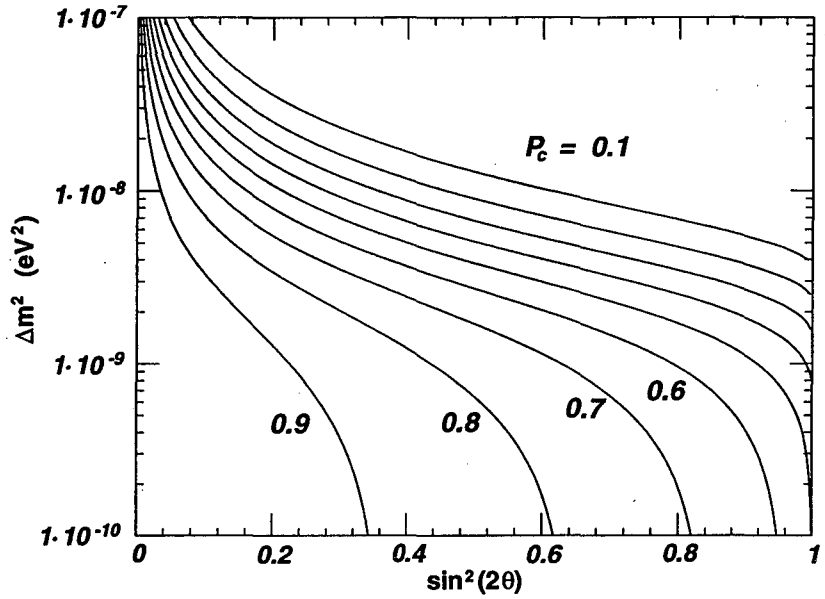

Figure 3.8: The contour plot of the hopping probability $P_c = 0.1, 0.2, \ldots, 0.9$, for the ^{7}Be neutrino energy, using the exponential-profile approximation for the electron number density and Eq. (3.15).

and $P_c \to \cos^2\theta$. Then Eq. (3.14) reduces to Eq. (3.7). As Δm^2 increases, P_c becomes smaller than $\cos^2\theta$, which enhances the vacuum oscillation effect in the small mixing angle region. Curve 2 in Fig. 3.7 includes the matter effect and indeed indicates a reduced sensitivity for large $\sin^2 2\theta$ (small P_c) and an enhanced sensitivity for small $\sin^2 2\theta$ (where P_c starts deviating from $\cos^2\theta$).[10]

The second effect is the finite width of the ^{7}Be line. To give some preliminary idea about the relative size of this effect, we first consider a simplified model. We assume for a moment that the only source of the line broadening is the Doppler shift of neutrino energies arising from the thermal motion of the ^{7}Be nuclei. Since the energy is shifted to $E \to E(1 + v_z/c)$ and the probability distribution of the velocity

[10]In the numerical scan, we ignored the additional phase factor δ, because its effects are negligible [27].

along the line of sight v_z is proportional to $\exp(-mv_z^2/2kT)$, the resulting line profile will be a Gaussian $\exp(-mc^2(E-E_0)^2/(2kTE_0^2))$. Taking the temperature to be 15.6 million Kelvin (the temperature in the center of the Sun) and integrating over the line profile, we obtain curve 3 in Fig. 3.7. The sensitivity loss now occurs at $\Delta m^2 \simeq 1 \times 10^{-8}$ eV^2, demonstrating that this effect is more important than the matter effect.

This naive model is actually incomplete; there exists another very important source of line broadening. Because the incoming electron in the process $^7\mathrm{Be} + e^- \rightarrow {}^7\mathrm{Li} + \nu_e$ has nonzero thermal kinetic energy, the center of mass energy of the reaction is greater than the one measured in the laboratory, and so the neutrino has a greater energy. The phase space distribution of electrons is governed by the Maxwellian factor $\exp(-E_e/kT)$. This distribution has to be multiplied by the energy-dependent cross section, integrated over the phase space, and finally convoluted with the Gaussian arising from the Doppler effect. The resulting line shape becomes asymmetric, with a Gaussian profile on the left (due to the Doppler effect) and an exponential tail on the right (due to the Maxwellian distribution of the electron energy). The issue was studied in detail in [40], where the precise form of the profile was computed.[11] Repeating the calculation with this profile we generate curve 4 in Fig. 3.7.

One can see that for this curve the cut-off occurs at smaller Δm^2. This behavior is expected, because the linewidth is now greater than when only the Doppler effect

[11] It turns out that other effects, such as collisional line broadening [41] or gravitational energy shift [40], are unimportant.

was included (curve 3 in Fig. 3.7). It is also worth noting that the cut-off sets in more gradually. This feature can be understood analytically by considering the Fourier transform of an exponential tail vs. a Gaussian tail. The details can be found in Appendix B.2.

Finally, we can combine both the linewidth and the matter effects. The result is curve 5 in Fig. 3.7. As expected, the inclusion of the matter effect on top of the linewidth effect introduces only a small distortion to the sensitivity region. It is important to note that for $\Delta m^2 \lesssim 5 \times 10^{-10}$ eV^2 none of the physical effects mentioned above affect the sensitivity region (curve 1 versus curve 5, in Fig. 3.7).

We need to consider one last ingredient in the analysis. We again return to the issue of the number of bins. While choosing more bins is necessary for larger values of Δm^2, it simultaneously leads to a loss of sensitivity for smaller Δm^2. A better procedure is to use an optimum number of bins N_{opt} for each Δm^2. It can be shown that for our method of analysis (minimizing χ^2 by varying the signal and background) and sufficiently large Δm^2 an approximate formula holds: $N_{opt} \simeq 2 \times 10^{10}(\Delta m^2/1 \text{ eV}^2)$. Of course, this formula should not be used when the optimal number of bins it predicts is too small. We choose to use 12 bins for $\Delta m^2 \leq 6 \times 10^{-10}$ eV^2 and a variable number of bins $N_{\text{bins}} = 2 \times 10^{10}(\Delta m^2/1 \text{ eV}^2)$ for $\Delta m^2 > 6 \times 10^{-10}$ eV^2.[12]

[12] An alternative technique, which can be considered more rigorous but which would also be more computer intensive, is to Fourier transform the simulated data for every value of $(\sin^2 2\theta, \Delta m^2)$ in the scan. One can then compare the intensities of the harmonics to those expected for the case of no oscillations. A description of this method can be found in [42]. For our purposes varying the number of bins is sufficient.

In Fig. 3.9 we show the entire sensitivity reach of Borexino after three years of running. The unshaded region will be covered at least at 95% CL, if in the analysis one allows the background and the incoming solar neutrino flux to float. The dark shading marks the additional portion of the parameter space that will be covered at least at 95% CL, if in the analysis one assumes both the anticipated background rate (10% uncertainty) and the SSM prediction of the ^{7}Be solar neutrino flux (9% uncertainty). For $\Delta m^2 \gtrsim 5 \times 10^{-9}$ eV^2, the sensitivity to the anomalous seasonal variation gets lost because of the smearing due to the linewidth effect. However, there is an overall suppression of the flux due to the MSW effect in this region. To be sensitive to this overall suppression, we should return to a smaller number of bins to enhance the statistical accuracy. We therefore use 12 bins in this region.[13]

For comparison, we also superimpose the "just-so" preferred regions obtained by analyzing the total event rates in the Homestake, GALLEX, SAGE, and Super-Kamiokande experiments (Fig. 5 in [2]). The plot shows that Borexino will be sensitive to almost all of the preferred region, even without relying on the SSM prediction of the incoming neutrino flux or on the knowledge of the background rate. Only two thin spikes protrude through the lower "islands". This overlap disappears completely when the anticipated background rate and the SSM prediction for the incoming neutrino flux are used in the "data" analysis, in which case the entire preferred region is covered.

[13] One can cover a slightly larger portion of the parameter space by using yet fewer bins. We chose 12 bins such that one can still verify the expected $1/L^2$ behavior of the signal even with a reduced flux, as we discussed in Sect. 3.1.

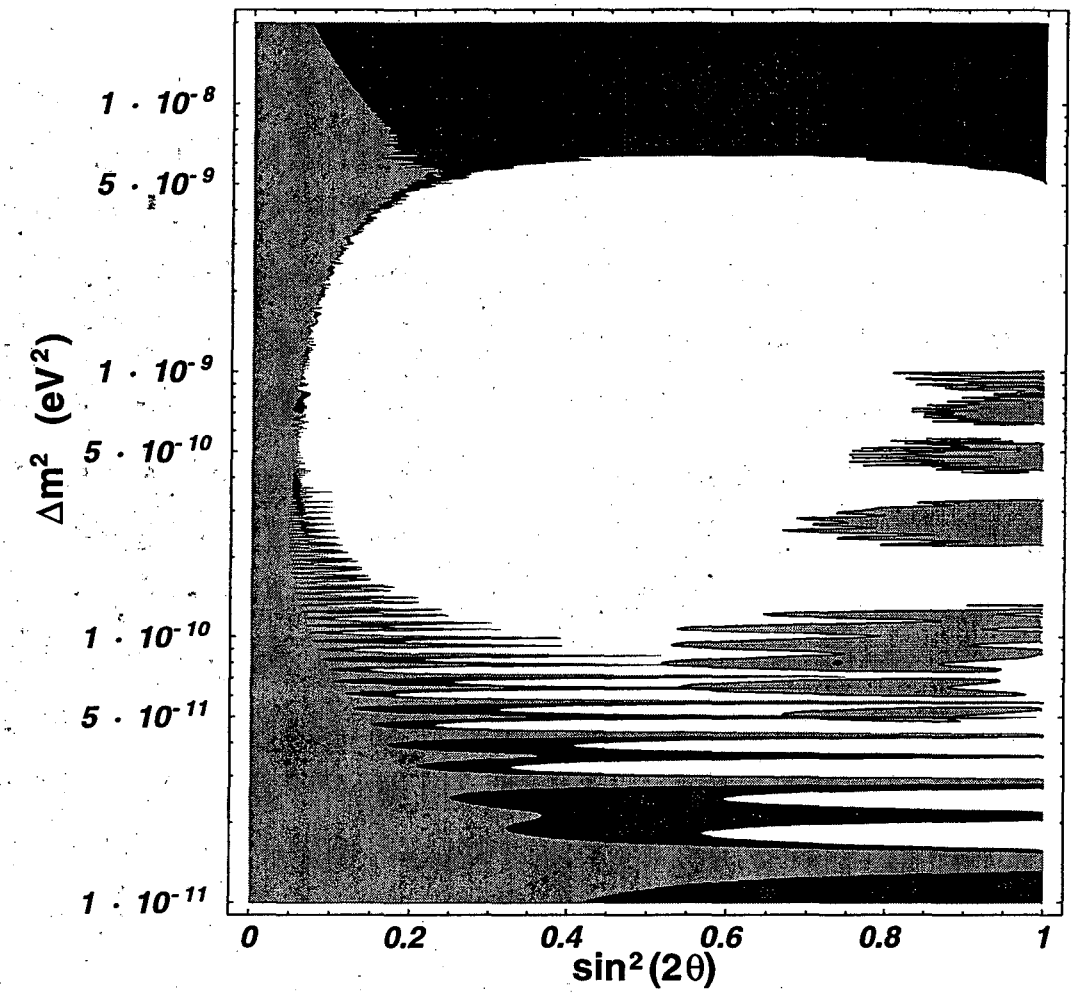

Figure 3.9: The final sensitivity plot for three years of Borexino running, after the inclusion of all effects limiting the reach of the experiment for large Δm^2. The white region corresponds to the sensitivity at more than 95% confidence level with both the incoming neutrino flux and background rate assumed to be unknown, and the dark region to the additional coverage when the SSM ^{7}Be flux and the background rate estimated elsewhere are used. Also shown are the regions preferred by the analysis of the total rates in the Homestake, GALLEX, SAGE, and Super-Kamiokande experiments [2].

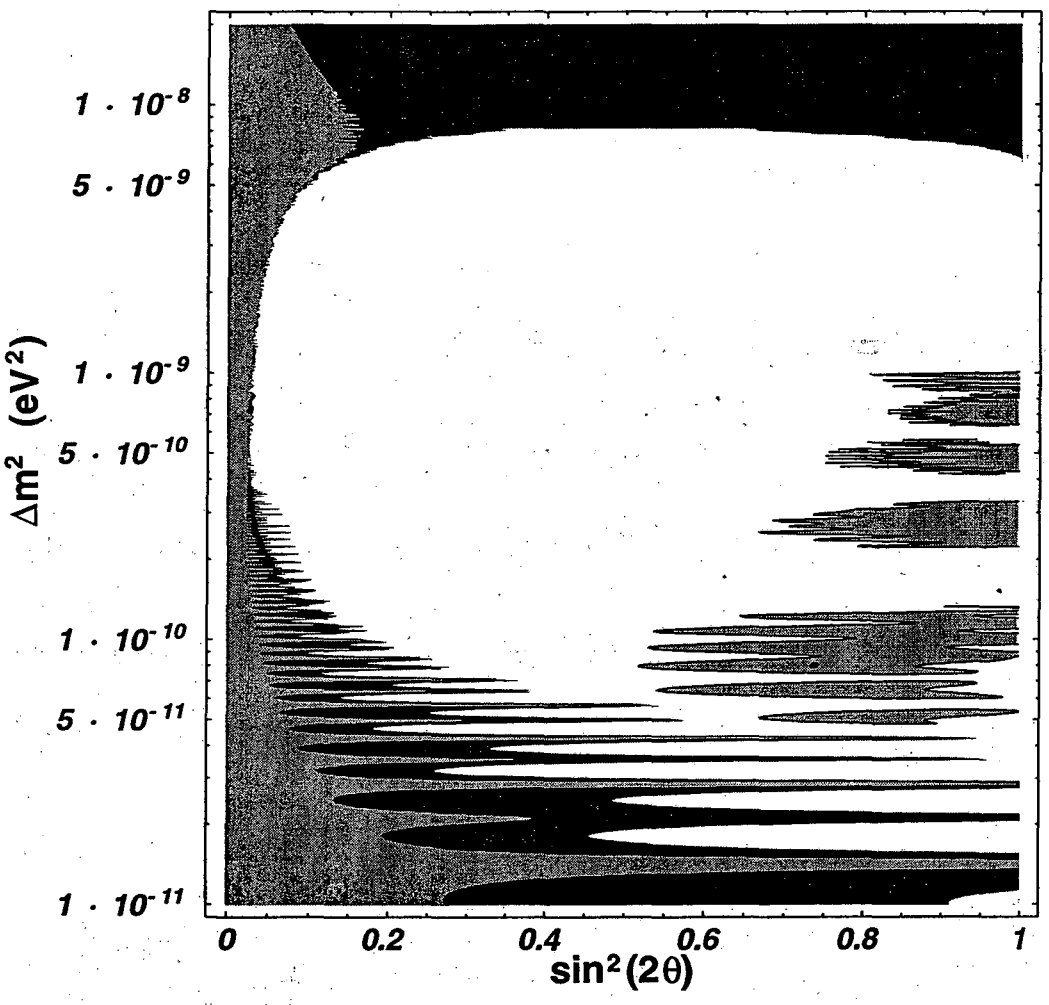

Figure 3.10: The same as Fig 3.9, but for three years of KamLAND running.

Fig. 3.10 contains a similar plot for three years of KamLAND running. Because KamLAND will have more statistics, it will be sensitive at 95% CL to the entire preferred region without relying in the analysis on the SSM prediction of the incoming neutrino flux or on the knowledge of the background rate.

As mentioned earlier, the sensitivity to anomalous seasonal variations is completely lost for $\Delta m^2 \gtrsim 10^{-8}$ eV^2. In this case the seasonal variation of the data is

consistent with an average suppression of the incoming neutrino flux. In particular, in the case of the MSW solutions (10^{-7} eV^2 $\lesssim \Delta m^2 \lesssim$ 10^{-4} eV^2), no anomalous seasonal variations can be detected, as was implicitly assumed in Sect. 3.1.

At last, it is worth mentioning that the experiments will still be sensitive to a significant part of the preferred region even if the background rate or the incoming ^{7}Be neutrino flux (for all flavors) turns out to be significantly different. For example, if the background rate at Borexino (KamLAND) turns out to be 30 (100) times higher than expected, the part of the preferred region with $\Delta m^2 > 10^{-10}$ eV^2 will still be within the reach of the experiment, after three years of running. The sensitivity will be completely lost only if the background rate turns out to be three (four) orders of magnitude higher than anticipated at Borexino (KamLAND). The consequences of a ^{7}Be solar neutrino flux smaller than predicted by the SSM can also be studied. If the ^{7}Be neutrino flux is for some reason suppressed by a factor of 5, KamLAND is still sensitive to the part of the preferred region with $\Delta m^2 > 10^{-10}$ eV^2, after 3 years of running.

3.3 Measuring the Oscillation Parameters

In this section, we address the issue of how well the two-neutrino oscillation parameters, $\sin^2 2\theta$ and Δm^2, can be extracted if the data collected at future solar neutrino experiments exhibits an anomalous seasonal variation. In order to do this, we simulate "data", according to the procedure developed in Sect. 3.2, for two distinct

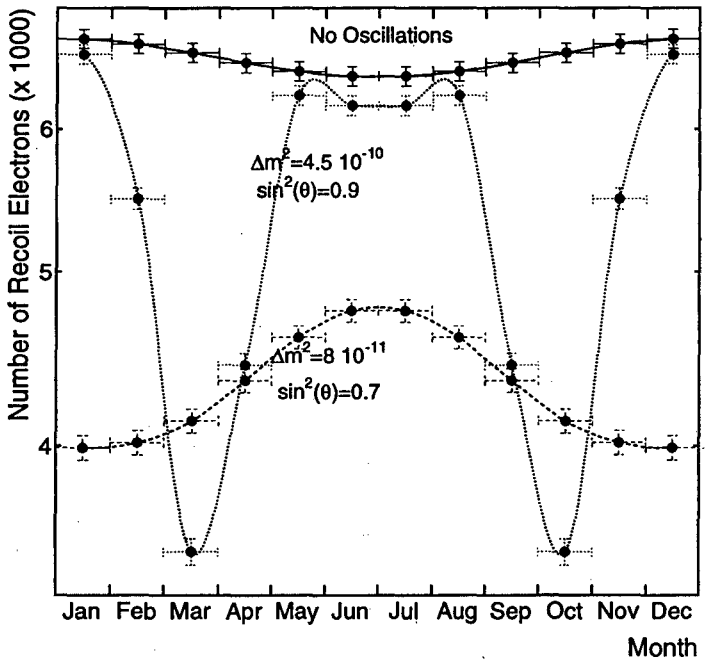

Figure 3.11: Number of recoil electrons detected in a given month, for the low point, the high point (see text for description) and the case of no neutrino oscillations, after three years of Borexino running.

points in the parameter space, $\sin^2 2\theta = 0.7$, $\Delta m^2 = 8 \times 10^{-11}$ eV^2 ("low point") and $\sin^2 2\theta = 0.9$, $\Delta m^2 = 4.5 \times 10^{-10}$ eV^2 ("high point"). The low point is close to the best fit point presented in [2], while the high point is close to the point preferred by the Super-Kamiokande analysis of the recoil electron energy spectrum [43]. The data is binned into months (12 bins per years), and Fig. 3.11 depicts the annual variations for both the high and the low points, assuming three years of Borexino running. The no-oscillation case is also shown.

In order to measure the oscillation parameters, we perform a 4 parameter (s, b, $\sin^2 2\theta$, and Δm^2) fit to the "data". The fit is performed by minimizing χ^2 with

respect to the incoming neutrino flux (s) and the background rate (b), as in Sect. 3.2, and computing it for fixed $\sin^2 2\theta$ and Δm^2. Fig. 3.12 depicts the values of $(\sin^2 2\theta, \Delta m^2)$ and the 95% CL contours (for two degrees of freedom), extracted from the "data" consistent with the low (light) and high (dark) points. Note that this is very different from what was done in the previous section. There, for each point in the $(\sin^2 2\theta, \Delta m^2)$ plane there was a different "data" set, and the "data" was fitted by a non-oscillation theoretical function. Here the "data" is fixed (either the low or the high point), and is fitted by a theoretical function which assumes neutrino oscillations.

One should easily note that the extracted 95% CL contour for the high point consists of only two "islands", while for the low point one extracts a collection of "islands". The reason for this is simple. When $\Delta m^2 \sim \text{few} \times 10^{-10}\ \text{eV}^2$, the oscillation length is slightly smaller than ΔL (see Eq. (3.5)). This means that the seasonal variation of the "data" has a very particular shape (as one may easily confirm by looking at Figs. 3.4, 3.11), which cannot be easily mimicked by other values of Δm^2, even when the background rate and the incoming flux are varied in the fit procedure.

When $\Delta m^2 \sim \text{several} \times 10^{-11}\ \text{eV}^2$, the oscillation length is larger than ΔL, and the effect of seasonal variations is less pronounced. There is a collection of Δm^2's that yields the same qualitative behavior. Because our fit procedure allows for the background rate and the neutrino flux to float freely, a good agreement with the "data" is met for a large portion of the parameter space. In order to make this

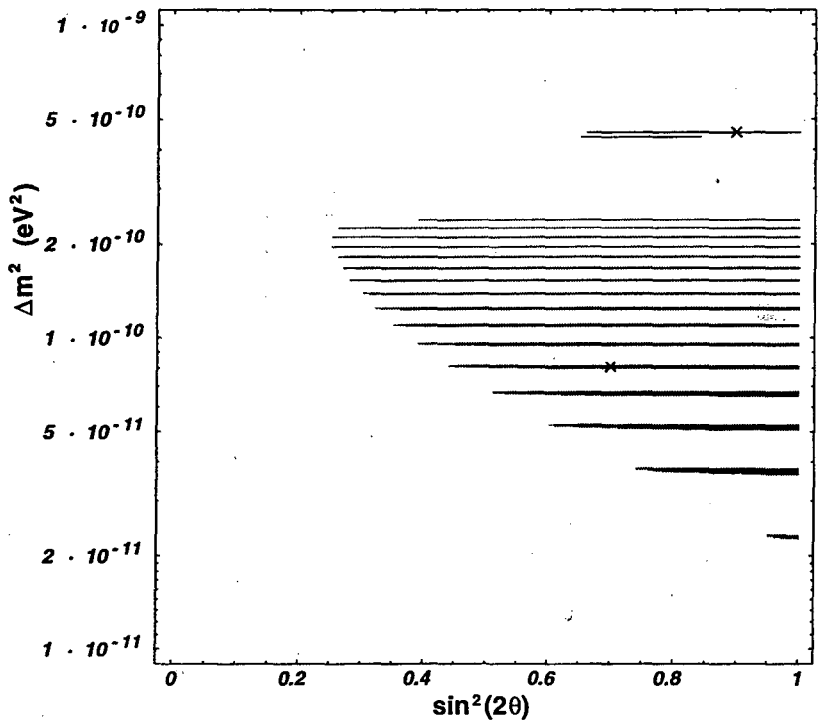

Figure 3.12: Measurement of the neutrino oscillations parameters $\sin^2 2\theta$ and Δm^2, assuming no knowledge of the SSM and the number of background events. The regions represent the 95% confidence level contours, for data consistent with the high (dark) and low points (light). The input points are indicated in the figure by the two crosses. See text for details. We assume 3 years of Borexino running.

discussion clearer, it is useful to describe in detail what happens to the number of electron neutrinos reaching the detector as a function of time.

In the case of the low point: initially, when the Earth is at the perihelion, the ν_e survival probability is small and, as time progresses, monotonically increases until the Earth reaches the aphelion (after six months). The process happens in reverse order in the next six months, as expected. There are many other values of the oscillation length, *i.e.* Δm^2, such that the survival probability monotonically increases for increasing Earth-Sun distance and therefore a similar qualitative behavior is to

be expected. The main quantitative difference is in the ratio of the number of events detected in the perihelion and in the aphelion, which may be accounted for by varying the background rate and the incoming neutrino flux. This explains the existence of islands. For values of Δm^2 in between islands, the survival probability either increases *and* decreases for varying Earth-Sun distance, or monotonically *decreases*. The exact location of the islands and their widths can only be understood by analyzing the fit procedure, in particular the minimization of χ^2 with respect to the background rate and the incoming neutrino flux. Note that there are no "islands" above $\Delta m^2 \gtrsim 2.5 \times 10^{-10}$ eV^2. This is because when the oscillation length is small enough (or Δm^2 large enough), the survival probability *cannot* only increase for increasing Earth-Sun distance, but necessarily reaches a maximum before the aphelion, and then decreases, independent of what the survival probability at the perihelion is. This situation is qualitatively different from the low point.

In the case of the high point: initially the survival probability is close to unity, decreases sharply as the Earth moves further from the Sun, and then grows rapidly, reaching a maximum when the Earth is close to its aphelion, because the oscillation length is smaller than ΔL. In this case, little variations in the oscillation length, *i.e.* Δm^2, produce big qualitative changes, including the position and number of maxima and minima. There is still a small ambiguity (*i.e.* two "islands") in determining Δm^2 for the high point. This happens when the oscillation length is such that the minimum of the survival probability happens in March/October and the survival probability is

large enough at the perihelion and the aphelion. The fact that the absolute values of the number of recoil electrons detected are different is taken care of by varying the signal and the background.

In conclusion, if Nature chose neutrino oscillation parameters such that $\sin^2 2\theta$ is large and $\Delta m^2 \approx$ few $\times 10^{-10}$ eV^2, Borexino should be able to measure these parameters independent of the SSM and any knowledge of the number of background events, with good precision (especially in Δm^2). If $\Delta m^2 \approx$ several $\times 10^{-11}$ eV^2, the determination of oscillation parameters is not as precise. Better precision can be achieved at KamLAND, but the ambiguity of solutions in the "low" Δm^2 region still remains.

3.4 Exclusion of Vacuum Oscillations

In this section, we address the issue of what the experiments can conclude about vacuum oscillations if no discrepancy from the normal seasonal variation effect is detected. In this case, one may be able to measure the incoming neutrino flux, as outlined in Sect. 3.1. Two distinct possibilities will be considered: (1) the measured flux is consistent with the SSM prediction; (2) the measured flux is suppressed with respect to the SSM prediction.

In the first case, one would be inclined to trust the SSM prediction of the ^{7}Be neutrino flux and use it in the analysis to exclude vacuum oscillations. This will be discussed in Sect. 3.4.1. On the other hand, in the second case, it is not clear if the

reduced flux is due to MSW neutrino oscillations, an incorrect SSM prediction of the neutrino flux, etc. This will be discussed in Sect. 3.4.2.

3.4.1 If the Flux is Consistent with the SSM Prediction

We simulate "data" consistent with the SSM and the expected number of background events. The relevant numbers are quoted in Sect. 3.1. The "data" are binned into months (12 bins per year), and are illustrated in Fig. 3.11, assuming three years of Borexino running. We then fit to the "data" annual distributions that include neutrino oscillations for a given choice of $(\sin^2 2\theta, \Delta m^2)$, plus a constant background. The background rate and the incoming neutrino flux may be allowed to float in the fit, constrained to a positive number.

It is important to note that this is the opposite of what was done in Sect. 3.2, where the sensitivity of Borexino and KamLAND to vacuum oscillations was studied. There, the simulated "data" were consistent with vacuum oscillations, and one tried to fit a non-oscillation prediction to the "data" by varying the incoming flux and/or the background. Here, the "data" are consistent with no oscillations, and one tries to fit the "data" with a prediction which includes the effect of neutrino oscillations for fixed $(\sin^2 2\theta, \Delta m^2)$, by varying the incoming flux and/or the background. If both the background and the incoming flux are fixed, *i.e.* not allowed to vary in the fit procedure, the exclusion and the sensitivity regions are the same. On the other hand, if both the background rate and the incoming flux are allowed to float, the exclusion

region is expected to be smaller than the sensitivity region presented in Sect. 3.2, especially in the region $\Delta m^2 \lesssim 10^{-10}$ eV^2. This is due to the fact that a large number of points in the parameter space yield an annual variation of the ν_e flux which is much larger than 7%, but agrees with the shape of the normal seasonal variation. If in the fit procedure the signal is scaled down to reduce the amplitude of the variation and the background scaled up to increase the number of events, a good fit to the no oscillation case can be attained.

Fig. 3.13 shows, for three years of Borexino and KamLAND running, the region of the $(\sin^2 2\theta, \Delta m^2)$ parameter space excluded at 95% CL, if one allows the solar neutrino flux and the background rate to float within the positive numbers (in white), and if one assumes the solar neutrino flux calculated in the SSM within theoretical errors (in light plus white).

A few comments are in order. First, one notices that the KamLAND exclusion region is larger than the one excluded by Borexino. This is, of course, expected because of KamLAND's larger fiducial volume and therefore higher statistics. Second, when the solar neutrino flux is allowed to vary in the fit, the excluded region of the parameter space shrinks, as expected and discussed earlier. Third, one can safely claim that, if no discrepancies are detected in the seasonal variation spectrum, the "large" Δm^2 (several $\times 10^{-10}$ eV^2) set of vacuum solutions (see Figs. 3.9 and 3.10) will be excluded, even at Borexino. Even when no knowledge of the incoming neutrino flux is used, a reasonable portion of the "small" Δm^2 (several $\times 10^{-11}$ eV^2) set of

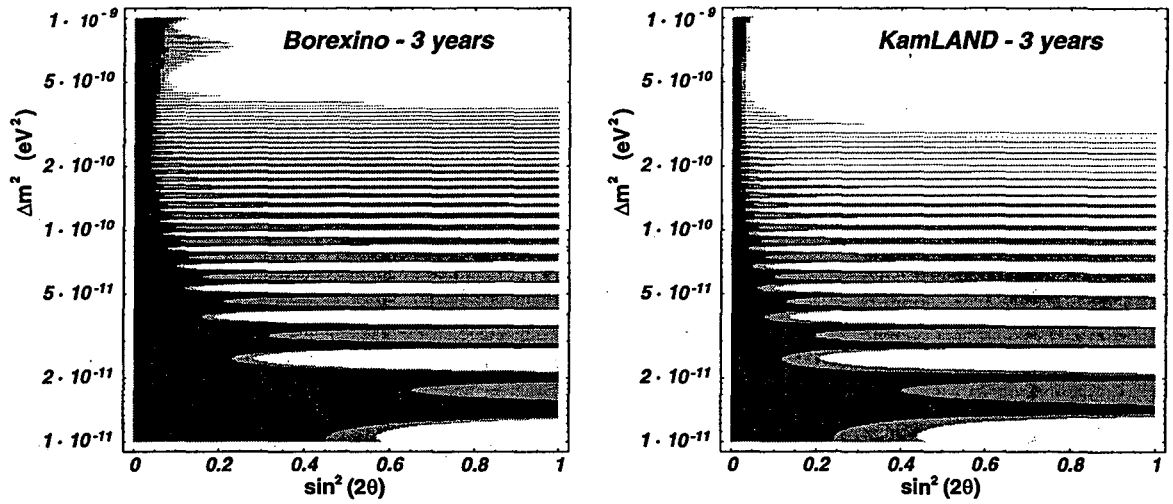

Figure 3.13: Region of the two neutrino oscillation parameter space excluded in the case of no neutrino oscillations if one assumes no knowledge of the background and no knowledge of the SSM (white) or knowledge of the SSM (light+white), after 3 years of Borexino (right) and KamLAND (left) running.

solutions is also excluded. When one assumes knowledge of the incoming neutrino flux, the entire allowed region is excluded.

If the background rate is larger than expected, the excluded region diminishes accordingly. This is because when the constant background is enhanced with respect to the oscillation signal it is easier to achieve a reasonable χ^2 for the fit even when the seasonal variations due to vacuum oscillations are significantly different from the no-oscillation case. In particular, when the background rate is large enough that the seasonal distribution of the data is statistically consistent with a flat one, a reasonable χ^2 for the fit can always be achieved simply by scaling the signal to zero and scaling up the background appropriately. Explicitly, after three years of Borexino (KamLAND) running the exclusion region vanishes if the background rate is $\sim$8 (40) times larger than anticipated, when both the background rate and the incoming neutrino flux are

allowed to float in the fit or ~500 (3000) times larger than anticipated when one assumes the neutrino flux predicted by the SSM.

3.4.2 If There is an Overall Suppression of the Flux

If there is an overall, *i.e.*, time-independent suppression of the flux (which is the case for the MSW solutions), the way to proceed towards excluding part of the vacuum oscillation parameter space is less clear. This is because such an experimental result neither agrees with the SSM prediction nor does it represent any "smoking gun" signature for neutrino oscillations, as is the case of anomalous seasonal variations. One does not know if the SSM prediction of the flux is simply wrong, or if there are neutrino oscillations consistent with one of the MSW solutions or both. Anyway, it is clear that (in general) the incoming neutrino flux should be considered unknown in the data analysis.

The most conservative option is to follow the same analysis done in the previous subsection, and allow both the incoming neutrino flux and the background rate to float in the fit. In this case, the excluded region of the two-neutrino oscillation parameter space is reduced significantly, and may completely disappear. This is because when the number of signal events is reduced the annual distribution is closer to flat and a good fit is obtained even when the would-be annual variations are very different. This is very similar to what was previously discussed at the end of the last subsection, where we discussed what happens if the background rate turns out to be

much larger than anticipated. Explicitly, after three years of Borexino running and a signal rate which is 21.3% of the SSM prediction (as one would obtain in the case of the small angle MSW solution), Borexino is unable to exclude any portion of the vacuum oscillation parameter space, while KamLAND can still exclude about one half of the "high" and "low" Δm^2 preferred regions. If the background rate can be estimated by other means with 10% uncertainty, Borexino and KamLAND will be able to exclude the entire "high" Δm^2 region and a significant portion of the "low" Δm^2 region.

In order to go beyond the most conservative analysis discussed above, one would have to look at the overall situation of the solar neutrino puzzle at the time of the data analysis. It is likely that one will be able to do much better. For example, solar neutrino oscillations might have already been established by the SNO experiment [44], and perhaps it is reasonable to assume the incoming solar neutrino flux predicted by the SSM. Then it would be possible to exclude a region of the parameter space as large as the one in Sect. 3.4.1 where one assumes the SSM flux. Another possibility is that Super-Kamiokande or SNO rules out the small angle MSW solution by studying the distortions of the electron energy spectrum [43, 23, 44], and a large suppression of the ^{7}Be solar neutrino flux would indicate that there is something wrong with the SSM. In this case, it is not clear how to proceed. We do not go into further discussions on all logical possibilities.

3.5 Conclusions

We have studied possible uses of the seasonal variation of the ^{7}Be solar neutrino flux at Borexino and KamLAND. Our results can be summarized as follows. Once the experiments accumulate enough data to see seasonal variations, the first step will be to determine if the observed pattern is consistent with the normal $1/L^2$ flux suppression. If a discrepancy is found, it will be a sign of vacuum oscillations. In this case, the seasonal variation of the data can be used to determine the oscillation parameters $\sin^2 2\theta$ and Δm^2. On the other hand, if the data are consistent with the normal pattern, the amplitude of the variation can be used to measure the ^{7}Be solar neutrino flux and to exclude a significant portion of the vacuum oscillation parameter space.

If the observed seasonal variations are consistent with the normal $1/L^2$ flux suppression, one can use the amplitude of the variation to determine what fraction of the observed recoil electrons are induced by the neutrinos coming from the Sun. This method is limited by statistics, and the accuracy is worse when the ^{7}Be solar neutrino flux is suppressed, as in the case of the small angle MSW solution. In fact, in Sect. 3.1 we found that in the case of a large suppression only KamLAND should be able to perform such a measurement, after 3 years of data taking. It is important to emphasize that we assumed the oscillation of electron neutrinos into other active flavors. In the case of oscillations into sterile neutrinos, the ^{7}Be solar neutrino flux might be almost absent, and in this case neither Borexino nor KamLAND are able

to perform a measurement of the flux using this technique.

An important advantage of this technique is that it does not require a separate estimate of the background rate, which may be a very difficult task. If the background rate can be reliably measured by some other means, one can obtain another measurement of the neutrino flux. In this case, the two results can then be compared for consistency, thus making the final result on the ^{7}Be neutrino flux much more trustworthy.

We also studied in great detail the effect of vacuum neutrino oscillations on seasonal variations. Our analysis shows that the outlook for discovering vacuum oscillations at both Borexino and KamLAND is very favorable. A very important finding in Sect. 3.2 is that the experiments may detect a deviation from the normal pattern of seasonal variations even without relying on the SSM prediction of the incoming neutrino flux or estimate of the background rate. The analysis would consist of trying to fit the observed data with the normal $1/L^2$ pattern, treating the incoming neutrino flux and the background rate as free parameters. With this technique, after three years of running Borexino should detect anomalous seasonal variations for almost all values of $(\sin^2 2\theta, \Delta m^2)$ preferred by the analysis of the neutrino flux data from Homestake, GALLEX, SAGE, and Super-Kamiokande, as illustrated in Fig. 3.9. The sensitivity region should be larger at KamLAND (Fig. 3.10). Results obtained in this way would be very robust. Both experiments are sensitive to an even larger portion of the parameter space if the background rate can be reliably estimated by auxiliary

measurements.

If anomalous seasonal variations are discovered, the data can be used to measure the oscillation parameters ($\sin^2 2\theta$, Δm^2). This issue was studied in Sect. 3.3. It was found that for $\Delta m^2 \gtrsim 10^{-10}$ eV^2 the experiments will be able to determine Δm^2 with good precision. At the same time, for $\Delta m^2 \lesssim 10^{-10}$ eV^2 there would be many "candidate islands" in the ($\sin^2 2\theta$, Δm^2) plane, and it will not be easy to resolve the ambiguity.

On the other hand, the absence of anomalous seasonal variations of the ^{7}Be solar neutrino flux data can be used to exclude regions of the vacuum oscillation parameter space. In Sect. 3.4 we presented the exclusion plots for both Borexino and KamLAND, after three years of running. An important lesson from that section is that in order to exclude a large portion of the preferred region, the experiments will need to either measure the background rate or rely on the SSM prediction for the neutrino flux. In the absence of both, the results are rather weak. This is to be contrasted with the situation in Sect. 3.2.

It is important to keep in mind that the simulated "data" is most of the time based on the SSM prediction for the ^{7}Be solar neutrino flux and the anticipated number of background events at Borexino and KamLAND. Our *numerical* results, therefore, even in the cases when we do not use the knowledge of the incoming neutrino flux or the background rate *at the analysis stage*, are not to be regarded as SSM and background rate independent. We would like to draw attention to our comments

at the end of Sects. 3.1 and 3.2 on how our results might change if these inputs are changed. We also assume only statistical errors in the data analysis, neglecting systematic uncertainties due to the lack of knowledge in the seasonal variation of the background rate. The inclusion of such effects is beyond the scope of this dissertation.

Overall our results indicate that the future Borexino results can lead to significant progress towards solving the solar neutrino puzzle. Furthermore, if KamLAND is also able to study solar neutrinos, one would have access to a larger data set, and more powerful results can be obtained.

Chapter 4

Earth Matter Effect at Borexino and KamLAND

It has been known for over a decade that the propagation of solar neutrinos through the Earth can result in a measurable variation in the observed neutrino event rates [45]. Reference [46], in particular, contains a good, thorough analysis of the expected day-night asymmetry for the Super-Kamiokande, Borexino, and SNO experiments. It states, however, that the asymmetry should vanish for the case of maximal neutrino mixing $\theta = \pi/4$. This point was generally accepted for 2 years until the authors of [47] pointed out that the asymmetry for $\theta = \pi/4$ is in fact nonzero. In this chapter we extend the previous analyses in several important aspects. First, we present an *enlarged parameter space*, where the vacuum mixing angle is

allowed to vary over its entire physical range from 0 to $\pi/2$[1]. We find that not only does the day-night asymmetry stay nonvanishing at maximal mixing, in agreement with [47], but that it also smoothly extends into the other part of the parameter space, $\pi/4 < \theta \leq \pi/2$. Second, we display the sensitivity regions of KamLAND and Borexino in this enlarged parameter space, using realistic numbers for the signal and background rates. In our analysis we use the χ^2 method, and study the effect of various binning schemes. Finally, we explore the possibility of using the neutrino regeneration data at the two experiments in question to measure the oscillation parameters.

This chapter is organized as follows. In Sect. 4.1 we review the day-night effect and present the day-night asymmetry expected for ^{7}Be neutrinos as a function of the two neutrino oscillation parameter space. We also introduce an enlarged parameter space, $0 \leq \theta \leq \pi/2$. In Sect. 4.2, we study the sensitivity of the KamLAND and Borexino experiments to the day-night asymmetry and to the zenith angle dependence of the ^{7}Be flux. In Sect. 4.3 we study the possibility of measuring the oscillation parameters if a significant day-night effect is observed at either Borexino or KamLAND. We contrast the analysis of the day-night asymmetry with the zenith angle distribution. In Sect. 4.4 we present a summary of our results and conclusions.

[1]This enlarged parameter space has already been mentioned in the context of three-flavor oscillations [48].

4.1 Electron Neutrino Regeneration in the Earth

As explained in Chapter 2, neutrino-matter interactions can dramatically affect the pattern of neutrino oscillations. The reason for this is that neutrino-matter interactions are flavor dependent, given that the matter distributions of interest (the Earth, the Sun) contain only first generation particles. One well-known consequence of this is that, in the case of neutrinos produced in the Sun's core, it is possible to obtain an almost complete $\nu_e \rightarrow \nu_{\text{other}}$ transformation even when the vacuum mixing angle is very small (see Sect. 2.3.3).

It has also been pointed out by several authors [45, 46, 47] that matter effects might also be relevant for neutrinos traversing the Earth. One experimental consequence of neutrino-Earth interactions is that the number of events detected during the day (when there are no neutrino-Earth interactions) can be statistically different from the number of events detected during the night. The Super-Kamiokande experiment has already presented experimental data which seem to slightly prefer a nonzero day-night asymmetry, even though the result is not yet statistically significant [49, 23] (the most recent result is $A_{DN} = 0.065 \pm 0.031 \pm 0.013$).

In this section we review the electron neutrino regeneration effect in the Earth and how it affects the observed solar neutrino flux. We also present the expected day-night asymmetry for ^{7}Be neutrinos at the KamLAND and Borexino sites.

4.1.1 The Day-Night Effect

If neutrinos have mass, it is very likely that, similar to what happens in the quark sector, neutrino mass eigenstates are different from neutrino weak eigenstates. Assuming for simplicity that only two neutrino states mix, we can relate the mass and flavor eigenstates as follows:

$$|\nu_1\rangle = \cos\theta|\nu_e\rangle - \sin\theta|\nu_\mu\rangle,$$
$$|\nu_2\rangle = \sin\theta|\nu_e\rangle + \cos\theta|\nu_\mu\rangle, \tag{4.1}$$

where θ is the vacuum mixing angle, $|\nu_1\rangle$ and $|\nu_2\rangle$ are the mass eigenstates with masses m_1 and m_2, respectively, and $\nu_e \leftrightarrow \nu_\mu$ mixing is considered. The mass-squared difference is defined as $\Delta m^2 \equiv m_2^2 - m_1^2$.

We are interested in the range of parameters that encompasses all physically different situations. First, observe that Eq. (4.1) is invariant under $\theta \to \theta+\pi$, $\nu_e \to -\nu_e$, $\nu_\mu \to -\nu_\mu$, *i.e.* $\theta \in [-\pi/2, \pi/2]$ and $\theta \in [\pi/2, 3\pi/2]$ are physically equivalent. Next, note that it is also invariant under $\theta \to -\theta$, $\nu_\mu \to -\nu_\mu$, $\nu_2 \to -\nu_2$, hence it is sufficient to only consider $\theta \in [0, \pi/2]$. Finally, it can also be made invariant under $\theta \to \pi/2-\theta$, $\nu_\mu \to -\nu_\mu$ by relabeling the mass eigenstates $\nu_1 \leftrightarrow \nu_2$, *i.e.* $\Delta m^2 \to -\Delta m^2$. Thus, all physically different situations are obtained if $0 \leq \sin^2\theta \leq 1$ and Δm^2 is positive, or $0 \leq \sin^2\theta \leq 1/2$ and Δm^2 can have either sign. In what follows, we will use the first parametrization ($\Delta m^2 > 0$), unless otherwise noted.

[7]Be neutrinos reach the Earth as an incoherent mixture of $|\nu_1\rangle$ and $|\nu_2\rangle$, as was

explained in Section 3.2 (see also [50, 47] and references therein), with probabilities P_1 and $P_2 = 1 - P_1$ as long as $\Delta m^2 \gtrsim 10^{-8}$ eV^2. P_1 is given in Eq. (2.57) in terms of the jumping probability P_c and its value depends on the details of the neutrino production and propagation inside the Sun, as presented in Sect. 2.3.3. The probability P_{ee} of detecting a ν_e on the Earth is given by

$$P_{ee} = P_1 P_{1e} + (1 - P_1) P_{2e} \ , \tag{4.2}$$

where P_{ie} is the probability that ν_1 (ν_2) is detected as a ν_e for $i = 1$ (2). Because $P_{1e} + P_{2e} = 1$ (always, independent of matter effects, because of the unitarity of the Hamiltonian), one can rewrite Eq. (4.2)

$$P_{ee} = P_1 + (1 - 2P_1) P_{2e} \ . \tag{4.3}$$

In the case of neutrinos detected during the day, $P_{2e} = \sin^2\theta$ (the vacuum result), while for neutrinos that traverse the Earth $P_{2e} = P_{2e}^E$ must be calculated numerically, and depends on the density profile of the Earth and the latitude of the location where the neutrinos are to be detected. One should also remember that muon or tau neutrinos still interact in the detector through neutral currents, although the even rate is down by a factor of $R \simeq 0.2$ compared to electron neutrinos. The day-night asymmetry ($A_{DN} \equiv$ (events detected during the night minus events detected during the day)/(total)) is, therefore,

$$A_{DN} = \frac{(1 - 2P_1)(P_{2e}^E - \sin^2\theta)(1 - R)}{(2P_1 + (1 - 2P_1)(P_{2e} + \sin^2\theta))(1 - R) + 2R} \ . \tag{4.4}$$

It is important to note that A_{DN} does not have to vanish, as used to be the general lore in the past, when $\sin^2\theta = 1/2$ (maximum mixing), as was clearly shown in [47]. A_{DN} does vanish, of course, when $P_1 = 1/2$ (a fifty-fifty mixture of mass eigenstates reaches the Earth).

It is interesting to note that, in the past, A_{DN} was always computed assuming that $\sin^2\theta \leq 1/2$. However, it is perfectly acceptable to have $\sin^2\theta > 1/2$, when the *heavy* mass eigenstate (ν_2) is predominantly ν_e. While in the case of vacuum oscillations physical results depend only on $\sin^2 2\theta$, in the case of neutrino-matter interactions $\sin^2\theta > 1/2$ leads to physically different results. Using $\sin^2 2\theta$ as a parameter in the latter case can be misleading, as $0 \leq \sin^2 2\theta \leq 1$ does not cover all physically distinct possibilities. Similar to what was pointed out in [47] for the transition between $\sin^2\theta < 1/2$ to $\sin^2\theta = 1/2$, we will show that for the entire range of $0 \leq \sin^2\theta \leq 1$ the behavior of A_{DN} is smooth. In Appendix C.1 we explain in detail how to extend the expression for P_1 to the case $\sin^2\theta > 1/2$.

4.1.2 The Day-Night Asymmetry at 36° and 42° North

We numerically compute the value of P_{2e}^E and A_{DN} for ^{7}Be neutrinos at KamLAND (latitude = 36.4° north) and Borexino (latitude = 42.4° north). We assume a radially symmetric exponential profile for the electron number density inside the Sun, and use the analytic expression for the survival probability of neutrinos produced in the Sun's core derived in [29], as presented in Appendix C.1. We appropriately integrate

over the ^{7}Be neutrino production region inside the Sun, using the results of the SSM [4], conveniently tabulated in [24].

We use a radially symmetric profile for the Earth's electron number density, given in [51], and the zenith angle exposure function for the appropriate latitude, which was obtained from [24]. For a plot of the electron number density profile in the Earth see Fig. 2 in [46] and for the zenith angle exposure function see the upper left-hand corner of Fig. 5 in [46]. The model predicts that the electron number density in the Earth's mantle varies in the range 2.1 to 2.7 moles/cm^3, while in the outer core the electron number density is significantly greater (4.6 to 5.6 moles/cm^3). Because of the latitude of Borexino and KamLAND, the solar neutrinos detected at these experiments will not travel through the inner core.

Fig. 4.1 depicts the constant day-night asymmetry contours for ^{7}Be neutrinos[2] at KamLAND and Borexino. It is important to note that, unlike conventionally done in the literature, the x-axis here is $\sin^2\theta$, not $\sin^2 2\theta$. To facilitate comparison with earlier results, we also depict the same information in the $(\Delta m^2, \sin^2 2\theta)$ plane in Fig. 4.2, where once again we vary the mixing angle in its entire physical range $0 \leq \theta \leq \pi/2$.

As Fig. 4.1 demonstrates, the asymmetry contours smoothly extend into the $\sin^2\theta > 0.5$ half of the parameter space. One can see that in that region the day-night asymmetry is non-zero and may, in fact, be quite large. This kind of behavior had

[2]We only assume ν_e oscillations into other active neutrino species.

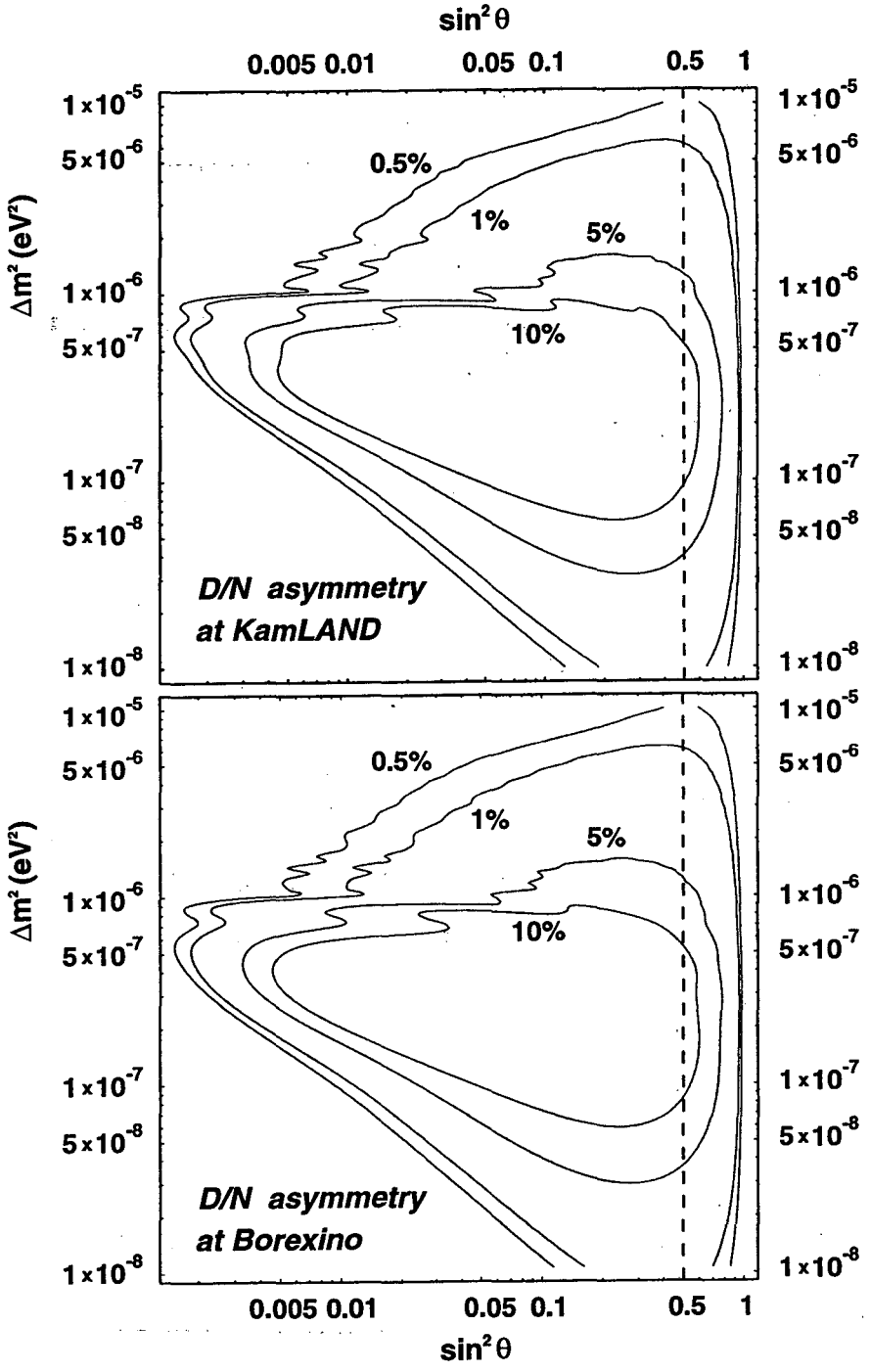

Figure 4.1: Constant day-night asymmetry contours (10%, 5%, 1%, 0.5%) in the $(\sin^2\theta, \Delta m^2)$-plane for ^{7}Be neutrinos at the KamLAND and Borexino sites. The vertical dashed line indicates $\sin^2\theta = 1/2$, where the neutrino vacuum mixing is maximal.

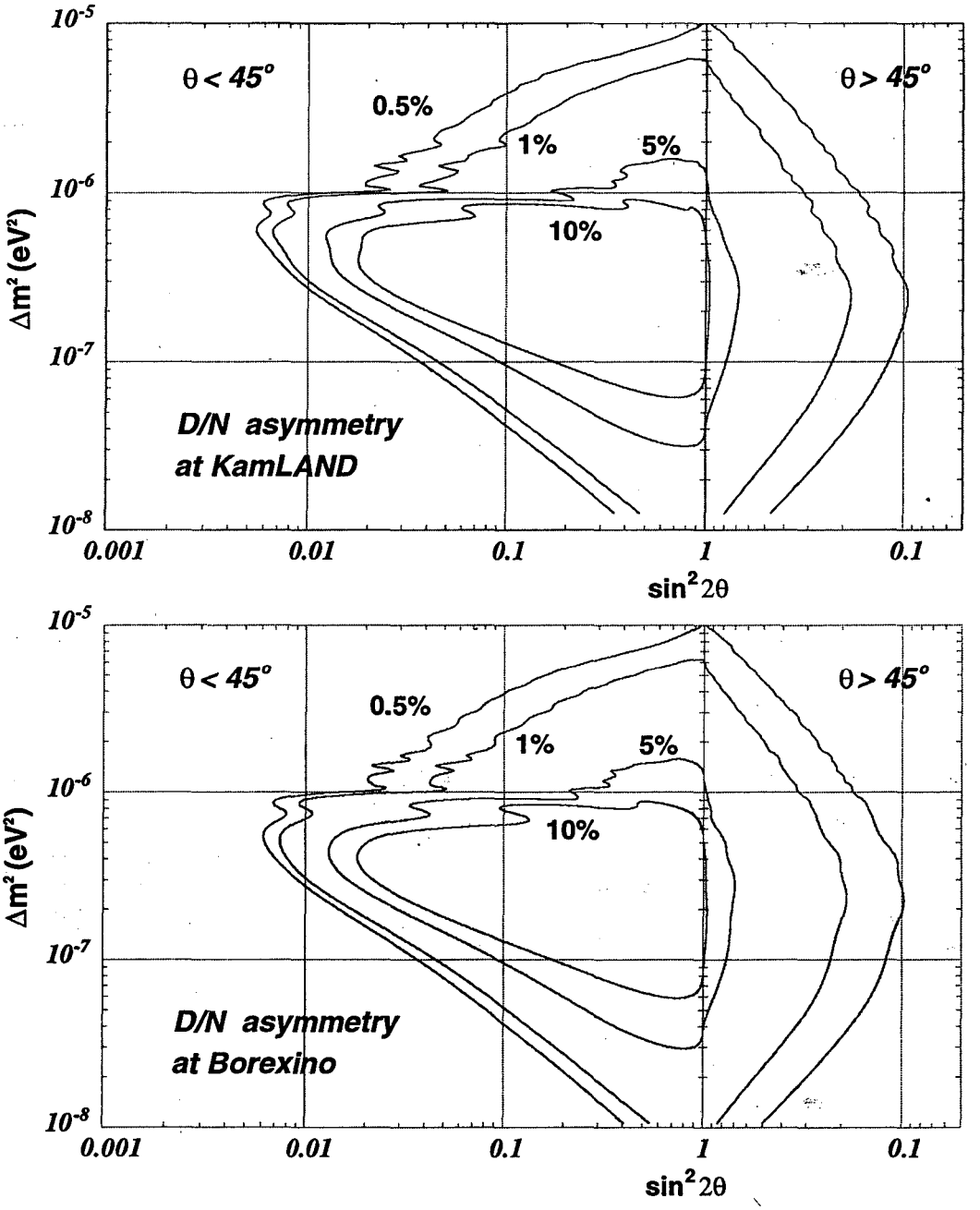

Figure 4.2: Constant day-night asymmetry contours (10%, 5%, 1%, 0.5%) in the $(\sin^2 2\theta, \Delta m^2)$-plane for ^{7}Be neutrinos at the KamLAND and Borexino sites. The right side of the plot, with decreasing scale, can also be thought of as $\Delta m^2 < 0$, $\theta < 45^0$.

already been seen in [48], for day-night asymmetry contours at Super-Kamiokande (see Fig. 11 in [48]). This is to be contrasted with conventional analyses, which choose axes as in Fig. 4.2, but only show the $0 \leq \theta \leq \pi/4$ half of the parameter space. As a result, contours there seem to abruptly terminate at maximal mixing.

It is also easy to see from our plots that, with the choice of variables as in Fig. 4.1, there is nothing special about maximal mixing. This point is somewhat obscured in the $(\Delta m^2, \sin^2 2\theta)$ plane, where it seems that the slope of the contours abruptly changes around $\sin^2 2\theta = 1$. The reason for this is that the Jacobian of the transformation from $\sin^2\theta$ to $\sin^2 2\theta$,

$$\frac{d(\sin 2\theta)}{d(\sin\theta)} = 2\frac{\cos 2\theta}{\cos\theta}, \tag{4.5}$$

vanishes at maximal mixing $\theta = \pi/4$. It can be argued, therefore, that $\sin^2\theta$ represents a more natural parametrization. From here on we will always use $\sin^2\theta$ as a parameter.[3]

The day-night asymmetry for $\theta = \pi/4$ is in general non-zero and, indeed, can be larger than 10%. Our analysis, thus, is in complete agreement with the findings of [47] and extends them to the other half of the parameter space. Note that constant day-night asymmetry contours do close as $\sin^2\theta \to 1$. This is expected, because in that limit, just like for $\sin^2\theta \to 0$, there is no neutrino mixing, and so P_{ee} goes trivially to 1 and A_{DN} vanishes.

[3]If one wishes to keep the symmetry between $\theta < \pi/4$ and $\theta > \pi/4$ for vacuum oscillations while avoiding the singular Jacobian, the best choice for the horizontal axis would be $\tan\theta$ in log scale, as was done in [48] in the context of three-flavor oscillations.

Almost all other features of the contours in Figs. 4.1 and 4.2 can also be understood analytically. Several physical effects are involved in shaping up the contours. In the low Δm^2 region the oscillation length in the Earth is comparable to the size of the Earth, independent of the value of Δm^2. This can be understood very easily in the approximation that the Earth's electron density is uniform. In that case the neutrino oscillation length is given by

$$L_{osc} = \pi \left[\left(\frac{\Delta m^2}{2E_\nu} \right)^2 + (\sqrt{2} G_F N_e)^2 - 2 \left(\frac{\Delta m^2}{2E_\nu} \right) \sqrt{2} G_F N_e \cos 2\theta \right]^{-1/2}, \qquad (4.6)$$

or numerically

$$\begin{aligned} L_{osc} &= 10.7 \times 10^4 \text{ km} \left[\left(\frac{\Delta m^2}{10^{-7} \text{ eV}^2} \right)^2 + \left(1.3 \frac{N_e}{1 \text{ mole/cm}^3} \right)^2 \right. \\ &\quad \left. - 2 \left(\frac{\Delta m^2}{10^{-7} \text{ eV}^2} \right) \left(1.3 \frac{N_e}{1 \text{ mole/cm}^3} \right) \cos 2\theta \right]^{-1/2}, \qquad (4.7) \end{aligned}$$

and, for $\Delta m^2/(2E_\nu) \ll \sqrt{2} G_F N_e$, $L_{osc} \to 8.2 \cdot 10^3 \text{ km} \times (1 \text{ mole/cm}^3/N_e)$.

For very small Δm^2 the asymmetry vanishes for two reasons. First, the MSW transition inside the Sun becomes non-adiabatic. For $\Delta m^2 \ll 10^{-5}$ eV^2, $\theta_M \simeq \pi/2$ (Eq. (2.50)) in the Sun's core and $P_1 \simeq P_c$ (Eq. (2.57)). As the value of the jumping probability P_c changes from 0 to $\cos^2\theta$ it passes through 1/2 (for $\theta < \pi/2$) where A_{DN} vanishes, according to Eq. (4.4). As can be deduced from Eq. (2.61), the contours of constant jumping probability P_c are approximately described by $\Delta m^2 \sin^2\theta =$ constant, provided $\sin^2\theta \ll 1$ and $\Delta m^2 \gg 10^{-9}$ eV^2. Second, the mixing angle in the Earth becomes close to $\pi/2$ and no regeneration takes place in that limit (see also Eq. (4.8) below, where $\theta_M \to \pi/2$ gives $P_{2e}^{av} \to \sin^2\theta$). Below the line $P_1 = 1/2$ the

asymmetry is negative and very small.

In the region $\Delta m^2 \gtrsim 3 \times 10^{-6}$ eV^2 neutrinos undergo many oscillations inside the Earth, as can be seen from Eq. (4.7). The relevant quantity in this case is the average survival probability, obtained after integrating over the zenith angle. One can understand the shape of the asymmetry contours in this region by, once again, approximating the electron number density in the Earth by a constant value. In this model, it is easy to show that, if a state $|\nu_i\rangle$ enters from vacuum into the Earth, the average survival probability inside the Earth is

$$\begin{aligned} P_{2e}^{av} &= \sin^2\theta_M + \sin^2(\theta - \theta_M)\cos 2\theta_M, \qquad |\nu_i\rangle = |\nu_2\rangle, \\ P_{1e}^{av} &= \sin^2\theta_M + \cos^2(\theta - \theta_M)\cos 2\theta_M, \qquad |\nu_i\rangle = |\nu_1\rangle. \end{aligned} \tag{4.8}$$

Here θ is the mixing angle in vacuum and θ_M is the mixing angle inside the Earth (see Eq. (2.50)). Obviously, $P_{1e}^{av} + P_{2e}^{av} = 1$. Using these expressions, one can compute the day-night asymmetry for this simplified model:

$$A = \frac{P_N + (1 - P_N)R - P_D - (1 - P_D)R}{P_N + (1 - P_N)R + P_D + (1 - P_D)R}, \tag{4.9}$$

where

$$\begin{aligned} P_D &= \sin^2\theta_\odot((1 - P_c)\sin^2\theta + P_c\cos^2\theta) + \\ &\quad \cos^2\theta_\odot((1 - P_c)\cos^2\theta + P_c\sin^2\theta), \\ P_N &= \sin^2\theta_\odot((1 - P_c)P_{2e}^{av} + P_cP_{1e}^{av}) + \\ &\quad \cos^2\theta_\odot((1 - P_c)P_{1e}^{av} + P_cP_{2e}^{av}). \end{aligned}$$

$\theta_\odot$ denotes the mixing angle at the production region in the core of the Sun, P_c

the jumping probability (Eq. (2.61)), and R is a contribution of $\nu_{\mu,\tau}$ interacting through the neutral current interactions in the detector. We found that for $N_e \sim 3-4$ moles/cm^3 the contours of constant A are in good agreement with the day-night asymmetry contours in Fig. 4.1 for $\Delta m^2 \gtrsim 3 \times 10^{-6}$ eV^2.

Using this simple model we can explain the behavior of the asymmetry contours in the large Δm^2 region. For example, according to Fig. 4.1, as $\sin^2\theta$ decreases for fixed Δm^2, the value of the asymmetry goes down. This happens because, while the difference in the numerator of Eq. (4.9) goes to zero, the denominator approaches a constant value due to the non-vanishing neutral current contribution. Notice that in a real experiment, in addition to the neutral current contribution, there will be a term proportional to the rate of background events, further decreasing the sensitivity. Thus, using asymmetry contours in this region to read off the sensitivity can be misleading. This would be even more obvious in the case of oscillations to a sterile neutrino. We will return to this issue in the next section.

Even more subtle features can be understood within this model. For instance, we found that the slight change of the slope seen for the 0.5% contour around $\sin^2\theta \sim 0.04$ is due to the significant deviation of the value of $\theta_\odot$ from $\pi/2$ in that region.

Finally, in the region $\Delta m^2 \sim 10^{-6}$ eV^2 the regeneration efficiency exhibits a very strong zenith angle dependence. Because the magnitudes of $\Delta m^2/(2E_\nu)$ and $\sqrt{2}G_F N_e$ in the core are almost equal, the mixing in the core is almost maximal ($\theta_M \sim \pi/4$, see Eq. (2.50)), while in the mantle it is small ($\theta_M \sim \pi/2$). As a result, for neutrinos

traveling through the outer core the conversion into ν_e is much more efficient than for ones going only through the mantle. The oscillations do not average out completely in this case, resulting in the presence of several wiggles. We have explicitly checked that these wiggles are not washed out by the effect of the finite width of the ^{7}Be line [40].

Our results for $\theta < \pi/4$ agree qualitatively with the results presented in [46] for the Borexino site. The agreement is not complete, however. For instance, the contours in [46] do not exhibit any wiggles in the range $\Delta m^2 \sim 10^{-6}$ eV^2.

4.2 The Earth Regeneration Effect at KamLAND and Borexino

In this section we study the sensitivity of the KamLAND and Borexino experiments to the day-night effect.

Borexino [36] is a dedicated ^{7}Be solar neutrino experiment. It is a large sphere containing ultrapure organic liquid scintillator (300 t) and can detect the light emitted by recoil electrons produced by elastic ν-e scattering. By looking in the appropriate recoil electron kinetic energy window, it is possible to extract a very clean sample of events induced by ^{7}Be neutrinos, if the number of background events is sufficiently small. Borexino expects, in the absence of neutrino oscillations, 53 neutrino induced events/day according to the SSM, and 19 events/day induced by background (mainly

radioactive impurities in the detector, see Chapter 3 and [36] for details).

The KamLAND experiment, located in the site of the original Kamiokande experiment, was initially designed as a reactor neutrino experiment. Recently, however, the fact that KamLAND might be used as a solar neutrino experiment has become a plausible and exciting possibility [37].

KamLAND is also a very large sphere containing ultrapure liquid scintillator (1 kt), and functions exactly like Borexino. The outstanding issue to determine if KamLAND will study solar neutrinos is if the background rates can be appropriately reduced. KamLAND expects, in the absence of neutrino oscillations, 466 neutrino induced events/kt/day according to the SSM, and 217 events/kt/day induced by background (mainly radioactive impurities in the detector, see Chapter 3 and [37] for details). We will consider a fiducial volume of 600 t, so that 280 (unoscillated) signal events/day and 130 background events/day are expected. We assume that the number of background events is constant in time.

We generate a histogram of the number of events expected in each of the N day and N night bins for different values of $(\Delta m^2, \sin^2\theta)$. The number of events per year in the i-th bin is

$$n_i \left(\frac{\text{events}}{\text{year}}\right) = 365 \left(\frac{\text{days}}{\text{year}}\right) (b_{\text{rate}} + s_{\text{rate}}(P_{ee}^i + (1 - P_{ee}^i)R)) \left(\frac{\text{events}}{\text{day}}\right) f_i, \quad (4.10)$$

where $s_{\text{rate}} = 280$ (53) events/day and $b_{\text{rate}} = 130$ (19) events/day for KamLAND (Borexino), P_{ee}^i is the electron neutrino survival probability in the i-th bin, R is

the ratio of the ν_e-e to $\nu_{\mu,\tau}$-e elastic cross sections[4] (see Chapter 3, at KamLAND (Borexino) $R = 0.214$ (0.213)) and f_i=(size i-th bin divided by the sum of the sizes of all the bins), such that $\sum_i^{2N} f_i = 1$. As an example, if there are 24 (12 day, 12 night) hour-bins, $f_i = 1/24$ for all i. In reality, we are interested in zenith angle bins, and in order to the determine f_i, the exposure function presented in [46] is used. Note that we assume only statistical uncertainties.

χ^2 is defined as

$$\chi^2 = \sum_{i=1}^{N} \frac{\left(n_i^{\text{night}} - n_i^{\text{day}}\right)^2}{\left(\sqrt{n_i^{\text{night}}}\right)^2 + \left(\sqrt{n_i^{\text{day}}}\right)^2} + N. \qquad (4.11)$$

The factor N is included in the definition of χ^2 in order to take statistical fluctuations of the data into account. A detailed explanation of the philosophy behind this procedure can be found in B.1.

It is important to comment at this point that, in light of the definition of χ^2 (Eq. (4.11)), the sensitivity of the experiments to the Earth matter effect does not require any input from the SSM, including the ^{7}Be solar neutrino flux, or from a direct measurement of the background rate. This is because we are comparing the night data with the day data, and no other inputs are required. Our quantitative results, however, depend on the expected number of signal and background induced events, since these quantities are used as input for the "data" sample.

We will define the sensitivity of a given experiment to the Earth matter effect by the value of χ^2, computed according to Eq. (4.11). The sensitivity defined in this way

[4] In the case of $\nu_e \leftrightarrow \nu_{\text{sterile}}$ oscillations, $R = 0$.

depends clearly on N, the number of day and night bins, and on f_i (see Eq. (4.10)), or on the "size of the bin". With the real experimental data, one will certainly consider many different types of analyses in order to maximize the sensitivity of the data to the neutrino regeneration in the Earth (options include computing moments of the zenith angle distribution, Fourier decomposing the data, maximum likelihood analysis, and others), but, since we analyze thousands of "data samples" (one for each value of $(\Delta m^2, \sin^2\theta)$), this simple χ^2 approach will suffice.

We consider two options for the size of zenith angle bins. In one of them, each bin has the same size, that is, the bins are equally spaced (*e.g.* $0^o-30^o, 30^o-60^o, 60^o-90^o$, etc). The other option is to choose the bin size such that the distribution of the day data is uniform. It is worthwhile to comment that the latter scheme may be considered the most natural one for KamLAND and Borexino, which are real time experiments with no directional capability. In these experiments, it is straightforward to organize the data into time bins, which then have to be translated into zenith angle bins by associating the time of the event with the position of the Sun in the sky.

Another issue to consider is the value of N which optimizes the sensitivity. It is clear that for $N = 1$ (the day-night asymmetry case) the statistical significance is enhanced for overall changes in the number of events, but for larger N, one should be more sensitive to distortions in the zenith angle distribution. Different binning schemes of the "data" for $\Delta m^2 = 1.12 \times 10^{-7}$ eV^2, $\sin^2\theta = 0.398$ and three years of KamLAND running are depicted in Fig. 4.3, for $N = 1$, $N = 10$ equally spaced bins,

and $N = 10$ "uniform" bins.[5]

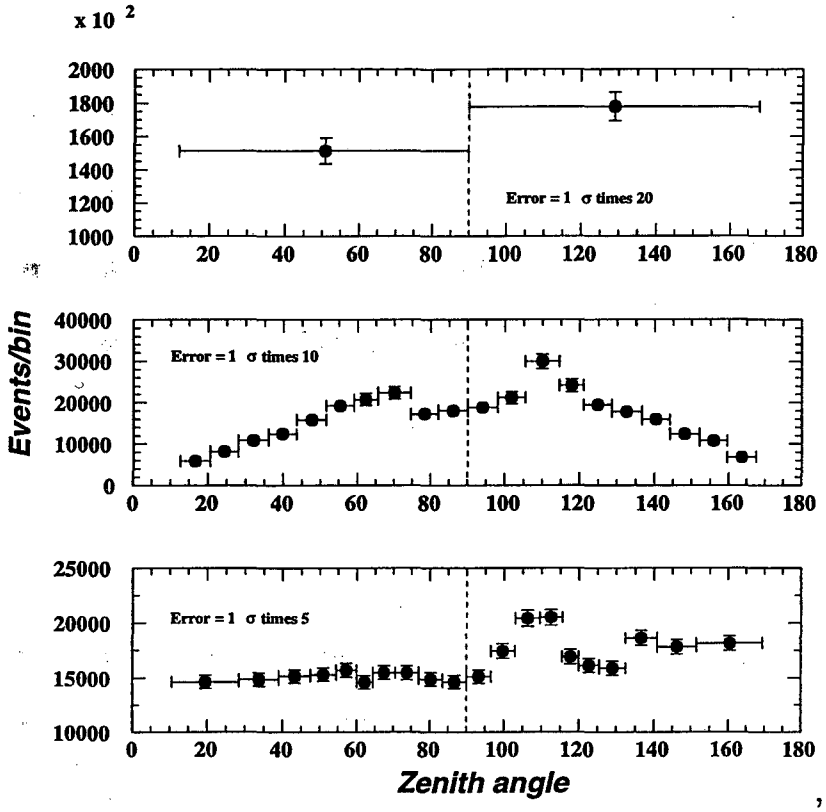

Figure 4.3: Different binning schemes, for $\Delta m^2 = 1.12 \times 10^{-7}$ eV^2, $\sin^2\theta = 0.398$: (a) $N = 1$ bin (the day-night asymmetry), (b) $N = 10$ equally spaced zenith angle bins, and (c) $N = 10$ "uniform" bins, where the day-time data is (roughly) uniformly distributed. The error bars contain statistical uncertainties only. We assume three years of KamLAND running.

Fig. 4.4 shows a comparison of the sensitivity reach of KamLAND after three years of running for two different binning schemes, $N = 1$ vs. $N = 10$ "uniform" bins. The contours are drawn at 95% C.L. One can easily see that for most of the parameter space, the best sensitivity is reached with the $N = 1$ case, while for a small region in the parameter space, when $\sin^2\theta \lesssim 0.1$ and $\Delta m^2 \sim 10^{-6}$ eV^2, the $N = 10$

[5]The residual non-uniformity seen in the figure is due to the fact that we used a discrete table of values for the exposure function.

scheme is more successful. This result is consistent with the analysis of Section 4.1.2. As explained there, for $\Delta m^2 \sim 10^{-6}$ eV^2 the data shows a large enhancement in the low zenith angle bin, while little effect in other bins. At Borexino this effect will be somewhat less pronounced because it is farther from the Equator.

One can see that the contours in Fig. 4.4 are similar in shape to the day-night asymmetry contours of Section 4.1.2, but quantitatively different. One important difference is that for $\Delta m^2 \gtrsim 10^{-6}$ eV^2 the χ^2 contours do not extend as far in the low $\sin^2\theta$ region as the asymmetry contours. While for low Δm^2 the 95% C.L. contour corresponds to the day-night asymmetry of roughly 0.5%, for $\Delta m^2 \gtrsim 10^{-6}$ eV^2 the corresponding value of the day-night asymmetry is at least two times greater. This phenomenon was already mentioned in Section 4.1.2. The difference occurs because the χ^2 analysis includes, in addition to the neutral current interactions, the constant background rate, thus eliminating the major shortcoming of the day-night asymmetry analysis.

In order to present the final sensitivity reach of KamLAND and Borexino, we combine the confidence level contour obtained in the different types of analyses, with different number of bins. Fig. 4.5 depicts the "optimal" 95%, 3σ, and 5σ confidence level (C.L.) contours for the sensitivity of three years of KamLAND and Borexino data to the day-night effect. The confidence levels are optimized by considering the union of same C.L. contours for all values of N and both binning schemes. The day-night asymmetry provides the best sensitivity reach for most of the parameter space,

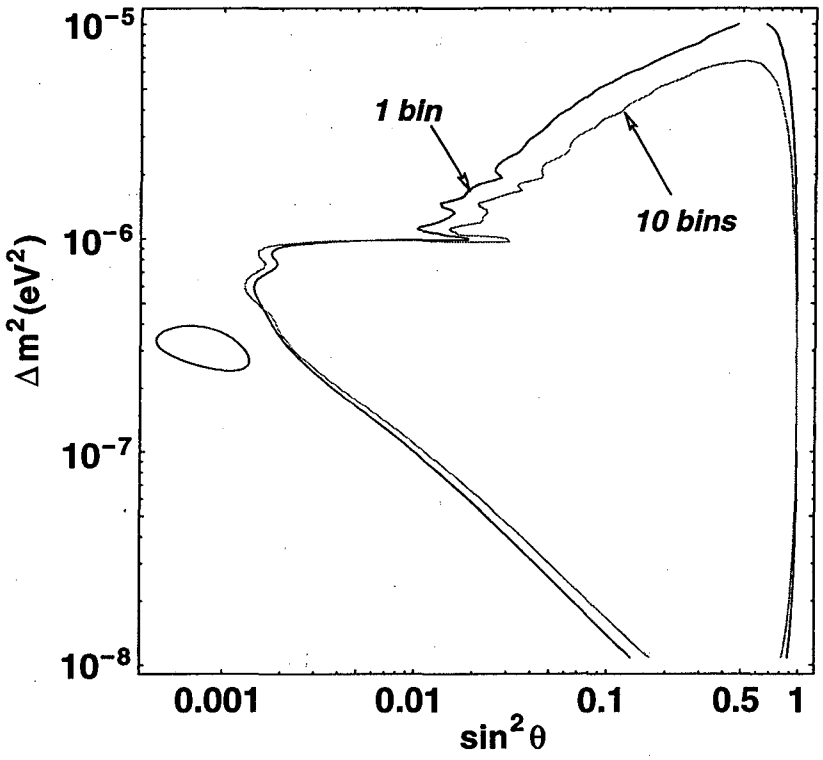

Figure 4.4: Comparison of the sensitivity reach of three years of KamLAND running with 1 bin and 10 uniform bins.

while the $N \approx 10$ uniform bins scheme at KamLAND increases the sensitivity for particular regions of the parameter space, as was discussed earlier.

Fig. 4.5 clearly demonstrates that in the case of the LOW MSW solution to the solar neutrino puzzle, both KamLAND and Borexino should be able to see a larger than 5σ effect, while in the case of the SMA no significant effect should be detected.[6] Both experiments are sensitive to a large portion of the parameter space which extends into $\theta > \pi/4$ region, where the heavy neutrino eigenstate is predominantly ν_e.

On the other hand, should no regeneration effect be observed, a large portion of the parameter space, including the entire LOW region might be excluded. The exclusion will require knowledge of the ^{7}Be neutrino flux, which can be measured, for example, by studying the seasonal variation of the observed event rate as discussed in Section 3.1. If the flux measured in this way turns out large and no day-night asymmetry is observed, one will be able to exclude the LOW solution without relying on the solar model. If, however, the measured flux is very small, the exclusion will be solar model dependent.

Since the sensitivity of Borexino (KamLAND) to the day-night asymmetry goes down to the 1.5% (0.5%) level, it is important to consider systematic effects in this measurement. It is, however, difficult to anticipate systematic uncertainties in the absence of data. We instead looked at the measurement of day-night asymmetry at Super-Kamiokande [49, 23]. The dominant systematic uncertainty there is the

[6] KamLAND may also be sensitive to a very small portion of the LMA solution.

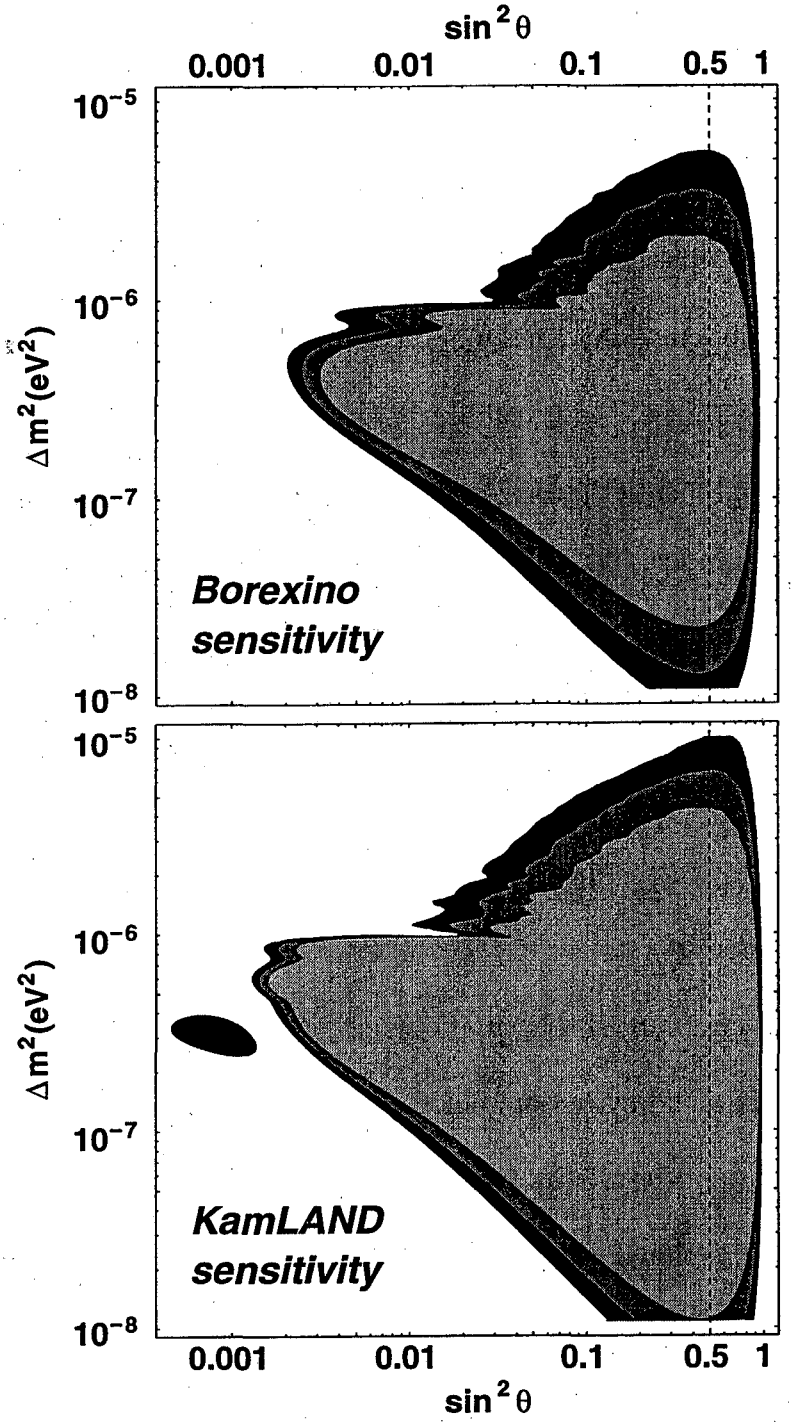

Figure 4.5: 95% (darkest), 3σ (dark), and 5σ (light) sensitivity confidence level (C.L.) contours for three years of KamLAND running. The LOW solution, which extends from $\Delta m^2 \sim 3 \times 10^{-8}$ eV^2 to $\Delta m^2 \sim 3 \times 10^{-7}$ eV^2 and has $\sin^2\theta \sim 0.3 - 0.5$ [3], is completely covered at more than 5σ C.L.

possible asymmetry in the detector, giving $\pm 0.6\%$.[7] Because the recoil electrons from ^{8}B neutrinos are forward peaked, the day (night) time data are detected primarily by the lower (upper) half the detector. A small possible gain asymmetry ([49] quotes 0.5%) for different zenith angle bins can result is a somewhat amplified difference in rates because the energy spectrum is rather steep close to the threshold energy (6.5 MeV). The energy calibration was done using electron LINAC, which at that time could shoot electrons only downwards and hence could not study the asymmetry well enough. The gain asymmetry is known to exist from the study of decay electrons in the cosmic ray muon data [52] as well as in spallation events.[8] We assume that this will not be an important systematic effect for Borexino or KamLAND because the energy deposit is basically isotropic (no directional capability) and hence the asymmetry in the detector should not result in a systematic effect in the day-night asymmetry.

The next largest systematic effect is the subtraction of background, $\pm 0.2\%$. If the background events are not completely isotropic, the subtraction depends on the direction and results in a systematic effect. Again at Borexino or KamLAND, the lack of directional correlation eliminates this systematic effect.

If we naively drop these two dominant systematic effects, the size of the total systematic uncertainty would be less than 0.1%. Of course, the sources of background

[7]Note that the talk [23] lists the systematic uncertainties in D/N ratio, which are twice as large as uncertainties in the asymmetry $(D-N)/(D+N) \approx ((D/N)-1)/2$.

[8]The gain asymmetry is now accurately measured using the ^{16}N source calibration and will be reduced dramatically.

are very different at Borexino or KamLAND. Possible differences in the temperature or Rn level between the day and night times could introduce new systematic effects, while our analysis assumed the same background level for day and night. This difference, however, can in principle be measured using the Bi-Po coincidence. Spallation background (such as ^{11}C) should not change between day and night.

Additionally, the experiments will need to consider other effects, such as the contribution of other neutrino sources or the uncertainty in the electron number density profile of the Earth. (More on the latter in the next section.) We also did not include in our analysis the contribution of neutrinos produced in the CNO cycle, which is about 10% of that from the ^{7}Be neutrinos. Although we cannot accurately predict the total systematic uncertainty at Borexino or KamLAND, we nonetheless find it encouraging that the dominant uncertainties at Super-Kamiokande are unlikely to affect these experiments.

4.3 Measuring the Oscillation Parameters

In this section, we discuss the possibility of measuring the value of $\Delta m^2, \sin^2\theta$ in the advent of a large day-night effect. In order to do this, data was simulated for $\Delta m^2 = 1.12 \times 10^{-7}$ eV^2, $\sin^2\theta = 0.398$, which is close to the LOW MSW solution to the solar neutrino puzzle [3]. For a plot of the "data" with different binning options, see Fig. 4.3.

In order to deal with the SSM solar neutrino flux and the background event rate,

we will conservatively "measure" both the background rate and the incoming solar neutrino flux by analyzing the seasonal variation (see Chapter 3) of the *day-time data only.* This measurement procedure will be incorporated in a four parameter χ^2 analysis (the parameters are Δm^2, $\sin^2\theta$, the solar neutrino flux s, and the background rate b) of the data. Explicitly,

$$\chi^2(\Delta m^2, \sin^2\theta, s, b) = \sum_{i=1}^{N} \frac{\left(\text{data}_i^{\text{night}} - \text{theo}_i^{\text{dn}}\right)^2}{\left(\sqrt{\text{data}_i^{\text{night}}}\right)^2} + \sum_{j=1}^{M} \frac{\left(\text{data}_j^{\text{day}} - \text{theo}_j^{\text{sea}}\right)^2}{\left(\sqrt{\text{data}_j^{\text{day}}}\right)^2}, \quad (4.12)$$

where $\text{data}_i^{\text{night}}$ is the night-time "data" binned into N night bins (as described in Sect. 4.2), $\text{data}_j^{\text{day}}$ is the day-time "data" binned into M "seasonal bins" (*e.g.* $j = 1, 2, \ldots 12$ months) as described in Section 3.2. $\text{theo}_i^{\text{dn}}$ is the prediction for the number of evens in the i-th night bin,

$$\text{theo}_i^{\text{dn}} = 365 \left[b + s(P_{ee,i}^{\text{night}} + (1 - P_{ee,i}^{\text{night}})R) \right] f_i, \quad (4.13)$$

similar to Eq. (4.10). b is the background rate in events per day and s is the number of events per day induced solar neutrinos according to the SSM prediction for the solar neutrino flux. Similarly, $\text{theo}_j^{\text{sea}}$ is the prediction for the day-time flux in the j-th seasonal bin (see Section 3.2),

$$\text{theo}_j^{\text{sea}} = \left[\int_{i-1}^{i} \text{d}t \left(b + s \frac{P_{ee} + (1 - P_{ee})R}{(1 - \epsilon \cos(2\pi t/\text{year}))^2} \right) \right] g_j, \quad (4.14)$$

where g_j is the number of days in the j-th bin and $\epsilon = 0.017$ is the eccentricity of the Earth's orbit.

It is simple to minimize χ^2 with respect to s and b, given that $\chi^2(s,b)$ is a quadratic function. The minimization with respect to Δm^2 and $\sin^2\theta$ is done numerically. Fig. 4.6 depicts the extracted contours in the $(\Delta m^2, \sin^2\theta)$-plane, in the case of 1 night bin and 10 "uniform" night bins, respectively.

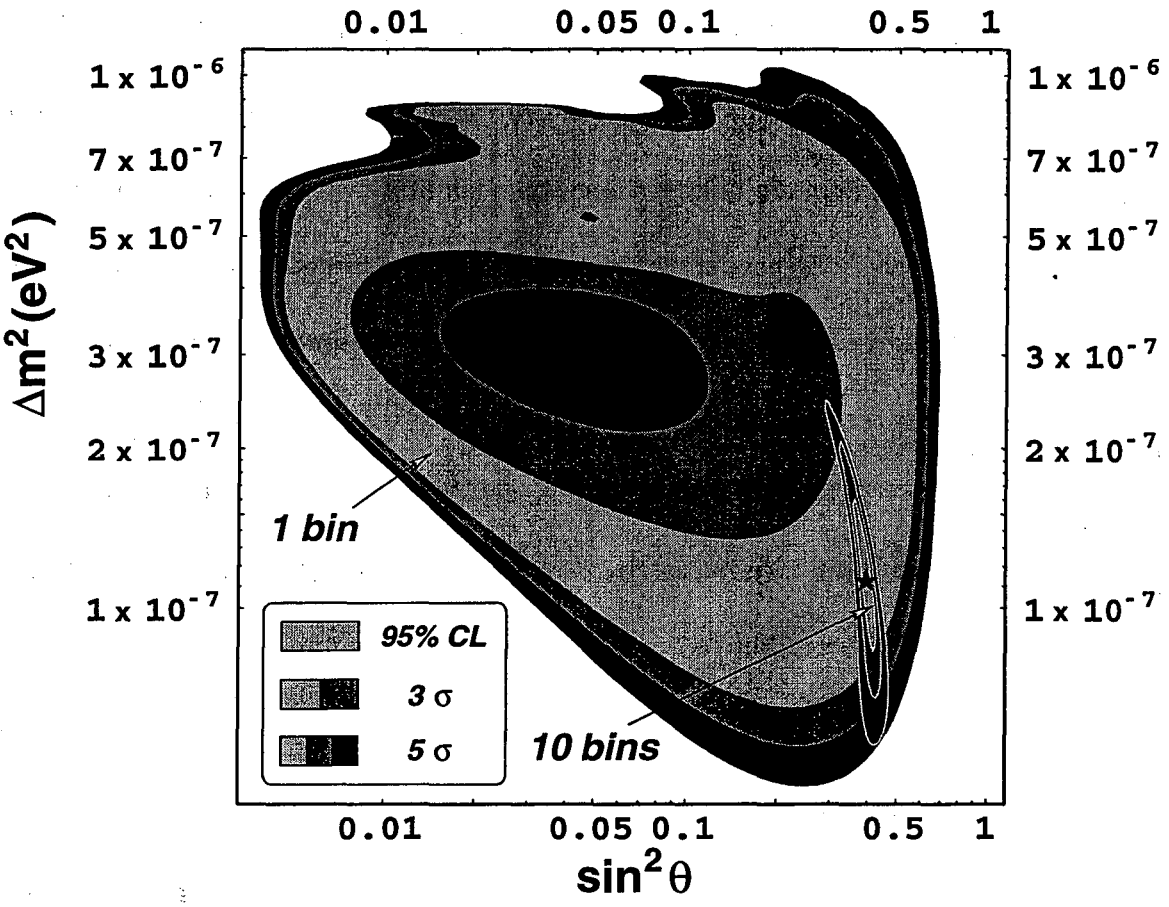

Figure 4.6: Measured values of $(\Delta m^2, \sin^2\theta)$ at KamLAND after three years of running. The data was generated for $\Delta m^2 = 1.12 \times 10^{-7}$ eV^2, $\sin^2\theta = 0.398$ (marked with the "star"). The regions obtained by using one night bin and ten uniform night bins are shown.

As Fig. 4.6 demonstrates, in the case of 1 night bin, one extracts values of Δm^2 and $\sin^2\theta$ which fall into "rings" which correspond roughly to $A_{DN} = A_{DN}^{\text{real}} \pm \Delta A_{DN}^{\text{real}}$,

where A_{DN}^{real} is the value of the day-night asymmetry for the input value of $\Delta m^2, \sin^2\theta$. In the case of more than one uniform bin, the ring degeneracy is broken, and a much more precise determination of the oscillation parameters is possible. This is expected, since for Δm^2 in this range the regeneration effect in the Earth exhibits a strong zenith angle dependence, as one can easily verified by looking at Fig. 4.3.

It is important to note that in the above analysis only statistical uncertainties were included, while in a real experiment one definitely will have to account for systematic effects as well. In particular, one will need to address the uncertainty in the Earth model used in the fit. In producing Fig. 4.6 the same Earth model [51] was used in generating the "data" and in the fit procedure. To understand the effect of using a "wrong" Earth model, we have repeated the above analysis using different Earth models in the fit. We found the results very encouraging. Even in the case when we used for the Earth profile a crude two-step model (a uniform density in the mantle and a uniform density in the core), the minimum of χ^2 occurred at $\Delta m^2 = 2.5 \times 10^{-7}$ eV^2, $\sin^2\theta = 0.24$, not far away from the true (input) value. Moreover, the χ^2 value at the minimum was much larger than the case with the "true" model ($\Delta\chi^2 = 183$ for 18 d.o.f.). This means that in a real experiment one will be able to adjust the Earth's model to achieve a better fit to the data. Because of the steep rise in χ^2 value as the Earth model is varied, the resulting χ^2 contours in the $(\Delta m^2, \sin^2\theta)$ parameter space should not be significantly larger than the ones presented here, where the Earth model is not varied. As a byproduct of the measurement of the neutrino oscillation

parameters, it might be possible to use the regeneration data to study the interior of the Earth!

4.4 Conclusions

We have studied the effect of the Earth matter on ^{7}Be solar neutrinos. We made use of an enlarged parameter space $0 \leq \theta \leq \pi/2$ and presented the sensitivity reach of the KamLAND and Borexino experiments in this space. Our results show that both experiments will be sensitive to the Earth regeneration effect in a large region which extends into the traditionally neglected $\theta > \pi/4$ part of the parameter space. In particular, for the LOW solution one expects to see a greater than 5σ effect. On the other hand, both experiments will see no day-night effect for the SMA solution and virtually no effect for the LMA solution.

If the experiments see a large Earth regeneration effect, it will be a powerful "smoking gun" signature of neutrino oscillations. Furthermore, as we have demonstrated, the results of the experiments can be used to measure the oscillation parameters. By studying the full zenith angle distribution, rather than the usual day-night asymmetry information, one might be able, in the case of the LOW solution, to perform a spectacular measurement of the parameters. In addition, it might be possible to use the zenith angle information to learn about the Earth electron density profile.

If, on the other hand, no Earth regeneration effect is detected, by combining this information with the flux measurement from seasonal variation of the event rate (see

Section 3.1), a large portion of the parameter space can be excluded. If the measured value of the ^{7}Be neutrino flux is large, the exclusion will be independent of a specific solar model.

Both the measurement of the oscillation parameters and the exclusion will require a thorough understanding of the systematic uncertainties. We have commented on some possible sources of such uncertainties in this chapter.

Overall, Borexino and KamLAND will provide crucial information about the solar neutrinos. Not only will the experiments measure the flux of the ^{7}Be solar neutrinos, but they will also be able to establish or exclude, without relying on solar models, the LOW solution based on the Earth regeneration effect and the vacuum oscillation solution based on the observed seasonal variation of the event rate. Together with results from Super-Kamiokande, SNO, and the KamLAND reactor neutrino experiment, this information can be used to finally unravel the 30-year-old solar neutrino puzzle.

Chapter 5

Studying the Full Parameter Space

In the last section we argued the importance of considering the full physical range of the neutrino mixing angle, $0 \leq \theta \leq \pi/2$, when studying the earth regeneration effect. One might wonder why the part of the parameter space with $\theta > \pi/4$ has been traditionally ignored in the literature. Possible reasons for this are that (1) the MSW solutions were expected to be confined to the $\theta < \pi/4$ region, and (2) the vacuum oscillation solutions were expected to be symmetric under $\theta \to \pi/2 - \theta$. In this chapter we reexamine both of these assumptions. We find that neither of them is justified.

5.1 MSW Effects in Vacuum Oscillations

In this section we point out that for solar neutrino oscillations with the mass-squared difference of $\Delta m^2 \sim 10^{-10} - 10^{-9}$ eV^2, traditionally known as "vacuum

oscillations", the solar matter effects are non-negligible, particularly for the low energy *pp* neutrinos. One consequence of this is that the values of the mixing angle θ and $\pi/2 - \theta$ are not equivalent, leading to the need to consider the entire physical range of the mixing angle $0 \leq \theta \leq \pi/2$ when determining allowed values of the neutrino oscillation parameters.

5.1.1 Introduction

The field of solar neutrino physics is currently undergoing a remarkable change. For 30 years the goal was simply to confirm the deficit of solar neutrinos. The latest experiments, however, such as Super-Kamiokande, SNO, Borexino, KamLAND, etc, aim to accomplish more than that. By collecting high statistics real–time data sets on different components of the solar neutrino spectrum, they hope to obtain unequivocal proof of neutrino oscillations and measure the oscillation parameters. Thus the physics of solar neutrinos is likely to become a precision science in the near future, and it is more important then ever to ensure that all relevant physical effects are taken into account and the right parameter set is used.

It has been a long–standing tradition in solar neutrino physics to present experimental results in the $\Delta m^2 - \sin^2 2\theta$ space and to treat separately the "vacuum oscillation" ($\Delta m^2 \sim 10^{-11} - 10^{-9}$ eV^2) and the MSW ($\Delta m^2 \sim 10^{-8} - 10^{-3}$ eV^2) regions. In the vacuum oscillation region the neutrino survival probability (*i.e.* the probability to be detected as ν_e) was always computed according to the canonical formula, Eq.

(2.29). Eq. (2.29) makes $\sin^2 2\theta$ seem like a natural parameter choice. As $\sin^2 2\theta$ runs from 0 to 1, the corresponding range of the mixing angle is $0 \leq \theta \leq \pi/4$. There is no need to treat separately the case of $\Delta m^2 < 0$ (or equivalently $\pi/4 \leq \theta \leq \pi/2$), since Eq. (2.29) is invariant with respect to $\Delta m^2 \to -\Delta m^2$ $(\theta \to \pi/2 - \theta)$.

The situation is different in the MSW region, since neutrino interactions with matter are manifestly flavor-dependent. It is well known that for $|\Delta m^2| \gtrsim 10^{-8}$ eV^2 matter effects in the Sun and Earth can be quite large. In this case, if one still chooses to limit the range of the mixing angle to $0 \leq \theta \leq \pi/4$, one must consider both signs of Δm^2 to describe all physically inequivalent situations. As was argued in Chapter 4, to exhibit the continuity of physics around the maximal mixing, it is more natural to keep the same sign of Δm^2 and to vary the mixing angle in the range $0 \leq \theta \leq \pi/2$.

Historically, a possible argument in favor of not considering $\theta > \pi/4$ in the MSW region might have been that this half of the parameter space is "uninteresting", since for $\theta > \pi/4$ there is no level-crossing in the Sun and the neutrino survival probability is always greater than 1/2 (see Appendix C.1). However, a detailed analysis reveals that allowed MSW regions can extend to maximal mixing and beyond, as will be explored in the next section (see also [53] and [54] for a treatment of 3- and 4- neutrino mixing schemes).

In this section we point out that for solar neutrinos with low energies, particularly the *pp* neutrinos, solar matter effects can be relevant even for $\Delta m^2 \sim 10^{-10} - 10^{-9}$ eV^2. These effects break the symmetry between θ and $\pi/2 - \theta$ making it necessary to

consider the full physical range of the mixing angle $0 \leq \theta \leq \pi/2$ even in the "vacuum oscillation" case.

5.1.2 Theoretical Framework

For simplicity we limit our consideration to the two-neutrino case. If neutrino masses are nonzero then, in general, the mass eigenstates $|\nu_{1,2}\rangle$ are different from the flavor eigenstates $|\nu_{e,\mu}\rangle$. The relationship between the two bases is given in terms of the mixing angle θ:

$$|\nu_1\rangle = \cos\theta|\nu_e\rangle - \sin\theta|\nu_\mu\rangle,$$
$$|\nu_2\rangle = \sin\theta|\nu_e\rangle + \cos\theta|\nu_\mu\rangle. \tag{5.1}$$

In our convention $|\nu_2\rangle$ is always the heavier of the two eigenstates, *i.e.* $\Delta m^2 \equiv m_2^2 - m_1^2 \geq 0$. Then, as already mentioned, $0 \leq \theta \leq \pi/2$ encompasses all physically different situations.

Neutrinos are created in the core of the Sun and exit the Sun in the superposition of the mass eigenstates. If the transition from the Sun's core to vacuum is *adiabatic*, the exit state is purely $|\nu_2\rangle$ [1]. In the case of a *nonadiabatic* transition there is also a nonzero probability P_c (a "level crossing" probability) to find the neutrino in the $|\nu_1\rangle$ state. In terms of P_c, the survival probability for neutrinos arriving at the Earth has

[1] Assuming the neutrino is in the heavy Hamiltonian eigenstate at the production point in the core. This assumption is valid as long as $\Delta m^2/E_\nu \lesssim 10^{-5}$ eV^2/MeV, see Chapter 4

the form (see Eq. (3.14) of Chapter 3.2, [26, 55])

$$\begin{aligned} P &= P_c \cos^2\theta + (1-P_c)\sin^2\theta \\ &+ 2\sqrt{P_c(1-P_c)}\sin\theta\cos\theta\cos\left(2.54\frac{\Delta m^2 L}{E_\nu}+\delta\right). \end{aligned} \tag{5.2}$$

Here L is the Earth–Sun distance and δ is a phase acquired when neutrinos traverse the Sun. Units are the same as in Eq. (2.29). In the adiabatic limit $P_c = 0$ and Eq. (5.2) yields $P = \sin^2\theta$. Neutrinos exit the Sun in the heavy mass eigenstate and do not oscillate in vacuum. From Eqs. (2.61,2.62) we can see that this happens for $\gamma \gg 1$, $\gamma\cos^2\theta \ll \gamma$. The first condition is satisfied for sufficiently large mass splitting $\Delta m^2 \gg 10^{-9}\text{eV}^2(E_\nu/1\text{ MeV})$, while the second one in addition requires that the mixing angle is not too small, $\sin^2\theta \gg (10^{-9}\text{ eV}^2/\Delta m^2)(E_\nu/1\text{ MeV})$.

In the opposite limit of small Δm^2, when the neutrino evolution in the Sun is "extremely nonadiabatic", $P_c \to \cos^2\theta$. It is trivial to verify that Eq. (5.2) in this limit reduces to Eq. (2.29). It has been assumed that in the vacuum oscillation region this limit is reached. Remarkably, however, this may not be the case for the low energy solar neutrinos, especially *pp* neutrinos ($E_\nu \leq 0.42$ MeV).

The most reliable way to compute P_c is by numerically solving the Schrödinger equation in the Sun for different values of Δm^2 and θ. We do this using the latest available BP2000 solar profile [56]. The profile, kindly provided by John N. Bahcall, is shown in Fig. 5.1. Fig. 5.2 shows contours of constant P_c for the energy of ^{7}Be neutrino (solid lines). Note that the variable on the horizontal axis is $\tan^2\theta$. With this choice, points θ and $\pi/2-\theta$ are located symmetrically on the logarithmic scale

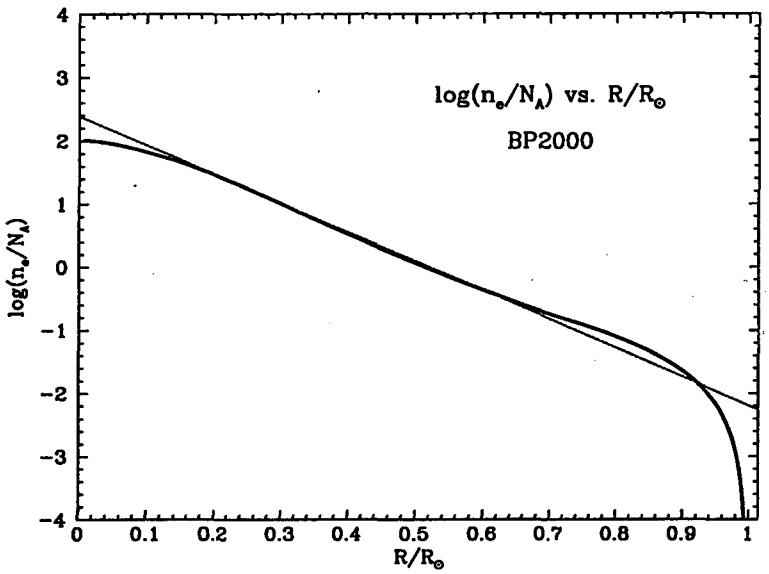

Figure 5.1: BP2000 solar electron number density profile (courtesy of John N. Bahcall).

about $\tan^2\theta = 1$ (see [48]). Other possible choices include θ or $\sin^2\theta$ on a linear scale, as was done in Chapter 4. The log scale here was chosen to unify the treatment with Sect. 5.2. The figure demonstrates that the contours are not symmetric with respect to the $\tan^2\theta = 1$ line, except in the region of $\Delta m^2/E_\nu \lesssim 10^{-10}$ eV^2/MeV, where the extreme nonadiabatic limit is reached. This simple observation is the crucial point of this section.

In the earlier chapters we used the analytical result for P_c, Eqs. (2.61) and (2.62), valid for the exponential solar profile $n_e \propto \exp(-r/r_0)$. As Fig. 5.1 shows, however, in the region relevant for vacuum oscillation, $0.9_\odot \lesssim R \lesssim R_\odot$, the profile falls off faster than the exponential with $r_0 = R_\odot/10.54 = 6.60 \times 10^4$ km (red line the figure).

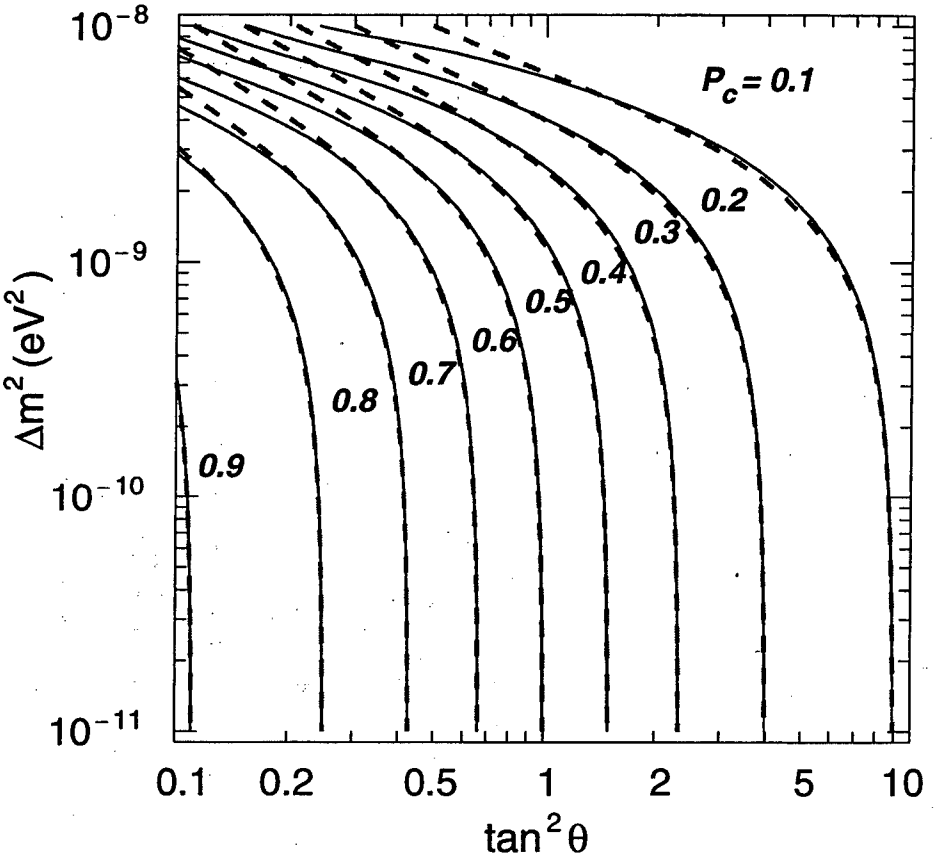

Figure 5.2: Contours of constant level crossing probability P_c for neutrino energy of 0.863 MeV (^{7}Be line). The solid lines are the results of numerical calculations using the BP2000 solar profile. The dashed lines correspond to using the exponential profile formula with $r_0 = R_\odot/18.4 = 3.77 \times 10^4$ km (see text).

Nevertheless, the equation

$$P_c = \frac{e^{\gamma \cos^2\theta} - 1}{e^{\gamma} - 1}, \tag{5.3}$$

where

$$\gamma = 2\pi r_0 \frac{\Delta m^2}{2E_\nu}, \tag{5.4}$$

can still be used with the appropriately chosen value of r_0. The dashed lines in Fig. 5.2 show the contours of P_c computed using Eq. (5.3) with $r_0 = R_\odot/18.4 = 3.77\times10^4$ km. As can be seen from the figure, the agreement between the two sets of contours for $\Delta m^2 \lesssim 4 \times 10^{-9}$ eV^2 is very good. Note that a similar result was arrived at in [30] for $\theta \leq \pi/4$, where the value of $r_0 = R_\odot \times 0.065 = 6.5 \times 10^4$ km was obtained.

Fig. 5.2 can also be used to read off the values of P_c for different neutrino energies, since P_c depends on E_ν through the combination $\Delta m^2/E_\nu$. It is obvious that for neutrinos of lower energies P_c starts deviating from its "extreme nonadiabatic" value at even smaller values of Δm^2, and vice versa. Consequently, as will be seen later, the solar matter effects on vacuum oscillations are most important at the gallium experiments, which are sensitive to the *pp* neutrinos, while the Super-Kamiokande experiment is practically unaffected.

Using Eqs. (5.3,5.2), it is possible to derive a corrected form of Eq. (2.29), by retaining in the expansion terms linear in γ:

$$\begin{aligned} P &= 1 - \left(1 + \frac{\gamma}{4}\cos 2\theta\right) \sin^2 2\theta \sin^2\left(1.27\frac{\Delta m^2 L}{E}\right) + \\ &+ O(\gamma^2) \end{aligned} \tag{5.5}$$

Notice that the first order correction contains $\cos 2\theta$ and hence is manifestly not invariant under the transformation $\theta \to \pi/2 - \theta$. Using Eq. (5.4) we see that for the pp neutrinos ($E_\nu \leq 0.42$ MeV) this correction is indeed non-negligible already for $\Delta m^2 \sim 10^{-10} - 10^{-9}$ eV^2.

With matter effects being relevant already at $\Delta m^2 \gtrsim 10^{-10}$ eV^2 one might wonder if the separation between vacuum oscillation solutions and MSW solutions is somewhat artificial. To fix the terminology, we will adopt a definition of vacuum oscillations as the situation when the value of neutrino survival probability depends on the distance L from the Sun, regardless of whether matter effects are negligible or not. The transition between the vacuum and the MSW regions will be discussed shortly.

5.1.3 Fits to data

To illustrate the role of matter effects in vacuum oscillations, we present fits to the total rates of the Homestake [19], GALLEX [21] and SAGE [20], and Super-Kamiokande [23] experiments. We combine experimental rates and uncertainties for the two gallium experiments and use the latest available 825-day Super-Kamiokande data set. The experimental results are tabulated in Table 2.3.

We fit the data to the theoretical predictions of the BP98 standard solar model [4]. Predicted fluxes and uncertainties for various solar reactions were kindly made available by J. N. Bahcall at [24]. To compute the rate suppression caused by neutrino

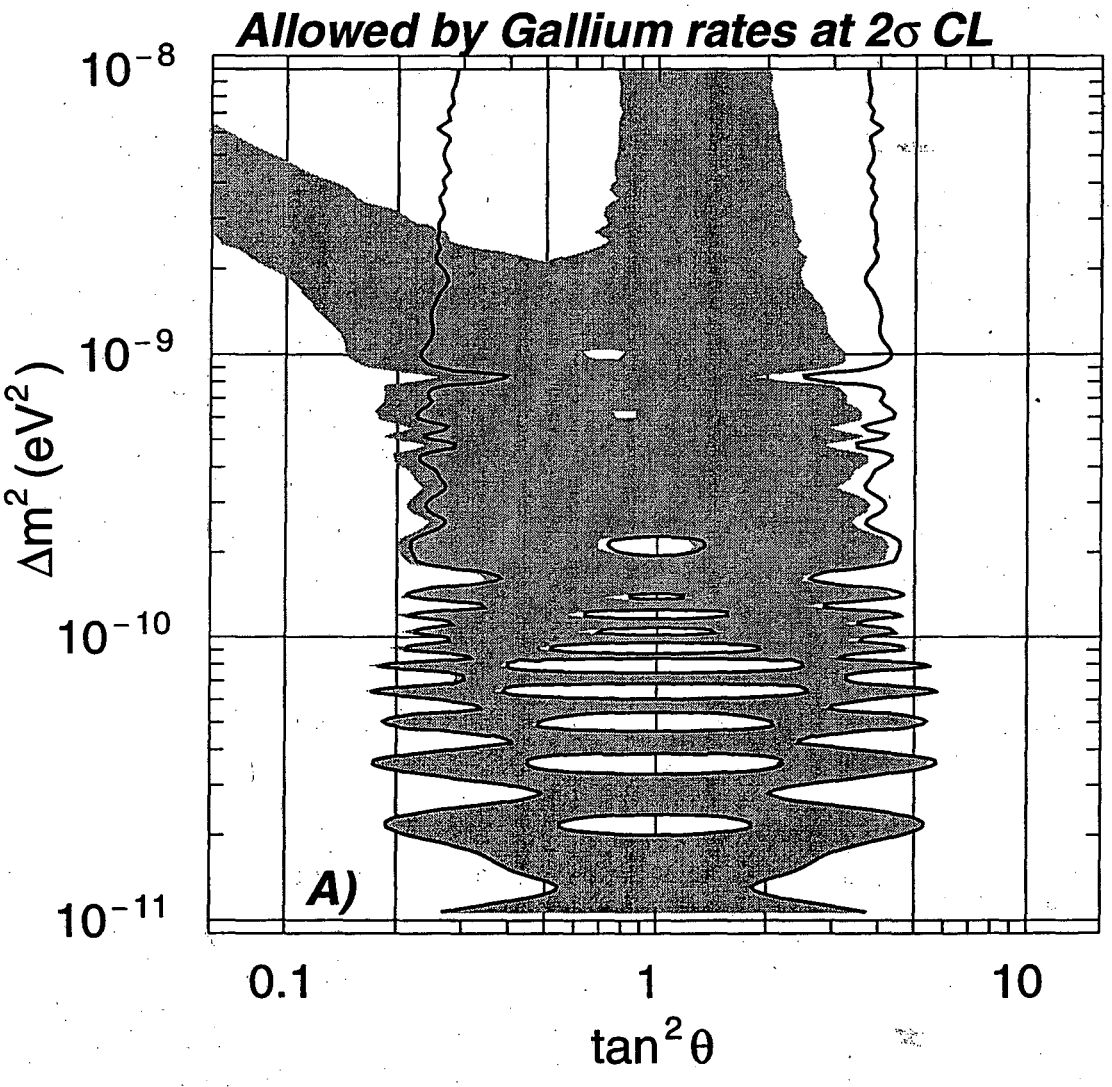

Figure 5.3: Region allowed by total rates of GALLEX and SAGE (shaded region). The region is obviously asymmetric for $\Delta m^2 > 10^{-10}$ eV^2, as a result of solar matter effects. Black outlines correspond to neglecting the solar matter effects.

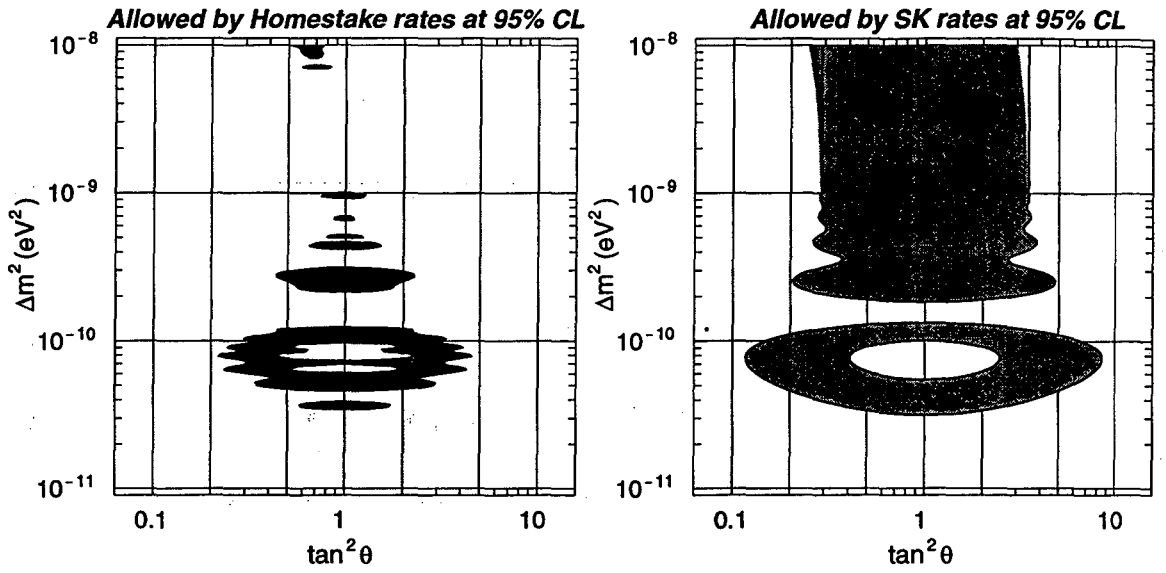

Figure 5.4: Regions allowed by total rates of Homestake and Super-Kamiokande. As expected, the regions show much less asymmetry than for the gallium case, Fig. 5.3. Black outlines correspond to neglecting the solar matter effects.

oscillations, we numerically integrate the neutrino survival probability, Eq. (5.2), over the energy spectra of *pp*, ^{7}Be, ^{8}B, *pep*, ^{13}N, and ^{15}O neutrinos. In addition, to account for the fact that the Earth–Sun distance L varies throughout the year as a consequence of the eccentricity of the Earth's orbit

$$L = L_0(1 - \epsilon \cos(2\pi t/\text{year})) \tag{5.6}$$

we also integrate over time to find an average event rate. In Eq. (5.6) t is time measured in years from the perihelion, $L_0 = 1.5 \times 10^8$ km is one astronomical unit, and $\epsilon = 1.7\%$.

In Fig. 5.3 we present the vacuum oscillation region allowed by the total rates of GALLEX and SAGE. In Fig. 5.4 we show the corresponding regions for Homestake and Super-Kamiokande. For comparison in all three plots we also show the regions

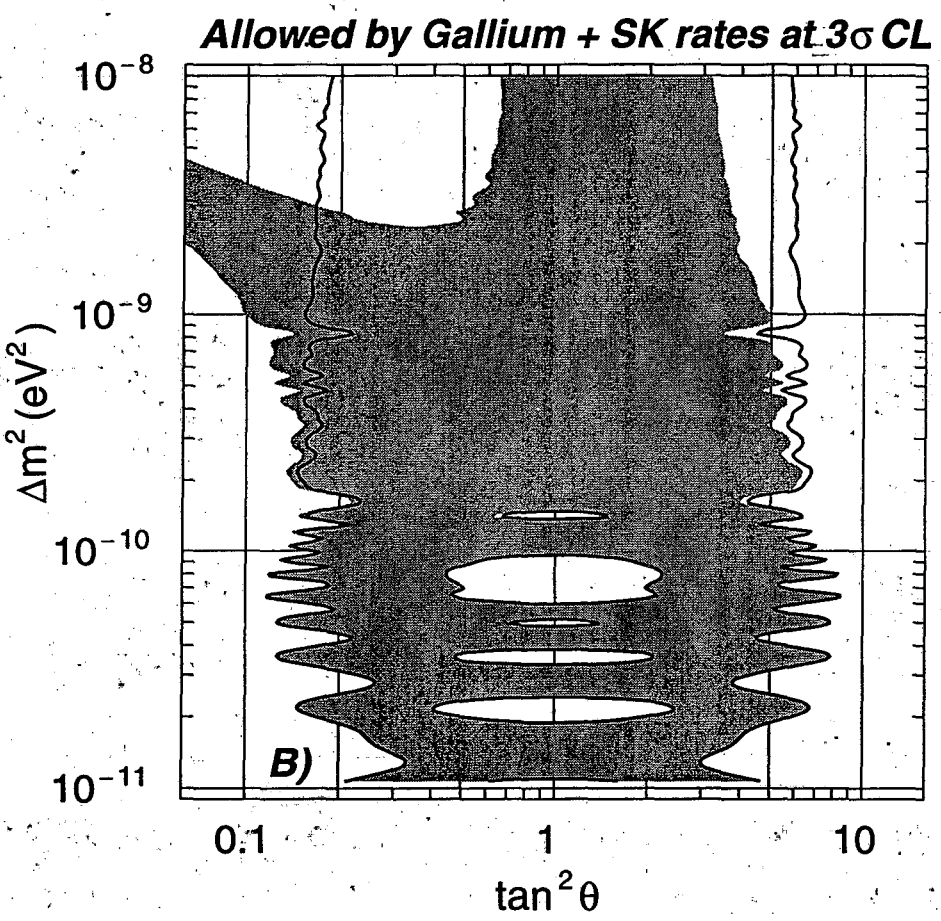

Figure 5.5: Allowed regions in the $\Delta m^2 - \tan^2\theta$ parameter space for vacuum oscillations based on rates of the gallium and water–Cherenkov experiments. Black outlines show the result of neglecting the solar matter effects.

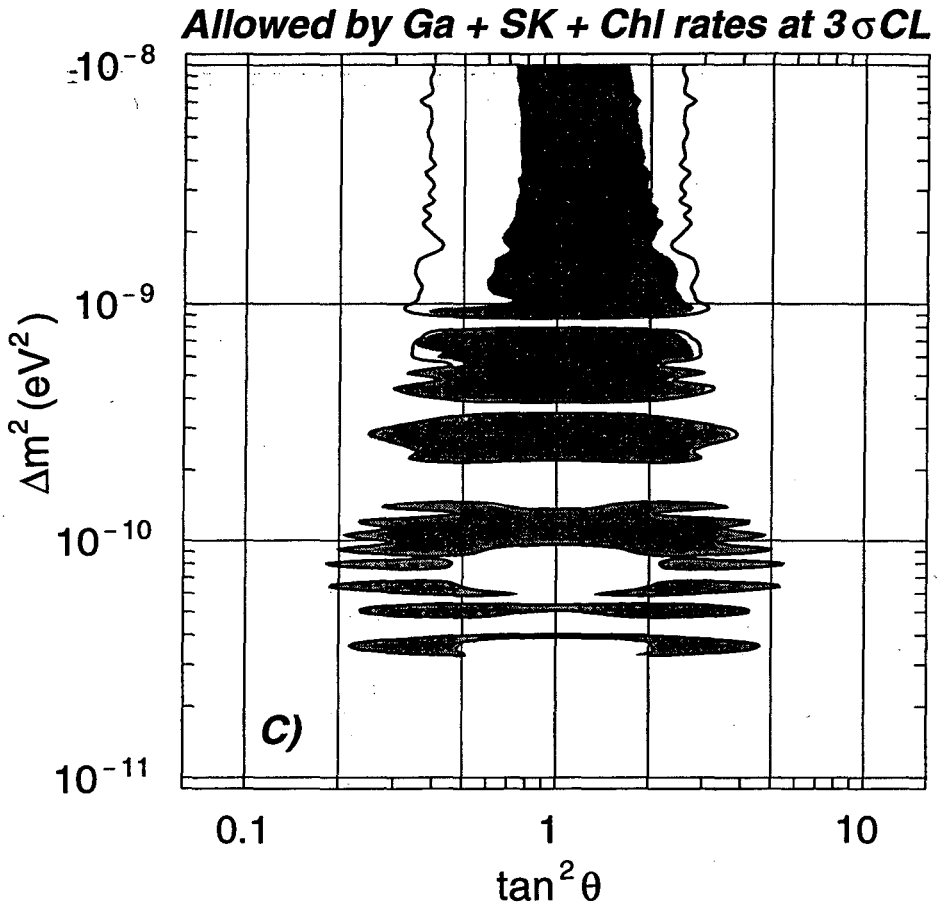

Figure 5.6: Allowed regions in the $\Delta m^2 - \tan^2\theta$ parameter space for vacuum oscillations based on rates of the gallium, chlorine, and water–Cherenkov experiments. Black outlines show the result of neglecting the solar matter effects.

one would obtain by neglecting the neutrino interactions with the solar matter (dark outlines), *i.e.* by setting $P_c = \cos^2\theta$ (black contours). Fig. 5.3 demonstrates that the matter effects are quite important for the gallium experiments, where the asymmetry is quite large for $\Delta m^2 \gtrsim 10^{-10}$ eV^2. As expected, the matter effects are small at Super-Kamiokande, since it detects neutrinos with $E_\nu \geq 6.5$ MeV. In all cases the allowed regions were defined as the sets of points where the theoretically predicted and experimentally observed rates are consistent with each other at the 95% C.L. for 1 d.o.f. ($\chi^2 = 3.84$) [2].

It is important to discuss the extent the vacuum oscillation region. There are two primary physical reasons why the neutrino event rate becomes independent of L for sufficiently large mass–squared splitting (and the seasonal variations disappear):

- *Adiabatic evolution in the Sun.* As $P_c \to 0$ the last term in Eq. (5.2) vanishes.
- *Integration over neutrino energy spectrum.* To compute the event rate one has to integrate Eq. (5.2) over neutrino energies. For sufficiently large Δm^2 the last term will average out to zero, leading effectively to the loss of coherence between the two mass eigenstates.

The detailed discussion of this phenomenon can be found in Section 3.2. Here for completeness we will present a brief summary of the result obtained there. As Δm^2 increases, coherence is first lost for reactions with broad energy spectra, such as *pp* and ^{8}B, and persist the longest for neutrinos produced as a part of a two-

[2] Notice that this is different from the conventional approach (see, for example, [53]).

body final state. The most important such reaction is electron capture by ^{7}Be nuclei ($^7\mathrm{Be}+e^- \rightarrow {}^7\mathrm{Li}+\nu_e$). Resulting ^{7}Be neutrinos have an energy spread of only a few keV, arising from the Doppler shift due to the motion of the ^{7}Be nucleus and the thermal kinetic energy of the electron. In order to properly take these effects into account, in our code we numerically integrate over the exact line profile, computed in [40]. The calculations show that the neutrino survival probability becomes independent of L for $\Delta m^2 \gtrsim 6 \times 10^{-9}$ eV^2. For this reason, we present our results for Δm^2 ranging from 10^{-11} eV^2 to 10^{-8} eV^2. Unfortunately, in the literature the traditional range is from 10^{-11} eV^2 to 10^{-9} eV^2 [2, 1, 54], although the allowed regions on the plots presented in all these papers seem to extend above 10^{-9} eV^2.

In Fig. 5.5 we present the vacuum regions allowed by the rates of GALLEX, SAGE, and Super-Kamiokande combined. The regions are drawn at 3σ C.L. (2 d.o.f., $\chi^2 = 11.83$, in the same convention as before). The distortions caused my the solar matter effects are clearly visible.

In Fig. 5.6 by the rates of all four experiments combined (3 d.o.f., $\chi^2 = 14.15$). In order to properly account for the correlation between the theoretical errors of the different experiments, we followed the technique developed in [57] and [53]. The allowed region exhibits a significant asymmetry for $\Delta m^2 > 6 \times 10^{-10}$ eV^2.

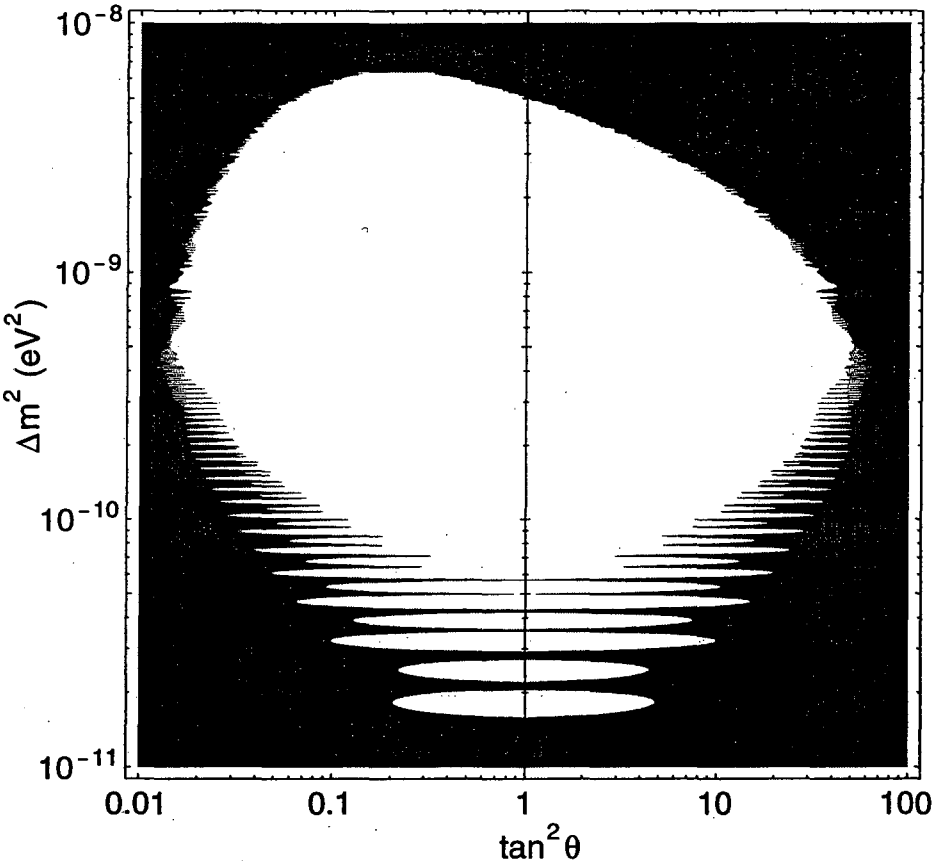

Figure 5.7: The sensitivity region of the Borexino experiment to anomalous seasonal variations for the full range of the mixing angle (95% CL). Notice the asymmetry for large Δm^2.

5.1.4 Sensitivity of Borexino experiment for $\theta > \pi/4$

An important question is how well future experiments will be able to cover vacuum oscillation solutions with $\theta > \pi/4$. In Fig. 5.7 we show the sensitivity of the Borexino experiment to anomalous seasonal variations for the entire physical range of the mixing angle $0 \leq \theta \leq \pi/2$. This is an extension of the analysis performed in 3.2, where the details of the procedure are described. The upper boundary of the sensitivity region shows a clear asymmetry as a result of the solar matter effects. This boundary can be used to approximately define the boundary between the vacuum and the MSW oscillation regions.

5.1.5 Conclusions

In summary, the preceding examples clearly illustrate the importance of including the solar matter effects when studying vacuum oscillation of solar neutrinos with $\Delta m^2 \gtrsim 10^{-10}$ eV^2. Because to describe such effects one has to use the full range of the mixing angle $0 \leq \theta \leq \pi/2$, future fits to the data should be extended to $\theta > \pi/4$. This seems especially important in light of the latest analyses [1], [54], which in addition to the total rates also use the information on the neutrino spectrum and time variations at Super-Kamiokande. In this case the allowed vacuum oscillation regions are mostly located in the $\Delta m^2 \gtrsim 4 \times 10^{-10}$ eV^2 part of the parameter space [54], precisely where the matter effects are relevant. (The best fit to the Super-Kamiokande electron recoil spectrum is achieved for $\Delta m^2 = 6.3 \times 10^{-10}$ eV^2, $\sin^2 2\theta = 1$ [1].) It would be very

important to repeat the analyses with the solar matter effects included, ideally using the exact electron density profile of the Sun.

Additionally, since ^{7}Be neutrinos remain (partially) coherent for $\Delta m^2 > 10^{-9}$ eV^2, it would be desirable to present the results of the fits in the range 10^{-11} eV$^2 < \Delta m^2 < 10^{-8}$ eV^2, as will be done in the next section.

5.2 MSW Regions

In this section we extend the analysis of the previous section to include the region of the MSW solutions. Our goal is to cover the entire range of Δm^2 relevant to the solar neutrino problem (10^{-11} eV$^2 < \Delta m^2 < 10^{-3}$ eV^2). Since matter effect distinguish the two parts of the parameter space $\theta < \pi/4$ and $\theta > \pi/4$, it is clear that MSW solutions are not symmetric with respect to $\theta \to \pi/2 - \theta$. Nevertheless, the region $\theta > \pi/4$ has largely been ignored in the literature.

Part of the reason for this neglect is that it is impossible to obtain ν_e survival probabilities less than one half when the two mass eigenstates are incoherent, *i.e.*, when the last term in Eq. (2.60) is absent. (This occurs in the so-called "MSW region" $10^{-8} \lesssim \Delta m^2 \lesssim 10^{-3}$ eV^2, see Sect 3.2.) Indeed, the data from the Homestake experiment [19] used to be about a quarter of the SSM prediction, and this could have been an argument for dropping the $\theta > \pi/4$ side entirely in the MSW region. However, the change from BP95 [39] to BP98 [4] calculations increased the Homestake result to about a third of the SSM with a relatively large theoretical uncertainty.

Therefore it is quite possible that the "MSW solutions" extend to the $\theta > \pi/4$ side as well. Moreover, some people question the SSM and/or the Homestake experiment, and perform fits by ignoring either (or both) of them [58]. We show below that some of the MSW solutions indeed extend beyond the maximal mixing and hence it is necessary to explore the $\theta > \pi/4$ side experimentally. If we further relax the theoretical prediction on the ^{8}B solar neutrino flux and/or ignore one of the solar neutrino experiments in the global fit, the preferred regions extend even deeper into the $\theta > \pi/4$ side.

We next present the results of global fits to the current solar neutrino data from water Cherenkov detectors (Kamiokande and Super-Kamiokande) [22, 23], a chlorine target (Homestake) [19] and gallium targets (GALLEX and SAGE) [21, 20] on the full parameter space. We do not include the spectral data from Super-Kamiokande [43] as it appears to be still evolving with time. The fit is to the event rates measured at these experiments only. In computing the rates we include not only the *pp*, ^{7}Be, and ^{8}B neutrinos, but also the ^{13}N, ^{15}O, and *pep* neutrinos. We use Eq. (2.60) with P_c computed in the exponential approximation for the electron number density profile in the Sun[3], and properly account for neutrino interactions in the Earth during the night with a realistic Earth electron number density profile by numerically solving Schrödinger equation as described in Chapter 4. Since the mixing angle at

[3]In our analysis in this section we use a constant value of $r_0 = R_\odot/10.54 = 6.60 \times 10^4$ km. As was pointed out in Sect. 5.1, in the vacuum oscillation region one should use a different value, $r_0 = R_\odot/18.4 = 3.77 \times 10^4$ km. Thus, the shape of the allowed vacuum oscillation regions in this section will be slightly different.

the production point in the Sun's core depends on the electron number density, we integrate over the production region numerically. We treat the correlations between the theoretical uncertainties at different experiments following Ref. [53]. To insure a smooth transition between the MSW and the vacuum oscillation region, we integrate over the energy spectrum (including the thermal broadening of the ^{7}Be neutrino "line") for $\Delta m^2 \leq 10^{-8}$ eV^2 and average the neutrino fluxes over the seasons. For $\Delta m^2 > 10^{-8}$ eV^2 we treat the two mass eigenstates as incoherent. Results are completely smooth at $\Delta m^2 = 10^{-8}$ eV^2, as expected. This allows us to fit the data from $\Delta m^2 = 10^{-11}$–10^{-3} eV^2 all at once, unlike previous analyses which separate out the "vacuum oscillation region" from the rest.

As was mentioned earlier, we take the global fit to the currently available data only as indicative of the ultimate result because we expect much better data to be collected in the near future to eventually supersede the current data set. We would like to keep our minds open to surprises such as the possibility that one of the earlier experiments was not entirely correct or that the theoretical uncertainty in the flux prediction was underestimated. In this spirit, we employ more conservative attitudes in the global fit than most of the analyses in the literature in the following three possible ways. (1) We allow higher confidence levels, such as 3 σ. (2) We relax the theoretical prediction on the neutrino flux. (3) We ignore some of the experimental data in the fit.

The global fit results are presented in Fig. 5.8 at the 2 σ (95% CL) and 3 σ

(99.7% CL) levels defined by $\chi^2 - \chi^2_{min}$ for two degrees of freedom. It is noteworthy that both the LMA and LOW solutions (we use the nomenclature introduced in [2]) extend to the $\theta > \pi/4$ side at the 3 σ level. At 99% CL, however, the LMA solution is confined to the $\theta < \pi/4$ side. This result is consistent with the two-flavor limit of the three-flavor analysis in [53] and the four-flavor analysis in [54], where the spectral data is included and the LOW solution extends beyond the maximal mixing at 99% CL. Another interesting fact is that the LOW solution is smoothly connected to the VAC solution, where the preferred region is clearly asymmetric between the two sides of the parameter space. Note that, at $\Delta m^2 \sim 10^{-9}$ eV^2, the allowed region is in fact bigger in $\theta > \pi/4$ side. The region $10^{-9} < \Delta m^2 < 10^{-8}$ eV^2 was, to the best of the authors' knowledge, never studied fully in the literature and this result demonstrates the need to study the entire Δm^2 region continuously without the artificial separation of the "MSW region" and "vacuum oscillation region," as traditionally done in the literature.

We next present a fit where the theoretical prediction of the ^{8}B flux is relaxed. Even though the helioseismology data constraints the sound speed down to about 5% of the solar radius [4], the core region where ^{8}B neutrinos are produced is still not constrained directly. Given the sensitive dependence of the ^{8}B flux calculation on the core temperature $\Phi_{^8B} \sim T^{18}$ [17], we may consider it as a free parameter in the fit. This can be done within the formalism of Ref. [53] by formally sending the error in $C_{\rm Be}$ to infinity. The result is presented in Fig. 5.9. The preferred region extends

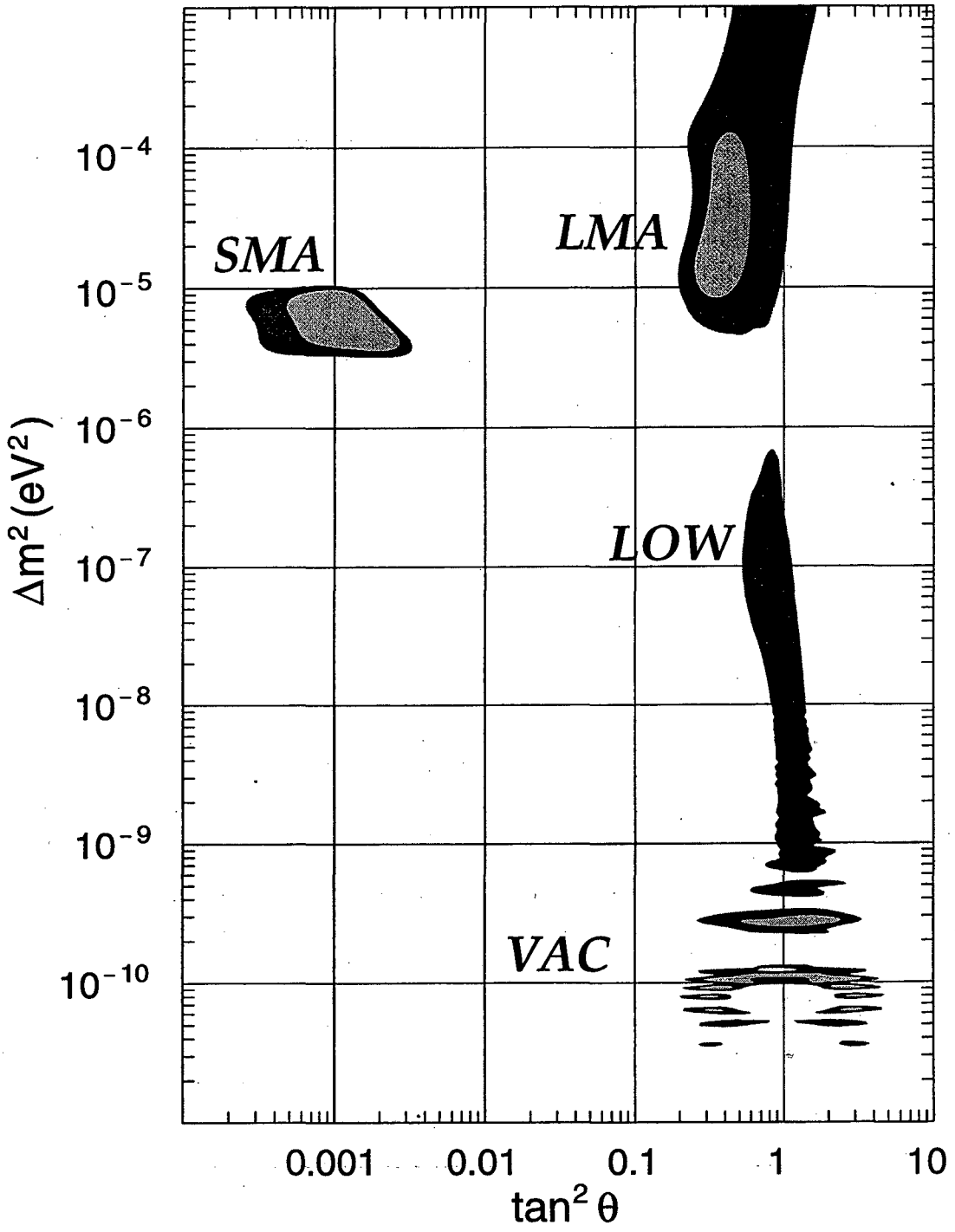

Figure 5.8: A global fit to the solar neutrino event rates at chlorine, gallium and water Cherenkov experiments. The regions are shown at 2 σ (light shade) and 3 σ (dark shade) levels. The region $\tan^2 \theta > 1$ corresponds to $\theta > \pi/4$.

farther into the $\theta > \pi/4$ side than the previous fit. Even though the LMA and LOW solutions are connected in this plot, the lack of a large day-night asymmetry at Super-Kamiokande would eliminate the range $3 \times 10^{-7} \lesssim \Delta m^2 \lesssim 10^{-5}$ eV^2 for $0.2 \lesssim \tan^2\theta < 1$ [49]. It is important for Super-Kamiokande to report their exclusion region for $\theta \gtrsim \pi/4$.

Finally, Fig. 5.10 shows a fit where the event rate measured at the Homestake experiment is not used. This may be a sensible exercise given that the neutrino capture efficiency was never calibrated in this experiment. The preferred region extends beyond the maximal mixing even at the 95% CL. Note also the asymmetry between the two sides of the parameter space even for $\Delta m^2 < 10^{-9}$ eV^2.

We expect the data of the current and next generation of solar neutrino experiments, such as Super-Kamiokande, SNO, GNO, Borexino, KamLAND, to eventually supersede the current data set. Therefore we regard the above global fits only as estimates of the ultimate results. The most important point is that all experimental collaborations should report their results, both exclusion and measurements, on both sides of the parameter space, without unnecessary theoretical bias towards the *theta* $< \pi/4$ side. We strongly urge the experimental collaborations to consider this point.

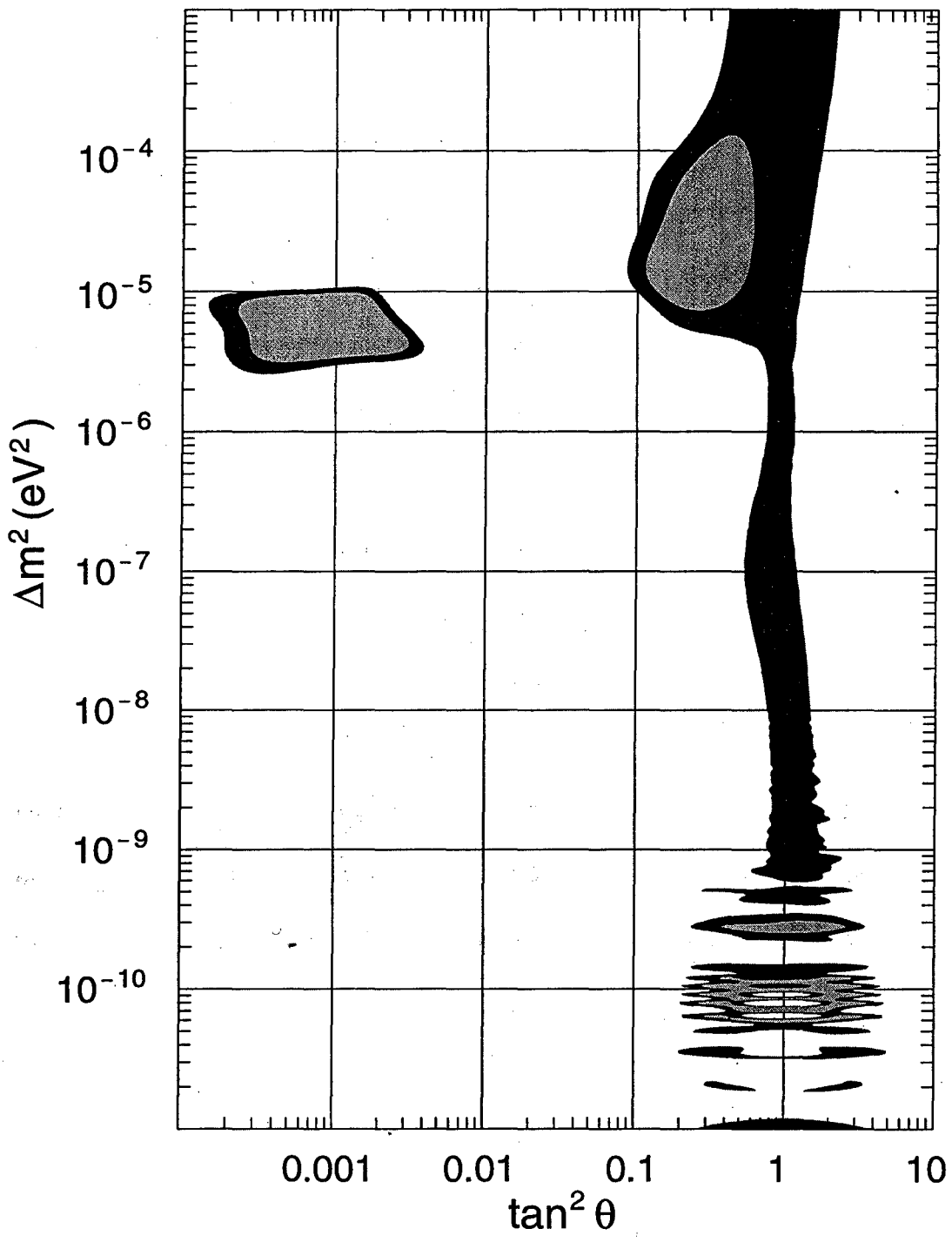

Figure 5.9: A global fit to the solar neutrino event rates at chlorine, gallium and water Cherenkov experiments, where the ^{8}B flux is treated as a free parameter. Contours are shown at 2 σ (light shade) and 3 σ (dark shade).

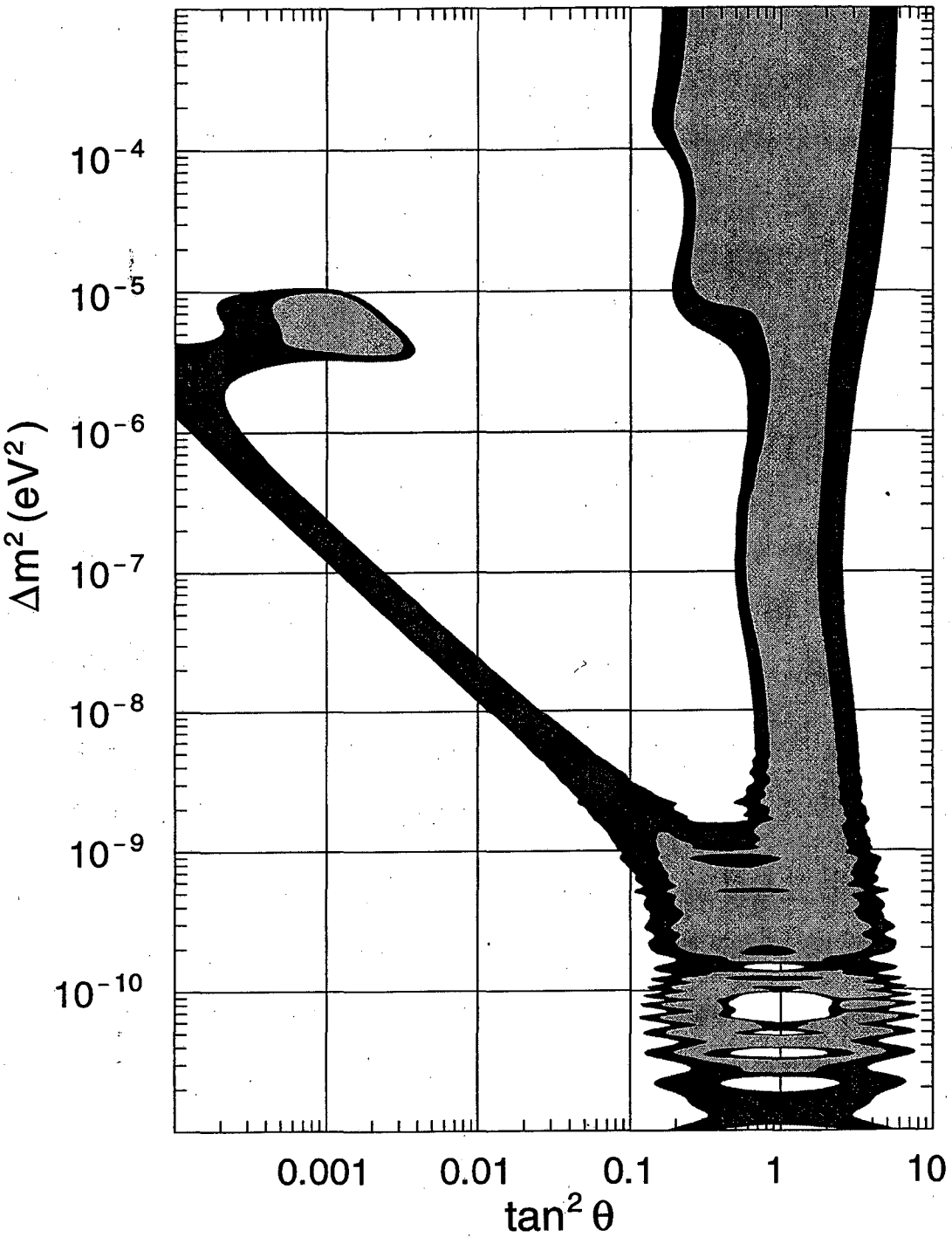

Figure 5.10: A global fit to the solar neutrino event rates at the gallium and water Cherenkov experiments but not at the chlorine experiment. Contours are shown at 2 σ (light shade) and 3 σ (dark shade).

Chapter 6

Summary and Conclusion

It has been three decades since the first evidence of solar neutrino deficit was reported by the Homestake experiment. In the last ten years the experimental situation improved dramatically, when high quality data from experiments such as SAGE, GALLEX, and Super-Kamiokande became available. It was conclusively demonstrated that neutrinos do come from the Sun and that the observed flux is indeed depleted compared the the Standard Solar Model prediction. The present state of the solar neutrino problem has been summarized in Chapter 2.

To prove that the solar neutrino deficit is caused by neutrino oscillations, a new generation of solar neutrino experiments, such as Super-Kamiokande, SNO, Borexino, KamLAND, etc, will be seeking evidence for solar neutrino oscillations without relying on the Standard Solar Model in well-understood experimental environments. They aim not only at establishing oscillations but also at overdetermining the solution in

the next few years.

One of the "smoking gun" signatures the experiments are seeking is the anomalous seasonal variations of the observed solar neutrino flux. Such variations, if detected, would be an unmistakable sign of the long-wavelength vacuum oscillations. ^{7}Be experiments, such as Borexino and KamLAND, are particularly well suited to look for anomalous variations, because the ^{7}Be solar neutrinos are virtually monochromatic. In Chapter 3 we discussed how anomalous seasonal variations might be used to discover vacuum neutrino oscillations at these experiments, independent of the solar model and the measurement of the background. In particular, we found that, after three years of Borexino or KamLAND running, vacuum neutrino oscillations can be either established or excluded for almost all values of $(\sin^2 2\theta, \Delta m^2)$ preferred by the Homestake, GALLEX, SAGE, and Super-Kamiokande data. We also investigated in Sect. 3.3 how well seasonal variations of the data can be used to measure $(\sin^2 2\theta, \Delta m^2)$ in the case of vacuum oscillations.

If the experiments observe seasonal variations consistent with the $1/L^2$ flux modulation, the data can be used to measure the ^{7}Be solar neutrino flux in a background independent way. We explored the reach of this method in Section 3.1.

Another "smoking gun" signature would be the detection of the day-night variation in the event rate. Such variations are predicted to occur for a large range of parameters as a result of the electron neutrino regeneration in the Earth. In Chapter 4 we determined the sensitivity of Borexino and KamLAND to this phenomenon.

We pointed out that it is important to study the regeneration effect for the entire physical range of the mixing angle $0 \leq \theta \leq \pi/2$, the fact previously unrecognized in the literature. Our analysis naturally avoids the incorrect conclusions made in the literature about the maximal mixing.

We also discussed in Sect. 4.3 the possibility of using the earth regeneration data to measure the neutrino oscillation parameters. We found that in the case of the LOW solution to the solar neutrino deficit, the measurement results can be surprisingly accurate, if one uses the full observed zenith angle dependence, rather than only the day–night asymmetry. Our results further indicate that it may be possible to use the data to constrain models of the Earth's interior. A comparable study has never before been performed.

The part of the parameter space with $\theta > \pi/4$ we studied in Chapter 4 has been traditionally ignored in the literature. It was commonly thought that the MSW solutions are confined to the $\theta < \pi/4$ region, and the vacuum oscillation solutions are symmetric between $\theta < \pi/4$ and $\theta > \pi/4$. In Chapter 5 we reexamined these assumptions and performed fits to the experimental data in the enlarged neutrino parameter space $0 \leq \theta \leq \pi/2$. We found that in the case of vacuum oscillation solutions matter effects can be nonnegligible for the low energy *pp* neutrinos. Thus, the allowed regions in the two sides of the parameter space are not completely symmetric. We further found that the MSW solutions can extend beyond the maximal mixing if one takes the conservative attitude to allow higher confidence levels, ignore some of the

experimental results in the fits, or relax theoretical predictions. We presented a global view of the parameter space with Δm^2 varying from 10^{-11} eV^2 to 10^{-3} eV^2, without artificially splitting the MSW and the vacuum oscillation regions.

In the next decade SNO, Borexino, and KamLAND will be reporting their data. Their results will eventually supersede data from the past experiments. It is therefore important to analyze the future data without too much prejudice based on the past data. We therefore believe that it is essential for the fits to the new data to be presented in the full parameter space. Ultimately, of course, we hope that the experimental data will shrink the allowed regions to a single point.

Bibliography

[1] J. N. Bahcall, P. I. Krastev, and A. Y. Smirnov, Phys. Lett. **B477**, 401 (2000), hep-ph/9911248.

[2] J. N. Bahcall, P. I. Krastev, and A. Y. Smirnov, Phys. Rev. **D58**, 096016 (1998), hep-ph/9807216.

[3] M. C. Gonzalez-Garcia, P. C. de Holanda, C. Pena-Garay, and J. W. F. Valle, (1999), hep-ph/9906469.

[4] J. N. Bahcall, S. Basu, and M. H. Pinsonneault, Phys. Lett. **B433**, 1 (1998), astro-ph/9805135.

[5] M. Goldhaber, L. Grodzins, and A. Sunyar, Phys. Rev. **109**, 1015 (1958).

[6] C. L. Cowan, H. W. Cruse, F. B. Harrison, A. D. McGuire, and F. Reines, Science **124**, 103 (1956).

[7] S. L. Glashow, Nucl. Phys. **22**, 579 (1961).

[8] A. Salam, Originally printed in *Svartholm: Elementary Particle Theory, Proceedings Of The Nobel Symposium Held 1968 At Lerum, Sweden*, Stockholm 1968, 367-377.

[9] S. Weinberg, Phys. Rev. Lett. **19**, 1264 (1967).

[10] C. Caso *et al.*, Eur. Phys. J. **C3**, 1 (1998).

[11] L. Wolfenstein, Phys. Rev. **D17**, 2369 (1978).

[12] E. K. Akhmedov, Sov. J. Nucl. Phys. **47**, 301 (1988).

[13] E. K. Akhmedov, Phys. Lett. **B213**, 64 (1988).

[14] E. K. Akhmedov, (1999), hep-ph/9903302, hep-ph/9907435.

[15] S. P. Mikheev and A. Y. Smirnov, Yad. Fiz. (Sov. J. Nucl. Phys.) **42**, 913 (1985).

[16] S. P. Mikheev and A. Y. Smirnov, Nuovo Cim. **9C**, 17 (1986).

[17] J. N. Bahcall, *Neutrino Astrophysics* (Cambridge University Press, Cambridge, England, 1989).

[18] J. N. Bahcall and P. I. Krastev, Phys. Lett. **B436**, 243 (1998), hep-ph/9807525.

[19] B. T. Cleveland *et al.*, Astrophys. J. **496**, 505 (1998).

[20] SAGE, J. N. Abdurashitov *et al.*, Phys. Rev. **C60**, 055801 (1999), astro-ph/9907113.

[21] GALLEX, W. Hampel *et al.*, Phys. Lett. **B447**, 127 (1999).

[22] Kamiokande, Y. Fukuda *et al.*, Phys. Rev. Lett. **77**, 1683 (1996).

[23] Y. Suzuki, talk presented at the XIX International Symposium on Lepton and Photon Interactions at High Energies, Stanford University, August 9-14, 1999.

[24] http://www.sns.ias.edu/~jnb/.

[25] S. T. Petcov, Phys. Lett. **B214**, 139 (1988).

[26] S. Pakvasa and J. Pantaleone, Phys. Rev. Lett. **65**, 2479 (1990).

[27] J. Pantaleone, Phys. Lett. **B251**, 618 (1990).

[28] T. Kaneko, *Prog. Theor. Phys.* **78**, 532 (1987); S. Toshev, *Phys. Lett.* **B 196**, 170 (1987); M. Ito, T. Kaneko, and M. Nakagawa, *Prog. Theor. Phys.* **79**, 13 (1988) [Erratum **79**, 555 (1988)].

[29] S. T. Petcov, Phys. Lett. **B200**, 373 (1988).

[30] P. I. Krastev and S. T. Petcov, Phys. Lett. **B207**, 64 (1988), Erratum-ibid. **B214**, 661 (1988).

[31] H. Minakata and H. Nunokawa, Phys. Rev. **D59**, 073004 (1999), hep-ph/9810387.

[32] S. L. Glashow and L. M. Krauss, Phys. Lett. **B190**, 199 (1987).

[33] V.N. Gribov and B. Pontecorvo, *Phys. Lett.* **28B**, 493 (1969); J.N. Bahcall and S.C. Frautschi, *Phys. Lett.* **29B**, 623 (1969); S.M. Bilenky and B. Pontecorvo, *Phys. Rep.* **41C**, 225 (1978); R. Ehrlich, *Phys. Rev.* **D 18**, 2323 (1978); R. Barbieri, J. Ellis, and M.K. Gaillard, *Phys. Lett.* **90B**, 249 (1980); K. Whisnant, R. Phillips, and V. Barger, *Phys. Rev.* **D 24**, 538 (1981).

[34] V. Barger, R.J.N. Phillips, and K. Whisnant, *Phys. Rev. Lett.* **65**, 3084 (1990); Z.G. Berezhiani, A. Rossi, *Phys. Rev* **D 51**, 5229 (1995), hep-ph/9409464; P.I. Krastev and S.T. Petcov, *Nucl. Phys.* **B449**, 605 (1996), hep-ph/9408234; B. Faïd, G.L. Fogli, E. Lisi, D. Montanino, *Phys. Rev.* **D 55**, 1353 (1997), hep-ph/9608311; *Astropart. Phys.* **10**, 93 (1999), hep-ph/9805293; J.M. Gelb and S.P. Rosen, hep-ph/9809508; V. Berezinsky, G. Fiorentini, and M. Lissia, INFN-CA-TH-98-15, hep-ph/9811352.

[35] S. L. Glashow, P. J. Kernan, and L. M. Krauss, Phys. Lett. **B445**, 412 (1999), hep-ph/9808470.

[36] J. B. Benziger *et al.*, "A Proposal for Participation in the Borexino Solar Neutrino Experiment", http://pupgg.princeton.edu/~Borexino/ppp.html; L. Oberauer, talk presented at NEUTRINO '98 conference, June 4–9, 1998, Takayama, Japan.

[37] A. Suzuki, talk presented at the VIII International Workshop on "Neutrino Telescopes", February 23-26, 1999, Venice, Italy, transparences and proceedinds can

be found at http://axpd24.pd.infn.it/conference/venice99.html; more information about the experiment at http://www.awa.tohoku.ac.jp/html/KamLAND/.

[38] J. Busenitz *et al.*, "Proposal for US Participation in KamLAND," March 1999, http://citnp.caltech.edu/andreas/kam_prop.html.

[39] J. N. Bahcall and M. H. Pinsonneault, Rev. Mod. Phys. **67**, 781 (1995), hep-ph/9505425.

[40] J. N. Bahcall, Phys. Rev. **D49**, 3923 (1994).

[41] A. Loeb, Phys. Rev. **D39**, 1009 (1989).

[42] G. L. Fogli, E. Lisi, and D. Montanino, Phys. Rev. **D56**, 4374 (1997), hep-ph/9706228.

[43] Super-Kamiokande, Y. Fukuda *et al.*, Phys. Rev. Lett. **82**, 2430 (1999), hep-ex/9812011.

[44] SNO, J. Boger *et al.*, (1999), nucl-ex/9910016.

[45] E.D. Carlson, *Phys. Rev.* **D 34**, 1454 (1986); A.J. Baltz and J. Weneser, *Phys. Rev.* **D 35**, 528 (1987); **D 37**, 3364 (1988);**D 50**, 5971 (1994); **D 51**, 3960 (1995); E. Lisi and D. Montanino, *Phys. Rev.* **D 56**, 1792 (1997); Q.Y. Liu, M. Maris and S.T. Petcov, *Phys. Rev.* **D 56** 5991 (1997); M. Maris and S.T. Petcov, *Phys. Rev.* **D 56** 7444 (1997).

[46] J. N. Bahcall and P. I. Krastev, Phys. Rev. **C56**, 2839 (1997), hep-ph/9706239.

[47] A. H. Guth, L. Randall, and M. Serna, JHEP **08**, 018 (1999), hep-ph/9903464.

[48] G. L. Fogli, E. Lisi, and D. Montanino, Phys. Rev. **D54**, 2048 (1996), hep-ph/9605273.

[49] Super-Kamiokande, Y. Fukuda *et al.*, Phys. Rev. Lett. **82**, 1810 (1999), hep-ex/9812009.

[50] A. S. Dighe, Q. Y. Liu, and A. Y. Smirnov, (1999), hep-ph/9903329.

[51] A. Dziewonski and D. Anderson, Phys. Earth Planet. Interior **25**, 207 (1981).

[52] S. Kasuga, *Observation of a Small ν_μ/ν_e Ratio of Atmospheric Neutrinos in Super-Kamiokande by the Method of Particle Identification*, PhD thesis, University of Tokyo, 1998, http://www-sk.icrr.u-tokyo.ac.jp/doc/sk/pub/main.ps.gz.

[53] G. L. Fogli, E. Lisi, D. Montanino, and A. Palazzo, (1999), hep-ph/9912231.

[54] C. Giunti, M. C. Gonzalez-Garcia, and C. Pena-Garay, (2000), hep-ph/0001101.

[55] J. Pantaleone, Phys. Rev. **D43**, 2436 (1991).

[56] J. N. Bahcall, M. Pinsonneault, and S. Basu, BP2000, to be published, http://www.sns.ias.edu/~jnb.

[57] G. L. Fogli and E. Lisi, Astropart. Phys. **3**, 185 (1995).

[58] R. Barbieri, L. J. Hall, D. Smith, A. Strumia, and N. Weiner, JHEP **12**, 017 (1998), hep-ph/9807235.

[59] A. de Gouvea, A. Friedland, and H. Murayama, (2000), hep-ph/0002064.

[60] A. Friedland, (2000), hep-ph/0002063.

[61] A. de Gouvea, A. Friedland, and H. Murayama, (1999), hep-ph/9910286.

[62] A. de Gouvea, A. Friedland, and H. Murayama, Phys. Rev. **D60**, 093011 (1999), hep-ph/9904399.

[63] M. C. Gonzalez-Garcia and C. Pena-Garay, (2000), hep-ph/0002186.

Appendix A

To Chapter 2

A.1 Derivation of the expression for the index of refraction

In this appendix we will derive the formula

$$n = 1 + \frac{2\pi N}{k^2} f(0), \tag{A.1}$$

using the methods of classical wave optics. Eq. (A.1) relates the index of refraction of a medium n to the forward scattering amplitude $f(0)$ of the scatterers that make up the medium. k is a wave number and N is the number density of the scatterers.

Consider first a simplified situation when there is only a single thin layer of the scatterers (Fig. A.1). Far away from the layer at point O the amplitude of the wave is the sum of the incoming and scattered waves, as shown in the phasor diagram on

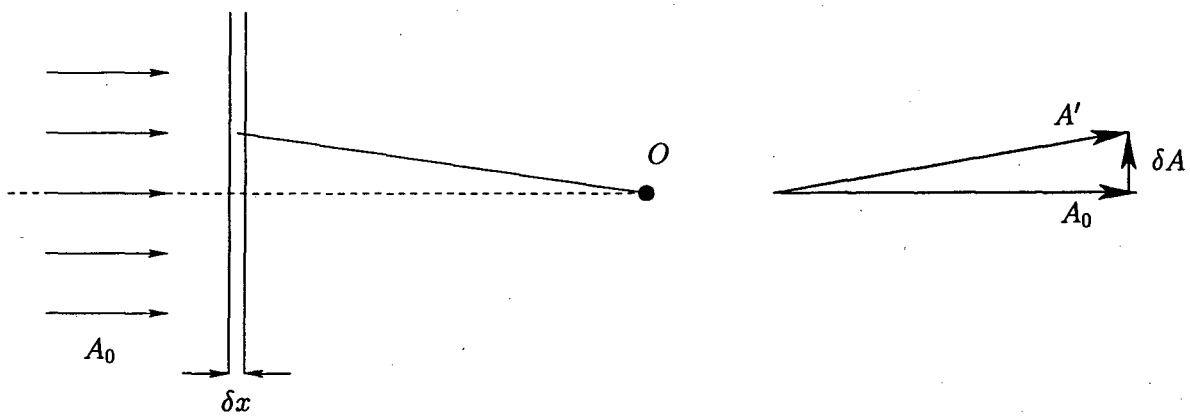

Figure A.1: Illustation to Appendix A.1.

the right side of the figure.

The phasor diagram shows that the effect of the scatterers is to add an additional phase shift $\delta\phi = \delta A/A_0$ to the incident wave. This can effectively be represented by assigning the scattering layer an index of refraction n. The value of n can be found requiring that the change in the optical path results in the phase shift $\delta\phi$:

$$2\pi\frac{\delta x(n-1)}{\lambda} = \delta\phi \Longrightarrow n = 1 + \frac{\lambda}{2\pi}\frac{\delta\phi}{\delta x} = 1 + \frac{1}{k}\frac{\delta\phi}{\delta x}. \tag{A.2}$$

We now turn to computing δA. It is equal to the sum of the contributions from all scatterers in the layer, with each scatterer contributing f/r. It is very easy to see by drawing a corresponding phasor diagram that the total amplitude δA should be equal to $1/\pi\times$(the amplitude obtained if all scatterers within the first Fresnel zone added up in phase). The size of the first Fresnel zone is

$$r_1 = \sqrt{(L+\lambda/2)^2 - L^2} \simeq \sqrt{L\lambda}. \tag{A.3}$$

If all scatterers in that zone interfered in phase at O, their contribution to δA would be equal to $A_0 N \delta x \pi r_1^2 f(0)/L$. Thus,

$$\delta A = A_0 N \delta x r_1^2 f(0)/L = A_0 N \delta x f(0) \lambda. \tag{A.4}$$

Then

$$1 + \frac{1}{k}\frac{\delta A/A_0}{\delta x} = 1 + \frac{1}{k} N f(0) \lambda = 1 + \frac{2\pi}{k^2} N f(0). \tag{A.5}$$

Q.E.D.

Appendix B

To Chapter 3

B.1 χ^2 Analysis

In the analyses in Sec. 3.2, 3.3, and 3.4, we are interested in the capability of an "average" experiment. It is possible to simulate "data" with statistical fluctuations included, but then the value of χ^2 would vary slightly between different repetitions of the same simulation. A better approach is to find an expression for χ^2 "averaged" over many simulations. As we show below, averaging over statistical fluctuations simply leads to the inclusion of a constant term in the definition of χ^2.

Suppose we have some solar neutrino data binned into N_{bins} bins. Let the average expected value in the ith bin be d_i with corresponding random fluctuation Δd_i. Suppose we want to fit this data with a function f, which can depend on two parameters:

the signal s and the background b. Then the χ^2 of the fit can be defined as follows:

$$\chi^2(s,b) = \sum_i^{N_{\rm bins}} \frac{(d_i + \Delta d_i - f_i(s,b))^2}{\sigma_{d_i}^2}, \tag{B.1}$$

where $\sigma_{d_i} = \sqrt{d_i + \Delta d_i}$. Because, in the case of interest, the number of events per bin is sufficiently large, we can approximately set $\sigma_{d_i} \simeq \sqrt{d_i}$.[1]

First consider the case when s and b are fixed numbers. The average value of the χ^2 one would obtain after simulating the data many times is

$$\langle \chi^2 \rangle = \left\langle \sum_i^{N_{\rm bins}} \left[\frac{(\Delta d_i)^2}{d_i} + \frac{2\Delta d_i (d_i - f_i)}{d_i} + \frac{(d_i - f_i)^2}{d_i} \right] \right\rangle. \tag{B.2}$$

Using $\langle \Delta d_i \rangle = 0, \langle (\Delta d_i)^2 \rangle = d_i$, we find

$$\langle \chi^2 \rangle = \sum_i^{N_{\rm bins}} \left[1 + \frac{(d_i - f_i)^2}{d_i} \right] = N_{\rm bins} + \sum_i^{N_{\rm bins}} \frac{(d_i - f_i)^2}{d_i}. \tag{B.3}$$

Therefore, in this simplest case it is enough to use the average values d_i and the number of bins to compute $\langle \chi^2 \rangle$.

Next, consider the case when $f(s,b) = b + g(s)$ and χ^2 is minimized with respect to b.

$$\begin{aligned} \frac{\partial \chi^2(s,b)}{\partial b} &= -\sum_i^{N_{\rm bins}} \frac{2(d_i + \Delta d_i - b - g_i(s))}{d_i} = 0 \\ \Longrightarrow b &= \left(\sum_i^{N_{\rm bins}} \frac{(d_i + \Delta d_i - g_i(s))}{d_i} \right) \left(\sum_i^{N_{\rm bins}} \frac{1}{d_i} \right)^{-1}. \end{aligned} \tag{B.4}$$

Introducing $A_i \equiv (d_i + \Delta d_i - g_i(s))/d_i$ and substituting Eq. (B.4) in Eq. (B.1), we

[1] One can easily estimate the resulting relative error in χ^2 to be of $O(1/\sqrt{\langle d_i \rangle})$.

obtain

$$\chi^2_{min} = \sum_i^{N_{\rm bins}} \left[\frac{A_i^2}{d_i} - 2\frac{A_i}{d_i} \left(\sum_i^{N_{\rm bins}} \frac{A_i}{d_i} \right) \left(\sum_i^{N_{\rm bins}} \frac{1}{d_i} \right)^{-1} + \frac{1}{d_i} \left(\sum_i^{N_{\rm bins}} \frac{A_i}{d_i} \right)^2 \left(\sum_i^{N_{\rm bins}} \frac{1}{d_i} \right)^{-2} \right]$$

$$= \sum_i^{N_{\rm bins}} \frac{A_i^2}{d_i} - \left(\sum_i^{N_{\rm bins}} \frac{A_i}{d_i} \right)^2 \left(\sum_i^{N_{\rm bins}} \frac{1}{d_i} \right)^{-1}. \qquad \text{(B.5)}$$

Now plugging back in the definition of A_i, we perform the averaging using $\langle \Delta d_i \rangle = 0$, $\langle (\Delta d_i)^2 \rangle = d_i$, and $\langle (\Delta d_i)(\Delta d_j) \rangle = 0$ for $i \neq j$:

$$\left\langle \sum_i^{N_{\rm bins}} \frac{A_i^2}{d_i} \right\rangle = N_{\rm bins} + \sum_i^{N_{\rm bins}} \frac{(d_i - f_i)^2}{d_i}, \qquad \text{(B.6)}$$

$$\left\langle \left(\sum_i^{N_{\rm bins}} \frac{A_i}{d_i} \right)^2 \right\rangle = \left(\sum_i^{N_{\rm bins}} \frac{1}{d_i} \right) + \left(\sum_i^{N_{\rm bins}} \frac{(d_i - g_i(s))}{d_i} \right)^2. \qquad \text{(B.7)}$$

Substituting Eq. (B.6) in Eq. (B.5), we find

$$\langle \chi^2_{min} \rangle = N_{\rm bins} - 1 + \sum_i^{N_{\rm bins}} \frac{(d_i - f_i)^2}{d_i} - \left(\sum_i^{N_{\rm bins}} \frac{(d_i - g_i(s))}{d_i} \right)^2 \left(\sum_i^{N_{\rm bins}} \frac{1}{d_i} \right)^{-1}. \qquad \text{(B.8)}$$

The last two terms are exactly what one would find after minimizing $\sum_i^{N_{\rm bins}} (d_i - b - g_i(s))^2/d_i$ with respect to b, and hence in this case random fluctuations can be accounted for by replacing $N_{\rm bins}$ in Eq. (B.3) by $N_{\rm bins} - 1$.

One can easily show that, if $f(s,b)_i = b + s \cdot h_i$ and one minimizes χ^2 with respect to s, the effect of random fluctuations is also to substitute $N_{\rm bins} - 1$ for $N_{\rm bins}$ in Eq. (B.3). The proof is completely analogous to the case we just studied. Moreover, it is straightforward to combine the two results and consider minimization with respect to both b and s, in which case one should replace $N_{\rm bins}$ in Eq. (B.3) by $N_{\rm bins} - 2$.

In general, one should use the number of degrees of freedom $N_{\text{d.o.f.}}$ when computing $\langle\chi^2\rangle$:

$$\langle\chi^2\rangle = N_{\text{d.o.f.}} + \sum_i^{N_{\text{bins}}} \frac{(d_i - f_i)^2}{d_i}. \tag{B.9}$$

B.2 Analytic Estimate of the Sensitivity Cutoff

In Sec. 3.2 we showed that the sensitivity region for anomalous seasonal variations is limited by the finite linewidth of the ^{7}Be line. In this appendix we show how one can analytically estimate the location and the shape of the sensitivity cutoff.

As was mentioned in Sec. 3.2, the true shape of the ^{7}Be line is rather complicated, with a Gaussian profile on the low end and an exponential tail on the high end. For the purpose of this estimate we choose to approximate the Gaussian part by a sharp cutoff:

$$f(E) = \begin{cases} 0 & \text{if } E < E_1 \\ e^{-aE+b} & \text{if } E > E_1 \end{cases}. \tag{B.10}$$

To determine the fraction of neutrinos reaching the Earth we integrate the oscillation probability $P(E, L)$ given by Eq. (3.7) over the line profile Eq. (B.10) and divide

by the normalization constant N.

$$\begin{aligned}\widetilde{P}(L) &= \frac{1}{N}\int dE P(E,L) f(E) \\ &\simeq \frac{1}{N}\left[\left(1-\frac{\sin^2 2\theta}{2}\right)\int_{E_1}^{\infty} dE e^{-aE+b}\right. \\ &\quad \left. + \frac{\sin^2 2\theta}{2}\int_{E_1}^{\infty} dE \cos\left(2\frac{1.27\Delta m^2 L}{E_0^2}(E_0-E)\right) e^{-aE+b}\right] \\ &= \frac{e^{-aE_1+b}}{N}\left[\left(1-\frac{\sin^2 2\theta}{2}\right)\frac{1}{a} + \frac{\sin^2 2\theta}{2}\frac{1}{\sqrt{a^2+(1.27\Delta m^2 L/E_0^2)^2}}\right. \\ &\quad \left. \times \cos\left(2\frac{1.27\Delta m^2 L}{E_0^2}(E_0-E_1) - \arctan\left(2\frac{1.27\Delta m^2 L}{aE_0^2}\right)\right)\right]. \qquad \text{(B.11)}\end{aligned}$$

Since the width of the line is only several keV while $E_0 = 0.862$ MeV, we can set $E_0 - E_1 \simeq E_0$ in the argument of the cosine. Substituting the value of the normalization constant $N = \int_{E_1}^{\infty} dE e^{-aE+b} = (1/a)e^{-aE_1+b}$ and introducing $\phi \equiv \arctan(2 \times 1.27\Delta m^2 L/(aE_0^2))$, we obtain

$$\widetilde{P}(L) \simeq 1 - \frac{\sin^2 2\theta}{2}\left(1 - \frac{\cos\left(2\frac{1.27\Delta m^2 L}{E_0} - \phi\right)}{\sqrt{1+(1.27\Delta m^2 L/(E_0^2 a))^2}}\right). \qquad \text{(B.12)}$$

From this equation we can read off the shape of the cutoff. Viewed as a function of Δm^2, for small values of the mixing angle the cutoff profile is approximately given by

$$\sin^2 2\theta_{\text{cutoff}} \propto \sqrt{1+(1.27\Delta m^2 L/(E_0^2 a))^2}. \qquad \text{(B.13)}$$

Using the numerical value of $a = 0.75$ keV^{-1}, obtained by fitting the line profile in [40], we find that $\sin^2 2\theta_{\text{cutoff}}(\Delta m^2)$ should increase by $\sqrt{2}$ with respect to the smallest value of $\sin^2 2\theta_{\text{cutoff}}$ when $\Delta m^2 \simeq 2.9 \times 10^{-9}$ eV^2. The actual number from

curve 4 in Fig. 3.7 is $\Delta m^2 \simeq 1.5 \times 10^{-9}$ eV^2. The actual value is smaller, which is expected, because, for the purpose of this estimate, we neglected the contribution of the Gaussian part of the line profile, effectively making the line narrower.

One can also estimate the location of the cutoff if the line profile were purely Gaussian (curve 3 in Fig. 3.7). The steps are completely analogous: the new normalization constant is $N' = \int_{-\infty}^{\infty} dE e^{-(E-E_0)^2/\sigma^2} = \sqrt{\pi}\sigma$, and $\widetilde{P}(L)$ is given by

$$\begin{aligned}
\widetilde{P}(L) &= \frac{1}{N'} \int_{-\infty}^{\infty} dE P(E,L) e^{-E^2/\sigma^2} \\
&\simeq \frac{1}{N'} \left[\left(1 - \frac{\sin^2 2\theta}{2} \right) \int_{-\infty}^{\infty} dE e^{-E^2/\sigma^2} \right. \\
&\quad \left. + \frac{\sin^2 2\theta}{2} \int_{-\infty}^{\infty} dE \cos\left(2 \frac{1.27 \Delta m^2 L}{E_0^2} (E_0 - E) \right) e^{-E^2/\sigma^2} \right] \\
&= 1 - \frac{\sin^2 2\theta}{2} \left(1 - e^{-(1.27\Delta m^2 L \sigma / E_0^2)^2} \cos\left(2 \frac{1.27 \Delta m^2 L}{E_0} \right) \right). \qquad \text{(B.14)}
\end{aligned}$$

Thus, the cutoff for this model sets in faster and the profile for small values of $\sin^2 2\theta$ is Gaussian. Numerically, $\sin^2 2\theta_{\text{cutoff}}(\Delta m^2)$ is expected to increase by $\sqrt{2}$ with respect to the smallest value of $\sin^2 2\theta_{\text{cutoff}}$ when $\Delta m^2 \simeq 4.2 \times 10^{-9}$ eV^2, which agrees with curve 3 in Fig. 3.7.

Appendix C

To Chapter 4

C.1 Matter Oscillations and No Level Crossing

In this appendix we discuss the survival probability of solar electron neutrinos outside the Sun, in particular the case of no level crossing, *i.e.,* when $\Delta m^2 \cos 2\theta < 0$ in the language of the two neutrino mixing scenario.

In the literature, matter effects in the Sun are always considered when there is "level crossing" inside of the Sun, *i.e.,* when the light neutrino is predominantly of the electron type, and, due to neutrino-electron interactions, when the instantaneous Hamiltonian eigenstate with the largest eigenvalue is predominantly of the electron type in the Sun's core. The other case, when the *heavy* neutrino is predominantly of the electron type, has not been studied in the literature in the context of two neutrino oscillations. The authors of [48], however, have considered this possibility

in the context of three-flavor oscillations.

The reason for this apparent neglect is simple, and will become clear as our results are presented. What happens is that, in the case of no level crossing, the average electron neutrino survival probability is always bigger than 1/2, and therefore on the surface it seems that this scenario is not relevant to the solar neutrino problem. This, however, is not the case, as discussed in detail in Chapter 5. Furthermore, in the region of the "just-so" solution it was believed that the no level crossing case would yield identical results as the level crossing case, but as Sect. 5.1 explains this is also not the case.

In the following analysis we will use the notation and results introduced in Sect. 2.3.3. Given Eq. (2.59) of that section, it is easy to show that, while for $\theta < \pi/4$, P_{ee} can be (much) smaller than 1/2, for $\theta > \pi/4$, P_{ee} is always larger than 1/2 (indeed, it will be shown that $P_{ee} \geq P_{ee}^{v}$, the (averaged) vacuum survival probability).

First, note that $-1 \leq \cos 2\theta_{\odot} \leq \cos 2\theta$. The equalities are saturated when $\sqrt{2}G_F N_e(0) \gg \Delta m^2/2E_\nu$ or $\sqrt{2}G_F N_e(0) \ll \Delta m^2/2E_\nu$, respectively. More quantitatively

$$\frac{\Delta m^2}{2E_\nu\sqrt{2}G_F N_e(0)} = 0.98\left(\frac{\Delta m^2}{10^{-5}\mathrm{eV}^2}\right)\left(\frac{0.862\mathrm{MeV}}{E_\nu}\right), \tag{C.1}$$

for an average core electron number density of 79 moles/cm^3 [4]. Therefore, in the case of ^{7}Be neutrinos and $\Delta m^2 \ll 10^{-5}$ eV^2,

$$\cos 2\theta_{\odot} = -1 + \frac{1}{2}\left(\frac{\Delta m^2 \sin 2\theta}{2E_\nu\sqrt{2}G_F N_e(0)}\right)^2 + \mathcal{O}\left(\frac{\Delta m^2}{2E_\nu\sqrt{2}G_F N_e(0)}\right)^3, \tag{C.2}$$

and

$$P_{ee} \simeq (1 - P_c)\sin^2\theta + P_c\cos^2\theta. \tag{C.3}$$

We will soon show that $P_c \in [0, \cos^2\theta]$,[1] so that, in the limit $\cos 2\theta_\odot \to -1$,

$$P_{ee} \in [\sin^2\theta, \sin^4\theta + \cos^4\theta] \quad \text{or} \tag{C.4}$$

$$P_{ee} \in [\sin^4\theta + \cos^4\theta, \sin^2\theta] \tag{C.5}$$

Eq. (C.4) (Eq. (C.5)) applies if $\sin^2\theta < \cos^2\theta$ ($\sin^2\theta > \cos^2\theta$). This is easy to see because $\sin^4\theta + \cos^4\theta = 1 - (1/2)\sin^2 2\theta$ is the average vacuum survival probability P^v_{ee} and

$$\begin{aligned} P^v_{ee} &= 1 - 2\sin^2\theta(1 - \sin^2\theta) \\ &= 1 - 2\sin^2\theta + 2\sin^4\theta, \end{aligned} \tag{C.6}$$

which is bigger (smaller) than $\sin^2\theta$ if $\sin^2\theta < \cos^2\theta$ ($\sin^2\theta > \cos^2\theta$). If the oscillatory terms do not average out,

$$P^v_{ee} = \sin^4\theta + cos^4\theta + 2\sin^2\theta\cos^2\theta\cos\left(2.54\frac{\Delta m^2 L}{E_\nu}\right). \tag{C.7}$$

When $\sqrt{2}G_F N_e(0) \ll \Delta m^2/2E_\nu$ matter interactions should be irrelevant, and it is easy to see from Eq. (2.50) that $\cos 2\theta_\odot \to \cos 2\theta$. In this limit $P_c \to 0$, since we are deep into the adiabatic region (as will be shown later) and $P_{ee} \to P^v_{ee}$.

[1] This is not hard to see. It is known that, if Δm^2 is large enough, the adiabatic approximation should hold, and therefore $P_c \to 0$ for large enough Δm^2. On the other hand, if Δm^2 is small enough, one should reproduce the vacuum oscillation result (as in the just-so scenario), and, from Eq. (2.59), it is easy to see that this happens when $P_c \to \cos^2\theta$ and $\cos 2\theta_\odot \to -1$.

The jumping probability P_c in the exponential approximation for the Sun's density is given by Eq. 2.61 of Sect. 2.3.3. According to the author of [29], this equation only holds for $\Delta m^2 \cos 2\theta > 0$. We will prove shortly, however, that Eq. (2.61) also applies in the case of no level crossing, when the *heavy* mass eigenstate is predominantly of the electron type, *i.e.* when $\sin^2\theta > \cos^2\theta$. Assuming that this is indeed the case, we can finish our discussion on the behavior of the electron neutrino survival probability, using ^{7}Be neutrinos as an example.

When $\Delta m^2 \ll 10^{-9}$ eV^2, $\cos 2\theta_\odot = -1$ and $P_c = \cos^2\theta$. In this case we argued and one can explicitly check that $P_{ee} = P^v_{ee}$.[2] For 10^{-9} eV$^2 \ll \Delta m^2 \ll 10^{-5}$ eV^2, $\cos 2\theta_\odot = -1$ and $P_c \to 0$. In this case $P_{ee} \simeq \sin^2\theta$. This is the adiabatic region. For $\Delta m^2 \gg 10^{-5}$ eV^2, matter effects become irrelevant and $\cos 2\theta_\odot = \cos 2\theta$, $P_c = 0$. Again $P_{ee} = P^v_{ee}$. Therefore, Eqs. (C.4,C.5) apply for all values of interest, and one can get a very large suppression of P_{ee} if $\sin^2\theta \ll 1$. On the other hand, in the case of no level crossing, P_{ee} is always bigger than $P^v_{ee} \geq 1/2$.

Fig. C.1 depicts the behavior of $P^{(^7\mathrm{Be})}_{ee}$ as a function of Δm^2, for different values of the vacuum mixing angle. The preferred values from the overall rate analysis at the Homestake, SAGE and GALLEX, and SuperKamiokande experiments [3] are indicated by stars. The four plots are labeled SMA, LMA, LOW to indicate that

[2]Indeed, this is the region of the "just-so" solution. As a matter of fact, in this region the distance dependent vacuum oscillations do not average out when the neutrinos are detected at the Earth, and one should use the position dependent expression, Eq. (2.60). It is trivial to check that, when $\cos 2\theta_\odot = -1$ and $P_c = \cos^2\theta$ Eq. (2.60) reproduces the vacuum oscillation expression Eq.(C.7), up to a phase (see Chapter 3). That this is also true for $\cos 2\theta < 0$ was explicitly checked starting with the exact solutions to Schrödinger's equation [28, 29].

they contain the best fit values of θ for the Small Mixing Angle, Large Mixing Angle and LOW Δm^2 solutions [3], respectively, and INT to indicate an intermediate value of θ between the SMA and LMA solutions. The dotted line indicates the value of P_{ee}^{v}. Similarly, Fig. C.2 depicts $P_{ee}^{(^7\mathrm{Be})}$ as a function of $\sin^2\theta$ for different values of the mass squared difference. We use the same notation as the one used in Fig. C.1, and the vertical dashed lines indicate the mixing angle for maximal vacuum mixing ($\sin^2\theta = 1/2$). Note that at this point $P_{ee}^{(^7\mathrm{Be})} = P_{ee}^{v} = 1/2$.

Finally, we argue that Eq. (2.61) holds for all values of $\cos 2\theta$. When $\sqrt{2}G_F N_e(0) \gg |\Delta m^2|/2E_\nu$, it is very simple to derive P_{ee}, following the exact solution [28, 29] to Schrödinger's equation and taking the appropriate limits. According to Eq. (39) in [29]

$$
\begin{aligned}
P_{\mu e} &= \frac{\sin^2(2\theta)}{4}\left[\frac{\sinh(\pi r_0 h_0\cos^2\theta)}{\cos^2\theta\sinh(\pi r_0 h_0)}e^{-\pi r_0 h_0\sin^2\theta}\right. \\
&+ \left.\frac{\sinh(\pi r_0 h_0\sin^2\theta)}{\sin^2\theta\sinh(\pi r_0 h_0)}e^{\pi r_0 h_0\cos^2\theta} + \mathcal{O}\left(\frac{\Delta m^2}{2E_\nu\sqrt{2}G_F N_e(0)}\right)^2\right], \qquad \text{(C.8)} \\
P_{\mu e} &\simeq \sin^2\theta\left(\frac{\sinh(\pi r_0 h_0\cos^2\theta)}{\sinh(\pi r_0 h_0)}e^{-\pi r_0 h_0\sin^2\theta}\right) \\
&+ \cos^2\theta\left(\frac{\sinh(\pi r_0 h_0\sin^2\theta)}{\sinh(\pi r_0 h_0)}e^{\pi r_0 h_0\cos^2\theta}\right), \\
P_{\mu e} &\simeq \sin^2\theta\left(\frac{e^{\pi r_0 h_0\cos 2\theta} - e^{-\pi r_0 h_0}}{e^{\pi r_0 h_0} - e^{-\pi r_0 h_0}}\right) + \cos^2\theta\left(\frac{e^{\pi r_0 h_0} - e^{\pi r_0 h_0\cos 2\theta}}{e^{\pi r_0 h_0} - e^{-\pi r_0 h_0}}\right), \\
P_{\mu e} &\simeq \sin^2\theta(P_c) + \cos^2\theta(1 - P_c),
\end{aligned}
$$

where $h_0 \equiv \Delta m^2/2E_\nu$ and P_c is given exactly by Eq. (2.61). Therefore

$$
P_{ee} = 1 - P_{\mu e} \simeq (1 - P_c)\sin^2\theta + P_c\cos^2\theta. \qquad \text{(C.9)}
$$

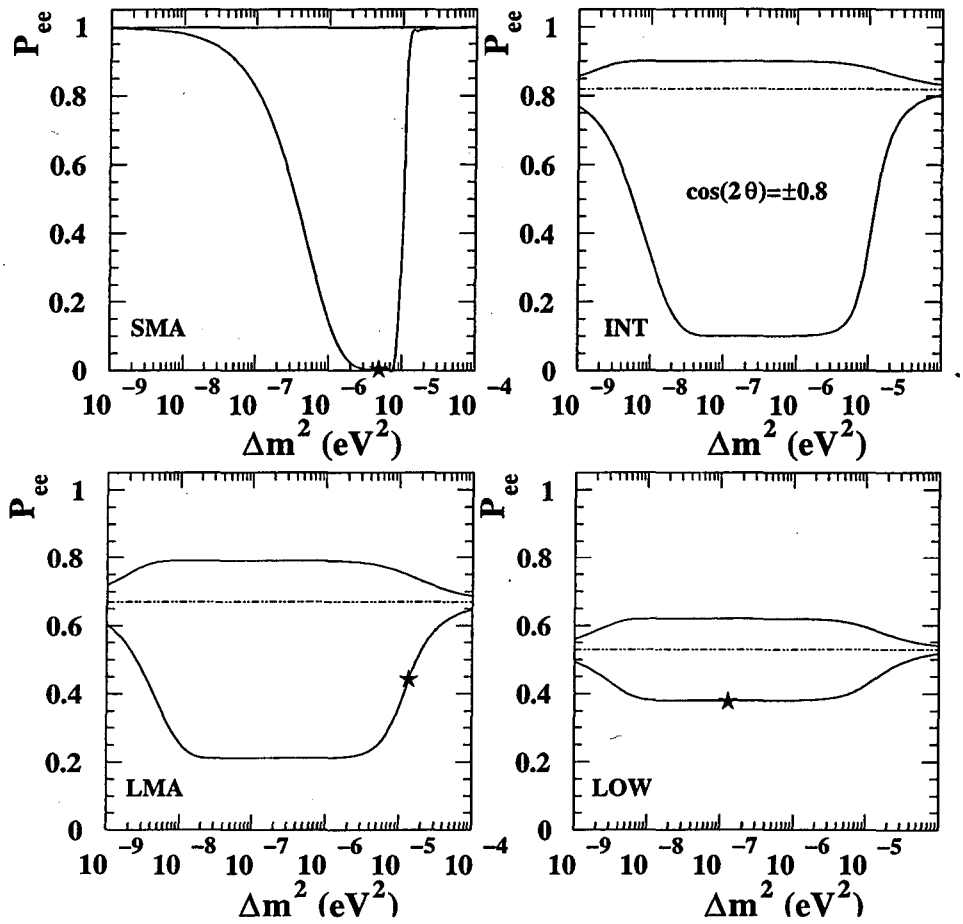

Figure C.1: The electron neutrino survival probability as a function Δm^2, for different values of the vacuum mixing angle, namely, $\cos 2\theta = \pm 0.997$ (SMA), $\cos 2\theta = \pm 0.8$ (INT), $\cos 2\theta = \pm 0.58$ (LMA), and $\cos 2\theta = \pm 0.24$ (LOW). The upper (lower) lines are for the negative (positive) sign of $\cos 2\theta < 0$. The stars indicate the preferred points from the overall rate analysis of the existing data [3], and the horizontal dotted lines indicate the vacuum survival probability, $P^v_{ee} = 1/2 - 1/2 \sin^2 2\theta$.

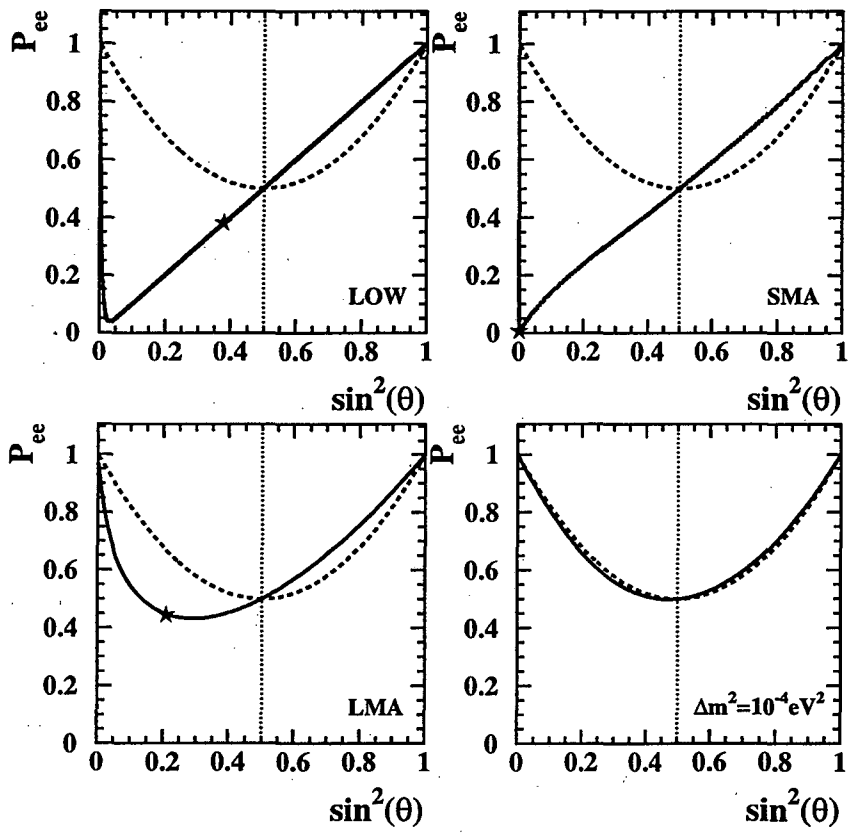

Figure C.2: The electron neutrino survival probability as a function $\sin^2\theta$, for different values of Δm^2, namely, $\Delta m^2 = 1.3\times10^{-7}$ eV^2 (LOW), $\Delta m^2 = 5.0\times10^{-6}$ eV^2 (SMA), $\Delta m^2 = 1.4\times10^{-5}$ eV^2(LMA), and $\Delta m^2 = 1\times10^{-4}$ eV^2. The stars indicate the preferred points from the overall rate analysis of the existing data [3], and the dashed lines indicate the vacuum survival probability, $P^v_{ee} = 1/2 - 1/2\sin^2 2\theta$.

Since, in deriving Eq. (C.8), no assumptions with respect to the sign of Δm^2 or the value of θ were made, it should be applicable in all cases,[3] as long as $\sqrt{2}G_F N_e(0) \gg |\Delta m^2|/2E_\nu$. Indeed, from Eqs. (2.50, 2.59) it is easy to note that, in the limit $\sqrt{2}G_F N_e(0) \gg |\Delta m^2|/2E_\nu$, $\cos 2\theta_\odot \to -1$ and Eq. (C.9) is exactly reproduced.

[3]That this is indeed the case was checked explicitly starting with the exact solution to Schrödinger's Equation in terms of Whittaker functions [28, 29]. Furthermore, in Chapter 5 (and also in reference[48]) the fact that Eq. (2.61) holds in the region of interested was verified numerically.

Ernest Orlando Lawrence Berkeley National Laboratory
One Cyclotron Road | Berkeley, California 94720

Prepared for the U.S. Department of Energy under Contract No. DE-AC03-76SF00098